



**HAL**  
open science

# Synthesis and characterisation of acceptor-doped BaSnO<sub>3</sub> compounds as proton conductors

Yanzhong Wang

► **To cite this version:**

Yanzhong Wang. Synthesis and characterisation of acceptor-doped BaSnO<sub>3</sub> compounds as proton conductors. Other. Ecole Centrale Paris, 2009. English. NNT : 2009ECAP0029 . tel-00453315

**HAL Id: tel-00453315**

**<https://theses.hal.science/tel-00453315>**

Submitted on 8 Oct 2014

**HAL** is a multi-disciplinary open access archive for the deposit and dissemination of scientific research documents, whether they are published or not. The documents may come from teaching and research institutions in France or abroad, or from public or private research centers.

L'archive ouverte pluridisciplinaire **HAL**, est destinée au dépôt et à la diffusion de documents scientifiques de niveau recherche, publiés ou non, émanant des établissements d'enseignement et de recherche français ou étrangers, des laboratoires publics ou privés.



**ÉCOLE CENTRALE DES ARTS  
ET MANUFACTURES  
« ÉCOLE CENTRALE PARIS »**

**THÈSE**  
présentée par

**Yanzhong WANG**

pour l'obtention du

**GRADE DE DOCTEUR**

**Spécialité : Science des Matériaux**

**Laboratoire d'accueil : Structures Propriétés et Modélisation des Solides  
UMR 8580 CNRS / Ecole Centrale Paris**

**SUJET :**

**Synthesis and characterisation of acceptor-doped  
BaSnO<sub>3</sub> compounds as proton conductors**

Soutenue le 25 septembre 2009

devant un jury composé de:

Mme Francesca PEIRO	Professeur à l'Universitat de Barcelona	Rapporteur
M. Gilles CABOCHE	Professeur à l'Université de Bourgogne	Rapporteur
Mme Rose-Noëlle VANNIER	Professeur à l'ENSCL	Examineur
M. Alain THOREL	Maître de Recherche à Mine de Paris	Président-Examineur
M. Guilhem DEZANNEAU	Chargé de Recherche à ECP	Co-directeur de thèse
M. Grégory GENESTE	Chef de Travaux	Co-directeur de thèse
M. Jean-Hubert SCHMITT	Directeur du Centre de Recherche de ECP	Invité

**2009-29**

**Ecole Centrale Paris**  
Grande voie des vignes  
92295 Châtenay-Malabry Cedex

## **Acknowledgements**

This work has been done in the Laboratoire Structures Propriétés et Modélisation des Solides (S.P.M.S) of the Ecole Centrale Paris (E.C.P.) and Centre National de la Recherche Scientifique (C.N.R.S., U.M.R.8580). I would like to sincerely thank M. Jean-Hubert SCHMITT, directeur de la recherche, for giving me encouragement and help, and I am also very grateful that he will take part in the defense of my thesis. I would also like to thank M. Jean-Michel KIAT, directeur du laboratoire for his support and guidance. As a recipient of China Scholarship Council (CSC) scholarship I want to thank CSC for the financial support, and the "Service de L'éducation" from the Chinese Embassy in France for their help and kind attention.

I would like to sincerely thank Mme F. Peiró, Professor of the University of Barcelona, and M. G. Caboche, Professor of the University of Dijon, for accepting to be the referees of my thesis.

I would also like to sincerely thank Mme R.N. Vannier, Professor of the University of Lillee, and M. A. Thorel, Maitre de recherche at the Centre des Matériaux-Armines for accepting as the examiners of my thesis.

I wish to express my deep gratitude to my advisor, Guilhem Dezanneau, who introduced me to solid-state electrochemistry, gave me the opportunity to realize this thesis in his group, and guided and encouraged me with much kindness and patience through the entire course of the study. I am also very grateful to my co-advisor, Gregory Geneste, for giving me lots of guidance and advice, and helping me revise my articles and thesis. I also wish to my sincere gratitude to my Chinese advisor, Prof. Guanjun Qiao from Xi'an Jiaotong University, who permitted and supported me to restart the thesis in Ecole Centrale Paris, and for his encouragement, understanding and guidance over these years.

I am very grateful to Anthony Chesnaud, post doctor of our group, for teaching me many experimental techniques, and also giving me lots of help and advice for my thesis. I

am also very grateful to other doctors of our group: Emile Bévillon, Marc-david Braida and Yang Hu. They gave me many suggestions and help, and we spent lots of unforgettable time, *i.e.* attending conferences, sports, drinking beer...

I would also like to thank Brahim Dkhil and Maud Giot, for their encouragement, help and kind attention.

I would also like to thank the laboratory engineers and technicians: Christine Bogicevic and Fabienne Karolak for their help in experiments, Gilles Boemare for the very time-costing TGA measurements, Jacques Chevreul, Bernard Fraisse and Nicolas Guibelin for XRD measurements, Pascale Geimener for FTIR, Françoise Garnier for SEM, and other people like Thierry Martin, Agnès Bénard, Fabien Debray, Obadias Mivumbi, Claire Roussel. Without their help, I could not have finished my thesis on time.

I would also like thank all Ph.D. students from the laboratory: Julie Carreaud, Julienne Chaigneau, Maël Guennou, David Albrecht, Bertrand Dupé, Lydie Louis, Mickaël Anoufa, Hongbo Liu, Pufeng Liu, Laijun Liu, ...

I would also like to thank Geraldine Carbonel and Catherine Lhopital from the secretariat de l' Ecole doctorale for their help, encouragement and kind attention.

Finally, I am eternally grateful to my family and my girlfriend for their forever support and love. You are always who I can count on, and you will always be.

# Résumé

L'objectif de ce travail était l'étude systématique de composés de type  $\text{BaSn}_{1-x}\text{M}_x\text{O}_{3-\delta}$  ( $\text{M} = \text{Y}, \text{Gd}, \text{Sc}, \text{In}, \dots$ ) pour lesquels des propriétés de conduction protonique étaient attendues. Nous avons tout d'abord développé une méthode de synthèse originale par polymérisation d'acide acrylique qui nous a permis d'obtenir des poudres nanométriques pures, puis des céramiques denses après frittage. Nous avons ensuite étudié l'influence de la nature et de la teneur en dopant sur les propriétés structurales et électriques. Cette étude expérimentale a été couplée à la modélisation semi-empirique qui nous a permis de prédire les défauts les plus probables au sein de la phase. Les résultats montrent que le modèle de substitution est étroitement lié à la taille des cations substituant. Pour les petits cations, une substitution totale sur le site B est calculée et observée alors que, pour les plus grosses terres rares (La, Nd et Sm), la modélisation anticipe une substitution partielle possible sur le site A confirmée par une anomalie dans l'évolution des paramètres de maille. Concernant les propriétés électriques, nous n'avons pas observé de tendances claires de l'évolution des propriétés électriques en fonction de la nature du cation. Il semble malgré tout que les dopants les meilleurs correspondent à ceux pour lesquels l'énergie d'association lacune-dopant est la plus faible. Dans le cas de l'yttrium, la conduction augmente avec le taux de substitution ce qui peut être relié à la fois à l'augmentation associée du nombre de porteurs et à l'évolution microstructurale. Nous montrons également que le taux de dopant a une forte influence sur la stabilité des matériaux produits. Ainsi, les composés fortement dopés sont instables sous atmosphère humide, alors que les composés faiblement dopés semblent stables sous atmosphère humide, riches en  $\text{H}_2$  ou  $\text{CO}_2$ . Finalement, nous avons montré que l'emploi de ZnO comme additif permettait d'abaisser fortement la température de frittage sans pour autant affecter les propriétés de transport. Cette étude a donc démontré que les composés de type  $\text{BaSn}_{1-x}\text{M}_x\text{O}_{3-\delta}$  ( $\text{M} = \text{Y}, \text{Gd}, \text{Sc}, \text{In}, \dots$ ) peuvent trouver des applications comme conducteurs protoniques pour peu que le taux de substituant soit limité pour des raisons de stabilité, que la taille de grains soit importante pour améliorer la conduction et le procédé de fabrication optimisé pour obtenir une forte densité.

# Abstract

The main objective of the present work was the systematic study of  $\text{BaSn}_{1-x}\text{M}_x\text{O}_{3-\delta}$  ( $\text{M} = \text{Y}, \text{Gd}, \text{Sc}, \text{In}, \dots$ ) as proton conductors. We first developed a synthesis route based on the acrylic acid polymerization. This allowed us obtaining pure nanopowders and dense ceramics after a classical sintering process. We then studied the influence of dopant nature and content on the structural and electrical properties. This study was coupled to theoretical calculations which helped us predicting the most probable defects within the structure. Results indicate that the substitution model is closely linked with dopant size. For small cations, the substitution on B-site occurs as foreseen by the original compound formula. For big cations (La, Nd and Sm), the modeling anticipates a possible partial substitution on A-site, confirmed by an anomaly observed on the evolution of cell parameters. Concerning electrical properties, we did not observe any significant trend as a function of dopant size. It seems nevertheless that best dopants in terms of anion or proton conduction are those presenting the smaller dopant-defect interaction energy as revealed by semi-empirical calculations. In the case of yttrium, the evolution of conduction with  $\text{Y}^{3+}$  content is linked both to the increase of charge carriers due to doping and to the increase of grain size with increasing dopant content. We also showed that the stability is strongly linked with the doping level. While highly doped compounds are unstable in humid atmosphere, slightly doped compounds present good stability in humid, hydrogen and  $\text{CO}_2$  containing atmosphere. Finally, we showed that ZnO as an additive could be used to lower the sintering temperature without changing the conduction properties. This study thus showed that  $\text{BaSn}_{1-x}\text{M}_x\text{O}_{3-\delta}$  ( $\text{M} = \text{Y}, \text{Gd}, \text{Sc}, \text{In}, \dots$ ) may find applications as proton conductors if dopant level is limited for stability reasons, grain size important for better conduction properties and the elaboration process optimised to ensure high density.

# Table of contents

<b>Acknowledgements</b> .....	I
<b>Abstract</b> .....	III
 <b>Chapter 1 Introduction</b>	
1.1 Solid oxide fuel cells.....	1
1.2 Proton conducting oxides: principle and defect chemistry.....	4
1.2.1 Proton defect formation.....	4
1.2.2 Hydration of acceptor-doped perovskite oxides.....	5
1.2.3 Proton transport.....	10
1.2.4 Effects of defect-acceptor dopant association.....	11
1.2.5 Isotope effect.....	12
1.2.6 Mixed conductivity in proton conductors.....	15
1.3 Proton conduction oxides: materials.....	17
1.3.1 Proton conductivity in acceptor-doped perovskite oxides.....	17
1.3.2 Proton conductivity in non-perovskite oxide and phosphates.....	20
1.3.3 Proton-conducting oxides: application in fuel cells	22
1.4 Barium stannate compounds.....	23
1.4.1 Synthesis.....	23
1.4.2 Properties and applications.....	27
1.5 Objectives.....	31
References.....	33
 <b>Chapter 2 Experimental Techniques</b> .....	
2.1 Introduction.....	39
2.2 Chemical and structural characterization.....	39

2.2.1 X-ray powder diffraction.....	39
2.2.2 Scanning electron microscope/Energy dispersive spectroscopy.....	39
2.2.3 Fourier transform infrared spectroscopy.....	40
2.2.4 Thermogravimetric analysis/Differential temperature analysis.....	40
2.3 Electrical characterization.....	41
2.3.1 The principle of AC impedance spectroscopy.....	41
2.3.2 Experimental method.....	44
2.4 Synthesis of ceramics oxides.....	44
2.4.1 Solid state reaction.....	45
2.4.2 Acrylic acid polymerization.....	45
2.4.3 Sintering.....	52
2.5 Conclusion.....	52
References.....	54
<b>Chapter 3 Synthesis, structure and electrical properties of <math>\text{BaSn}_{1-x}\text{M}_x\text{O}_{3-\delta}</math>.....</b>	<b>55</b>
3.1 Introduction.....	55
3.2 Structural properties of $\text{BaSn}_{1-x}\text{M}_x\text{O}_{3-\delta}$ compounds.....	56
3.3 Defect chemistry of doped $\text{BaSnO}_3$ .....	58
3.3.1 Evolution of cell parameters.....	58
3.3.2 Defect model versus cell parameters.....	59
3.3.3 Application to doped $\text{BaSnO}_3$ .....	60
3.4 Thermal expansion.....	62
3.5 Thermodynamics and transport properties of $\text{BaSn}_{1-x}\text{M}_x\text{O}_{3-\delta}$ .....	64
3.5.1 Microstructural and structural properties of samples.....	64
3.5.2 Water uptake.....	66
3.5.3 Transport properties.....	71
3.6 Conclusion.....	75
References.....	77

<b>Chapter 4 Structural, proton incorporation and conductivity of Y-doped BaSnO<sub>3</sub>...</b>	<b>78</b>
4.1 Introduction.....	78
4.2 Microstructural and structural properties.....	78
4.3 Thermodynamic analysis of water uptake.....	83
4.4 Transport properties.....	86
4.4.1 Analysis of impedance spectra.....	86
4.4.2 Transport properties as a function of P(O <sub>2</sub> ).....	87
4.4.3 Conductivities as a function of temperature in different atmospheres.....	89
4.4.4 Influence of Y <sup>3+</sup> content on conductivity.....	94
4.4.5 Isotope effect.....	98
4.5 Chemical stability.....	100
4.5.1 Stability in wet atmosphere/conditions.....	101
4.5.2 Stability in wet 5H <sub>2</sub> /Ar and CO <sub>2</sub> .....	105
4.6 Conclusion.....	106
References.....	108
<b>Chapter 5 Effect of ZnO additive on sintering and electrical properties of BaSn<sub>0.75</sub>Y<sub>0.25</sub>O<sub>3-δ</sub>.....</b>	<b>110</b>
5.1 Introduction.....	110
5.2 Part I: ZnO effect on pure phase formation and densification of BaSn <sub>0.75</sub> Y <sub>0.25</sub> O <sub>3-δ</sub> .....	111
5.2.1 Experimental.....	111
5.2.2 Results and discussions.....	112
5.2.3 Conclusion.....	114
5.3 Part II: ZnO as a sintering aid and a second dopant effects on microstructural and electrical properties of BaSn <sub>0.75</sub> Y <sub>0.25</sub> O <sub>3-δ</sub> compounds.....	114
5.3.1 Experimental .....	114
5.3.2 Results and discussions.....	115

5.4 Conclusion.....	123
Reference.....	124
<b>Chapter 6 Atomistic simulation of pure and doped BaSnO<sub>3</sub>.....</b>	<b>125</b>
6.1 Introduction.....	125
6.2 Methods.....	126
6.2.1 Atomistic simulation technique.....	126
6.2.2 Defective unit cell volumes.....	129
6.3 Results and discussions.....	130
6.3.1 Basic properties of BaSnO <sub>3</sub> .....	130
6.3.2 Intrinsic atomic defects.....	132
6.3.3 Redox reactions.....	133
6.3.4 Dopant-ion substitution.....	137
6.3.5 Defect volume and cell parameter.....	139
6.3.6 Defect association.....	141
6.3.7 Oxygen ion migration.....	143
6.4 Conclusion.....	146
References.....	148
<b>Chapter 7 Conclusion and perspective.....</b>	<b>150</b>
7.1 Conclusions.....	150
7.1.1 Resume of the main results.....	150
7.1.2 Comparison of barium stannate with typical proton conductors.....	151
7.2 Perspective.....	152
<b>Appendix.....</b>	<b>153</b>
A Résumé en Français.....	153

# Chapter 1 Introduction

## 1.1 Solid oxide fuel cells

Fuel cells are electrochemical devices that convert directly chemical energy present in fuels into electrical energy. They are a promising alternative to traditional power generation with high efficiency and low environmental impact. Because the intermediate steps of producing heat and mechanical work typical of most conventional power generation methods are avoided, fuel cells are not limited by thermodynamic limitations of heat engines such as the Carnot efficiency. Fuel cells differ from conventional rechargeable batteries: as long as the fuel and oxidant are supplied to the electrodes, the cell will continue to produce an electric current flowing from the anode (the negative electrode) to the cathode (positive electrode), as opposed to stored chemical energy. Fuel flexibility has been demonstrated using natural gas, biogas, coal gas *etc.* Fuel cells have a potentially wide variety of applications, such as transportation, stationary power plants, micropower generation, *etc.* Transportation markets worldwide have shown remarkable interest in fuel cells. Nearly all major vehicle manufacturers and energy providers are supporting their development [1].

Among the various kinds of fuel cells, Solid Oxide Fuel Cells (SOFCs) have shown tremendous reliability when operated continuously [2, 3]. In addition, such fuel cells offer the highest energy conversion efficiency and excellent fuel flexibility. However, several of the challenges hindering SOFC technology are a consequence of the high temperature (900-1000°C) required for their operation. This high temperature is used to overcome limitations of ionic conductivity in available solid electrolytes and of kinetics in available electrode materials [4]. The high operating temperature places severe constraints on materials selection, implies difficult fabrication processes, induces materials over cost, and reduces thermal cycling and fuel cell life.

In recognition of these challenges, there are presently major research efforts

ongoing to decrease the operating temperature of SOFC to moderate temperatures, *i.e.* from 500 to 800°C. Therefore, research has been focused on improving electrolyte material conductivity because a major part of fuel cell resistance is derived from the electrolyte resistance. Many families of oxygen conducting compounds have been thus explored but very few present at the same time good mechanical properties, chemical stability in both oxidative and reducing atmospheres, good ion conduction and poor electronic conduction. Another strategy consists in exploring proton conducting materials since the transport of protons is generally a low-activation energy process. This implies that the conductivities of compounds based upon proton conduction might be higher than that of compounds based upon oxygen ion conduction at low temperature. **Figure 1.1** illustrates this point showing the comparison of the conductivities of well known proton and oxide ion conducting oxides at different temperatures [5].

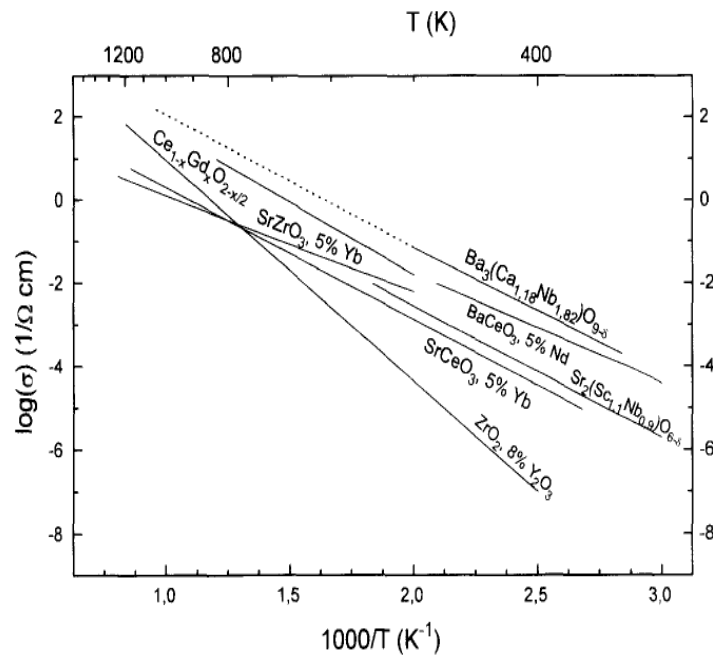


**Figure 1.1** Conductivity of some solid electrolyte oxides for SOFCs [5]

Iwahara *et al.* [6, 7] first demonstrated the existence of proton conduction in  $ABO_3$  perovskite compounds at elevated temperature, and then many families of compounds

have since then been explored, such as acceptor-doped perovskites oxides, binary rare earth oxides with fluorite-related structures or ternary oxides with pyrochlore structure. The experiments demonstrate that the highest proton conductivities are observed for perovskites oxides [8].

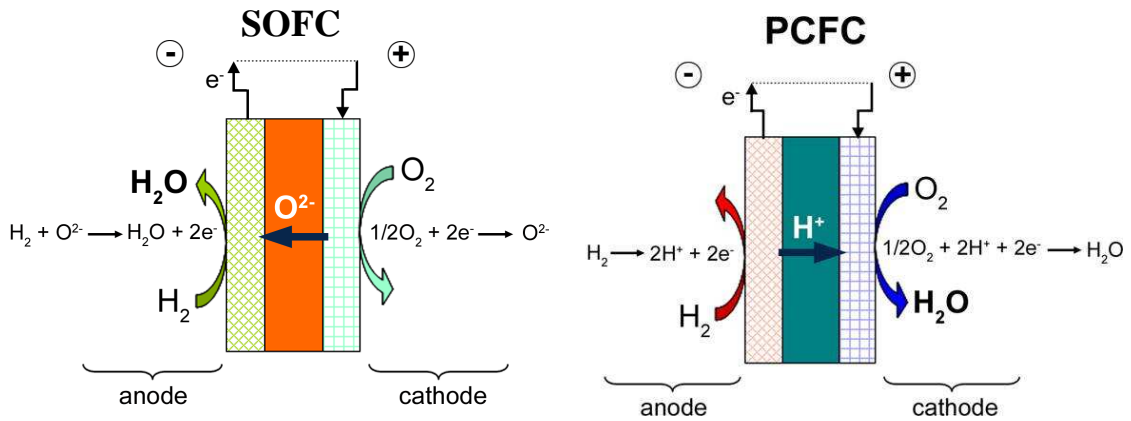


**Figure 1.2** The schematic presentations of unit cell of solid oxide fuel cell (SOFC) and proton conducting fuel cell (PCFC). (Note: the figures come from the Ideal Cell European Project draft)

Let us come back to the working principle of SOFC, as represented in **Figure 1.2**. In a classical SOFC based on anion-conducting electrolyte, the reduction of oxygen occurs at the cathode and the resulting  $O^{2-}$  anion is then transported across the electrolyte till the anode side, where it will combine with  $H_2$  gas to form gaseous water. The two half-reactions of oxidation/reduction involve exchanges of electrons that circulate in the external circuit. In Proton Conducting Fuel Cells (which is actually a kind of SOFC), hydrogen is oxidized into  $H^+$  and this  $H^+$  is carried out till the cathode through the proton-conducting electrolyte.  $H^+$  ions then react with  $O_2$  gas to form gaseous water. Intrinsically, the oxide ion-conducting fuel cell produces then water vapor on the anode side, which lowers the cell voltage, and reduces fuel utilization and requires considerable fuel circulation [4]. A proton-conducting fuel cell, on the other hand, produces water at the cathode. The high air flow usually used takes care of this, while the anode fuel gas remains undiluted by water vapor, keeping the Nernst voltage high [9].

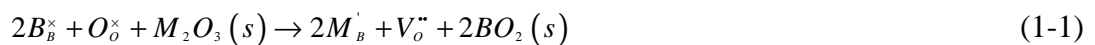
The major problem of ceramic proton conductors is their rather basic nature because Sr and Ba are often some of their components [9]. They are thus vulnerable to destructive reaction with acidic gases, such as CO<sub>2</sub> or SO<sub>2</sub>/SO<sub>3</sub>, especially at moderate temperature, and may also react with water at moderate and low temperatures to form hydroxides. All in all, proton conducting oxides are advantageous in intermediate or low temperature, and can be candidates for electrolyte materials for reducing the operation temperature of SOFCs.

## 1.2 Protonic conducting oxides: principle and defect chemistry

Protonic conducting oxides can be considered as electrolytes in which hydrogen ions are the major charge carriers. Protons, usually, are not part of the component of oxides. The requirements for the introduction of protonic defects into an oxide-based proton conductor can be simply stated as [10]: (1) It possesses an oxygen deficient lattice, either structurally, or via acceptor doping, (2) It can incorporate water at modest applied vapor pressures, *i.e.* < 1 atm., (3) It permits the rapid transport of protons once these have been “formed”.

### 1.2.1 Proton defect formation

For large band gap perovskite (ABO<sub>3</sub>) oxides, proton conduction almost exclusively involves acceptor-doped systems with charge-compensating oxygen vacancies in the dry state. When it is exposed to humidified atmosphere, the oxygen vacancies are replaced by hydroxyl groups, which means that protons are incorporated into perovskite structure, as shown in **Figure 1.3**, and the defect reactions are expressed in Kröger-Vink notation as following:



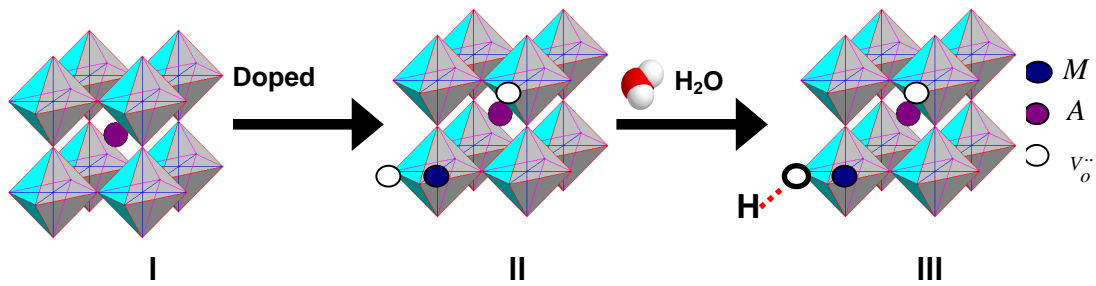


**Figure 1.3** Formation of proton defect: I) Perfect lattice, II) Introduction of oxygen vacancies, III) Formation of proton defect.

However, it is well known that non-stoichiometry, atmosphere, dopant nature *etc.*, greatly influence defect reaction and transport properties of proton conductors. For instance, for the typical proton conductors, *i.e.* barium cerate and barium zirconate, it has been reported that BaO evaporates easily from the surface of sintered pellets due to high sintering temperature [11], and some analysis also indicates the possible existence of an amorphous Ba-rich phase at grain boundaries [12]. Barium oxide deficiency may result in the trivalent ion residing on Ba-site. For instance, microanalysis of Nd-BaCeO<sub>3</sub> solid solutions indicated that the solutions could be represented by a general formul Ba<sub>1-x</sub>Nd<sub>x</sub>Ce<sub>1-y</sub>Nd<sub>y</sub>O<sub>3-(y-x)/2</sub>(V<sub>o</sub>'')<sub>(y-x)/2</sub> in which Nd is partitioned on both Ba and Ce sites [13]. The existence of Ba<sup>2+</sup>-site occupation has also been proposed by theoretical calculations for large dopants such as La, Nd and Sm in doped BaCeO<sub>3</sub> [14].



This reaction consumes oxygen vacancy instead of creating new vacancies, and thus might lower the protonic conductivity.

### 1.2.2 Hydration thermodynamics of acceptor-doped perovskite oxides

As mentioned above, when the doped perovskite oxide with oxygen vacancies is exposed to water atmosphere, oxygen vacancies are filled by hydroxyl ions as described **Eq. (1-2)**. The thermodynamics associated to **Eq. (1-2)** is an important parameter for describing proton conduction, which can evaluate the dissolution and concentration of

protons in the materials. The hydration thermodynamics of such reaction might be determined theoretically or experimentally basing on semi-empirical calculation and first-principles calculations or thermogravimetric and conduction data.

### 1.2.2.1 Theoretical calculations

The enthalpy of water incorporation has been calculated by semi-empirical calculation for typical proton conductors, such as BaCeO<sub>3</sub>, SrZrO<sub>3</sub> and CaZrO<sub>3</sub> compounds [14, 15]. Based on in Eq. (1-2). The enthalpy of water dissolution (proton incorporation),  $E_{H_2O}$ , can be calculated using the following equation [14, 15]:

$$E_{H_2O} = 2E(OH_o^\cdot) - E(V_o^{\cdot\cdot}) + E(PT) \quad (1-4)$$

Where,  $E(OH_o^\cdot)$  is the energy associated with substitution of  $O^{2-}$  with an  $OH$  group,  $E(V_o^{\cdot\cdot})$  the energy needed to create an isolated oxygen vacancy and  $E(PT)$  is the energy of proton exchange reaction at the surface, which hydroxide ions replace lattice oxygen ions:  $O^{2-} + H_2O(g) = 2OH^-$ . It is independent of the crystal structure, calculated to be -11.77 eV [15, 16].

The results calculated based on Eq. (1-4) indicate negative dissolution enthalpy, which signifies probable dominating proton conductivity at low temperature in these materials, which is consistent with the experimental conclusions. Of course, uncertainties in the absolute calculated values are important due to the limits of the very simplistic model employed. Nevertheless, there is reasonable quantitative accord with the few available experimental values [17].

Recently, the hydration energies of barium zirconate and barium stannate doped by various trivalent elements (Gd<sup>3+</sup>, In<sup>3+</sup>, Nd<sup>3+</sup>, Sc<sup>3+</sup> and Y<sup>3+</sup>) have been also calculated from first principles calculations with an “isolated defects” model as well as with a model considering the interaction energies between the dopants and oxygen vacancies/protons [18, 19]. The authors deduced hydration energies, within the framework of various models, and estimated the hydration Gibbs free energy by accounting for vibrational energetic and

entropic effects. In the case of Y-doped BaSnO<sub>3</sub>, the hydration energy (12.5 mol % Y doping) calculated is - 0.69 eV. The experimental enthalpy of 10 mol % Y-doped BaSnO<sub>3</sub> is - 0.62 eV, for 25 mol % of Y content it is - 0.83 eV, and for 50 mol % of Y content - 1.05 eV [20]. The results of computation are good agreement with the experimental results.

Unfortunately, the theoretical calculations are unable to evaluate the value of the hydration reaction entropy leading thus to some important uncertainty for the real temperature range of a material to work as a proton conductor.

### 1.2.2.2 Experimental access to hydration thermodynamics

To analyse hydration thermodynamics, the equilibrium expression for **Eq. (1-2)** between oxygen vacancies and water vapour to form protons is [21]:

$$K = \exp\left(\frac{\Delta S^\circ}{R}\right) \exp\left(-\frac{\Delta H^\circ}{RT}\right) = \frac{[OH_o^\cdot]^2}{([V_o^{\cdot\cdot}][O_o^x]P_{H_2O})} \quad (1-5)$$

Where, the square brackets denote molar fractions or volume concentrations (but in general not site fractions).

The electroneutral condition of acceptor-doped oxide with oxygen vacancies and protons is:

$$2[V_o^{\cdot\cdot}] + [OH_o^\cdot] = [Acc^\cdot] = \text{constant} \quad (1-6)$$

Where, *Acc* denotes acceptors in general. The approximation is made here that the concentration of holes/electrons is negligible.

If defect concentrations are small, we could assume that  $[O_o^x]$  equals the concentration of oxide ion sites,  $[O_o^x] + [V_o^{\cdot\cdot}] + [OH_o^\cdot] = [O] = \text{constant}$ . In molar concentration, for perovskites oxides,  $[O] = 3$ , then:

$$K = \frac{4[OH_o^\cdot]^2}{P_{H_2O} ([Acc^\cdot] - [OH_o^\cdot]) (6 - [Acc^\cdot] - [OH_o^\cdot])} \quad (1-7)$$

And the concentration of protonic defects as a function of  $P_{H_2O}$  and K is:

$$[OH_o^\cdot] = \frac{3Kp_{H_2O} - \sqrt{Kp_{H_2O} \left( 9Kp_{H_2O} - 6Kp_{H_2O} [Acc'] + Kp_{H_2O} [Acc']^2 + Kp_{H_2O} + 24[Acc'] - 4[Acc']^2 \right)}}{Kp_{H_2O} - 4} \quad (1-8)$$

Because the formation of protonic defects according to **Eq. (1-2)** is accompanied by a significant weight increase, the concentration of protonic defects as a function of temperature and water partial pressure is usually measured by thermogravimetric analysis (TGA), or indirectly by conductivity measurements. The fitting of experimental data to the model described above yields the equilibrium constant  $K$ , and  $K$  vs temperature is well described by **Eq. (1-5)** corresponding to an Arrhenius type behavior for  $K(T)$ , giving standard hydration enthalpies and entropies ( $\Delta H^\circ$  and  $\Delta S^\circ$ ) [8].

Hydration thermodynamic parameters are important in that they determine whether at a given temperature the material is primarily dominated by oxygen vacancies or protons [9]. The enthalpy of hydration (**Eq.1-2**) varies considerably, with some apparent correlation to materials properties.

Norby *et al.* [21, 22] reported that the enthalpy of hydration for rare earth sesquioxides becomes more negative as the oxide gets more stable, *i.e.*, as the enthalpy of formation gets more negative, the stable  $Y_2O_3$ ,  $Er_2O_3$  and  $Yb_2O_3$  thus contain protons up to very high temperatures, while less stable  $La_2O_3$  dehydrates even at very moderate temperatures. However, the mobility of protons decreases as their stability in the oxide increases, the highest proton conductivity being thus obtained as a compromise in the middle of the series, for  $Gd_2O_3$ .

In perovskite-related oxides, Kreuer *et al.* [8] suggested that the enthalpy of hydration reaction tends to become more negative with decreasing electronegativity of cations interacting with the lattice oxygen, *i.e.*, with decreasing Bronsted basicity of the oxide. Norby *et al.* [21] have developed a correlation between the hydration enthalpy and the difference  $\Delta X_{B-A}$  in electronegativity between the cations populating the B-site and the A-site of the perovskite. **Figure 1.4** shows precisely an update of this correlation plot [9]. A linear trend from the enthalpies can be presented roughly as:

$$\Delta H(\text{kJ} / \text{mol}) = -173(9) + 370(42)\Delta X_{B-A} \quad (1-9)$$

We will see in the following that this law is far from representing the behaviour of all perovskite compounds, in particular the behavior of acceptor-doped barium stannates. Indeed, from this calculation, barium stannates compounds should present a positive enthalpy (and thus no water uptake) for the hydration reaction which is of course very different from what observed.

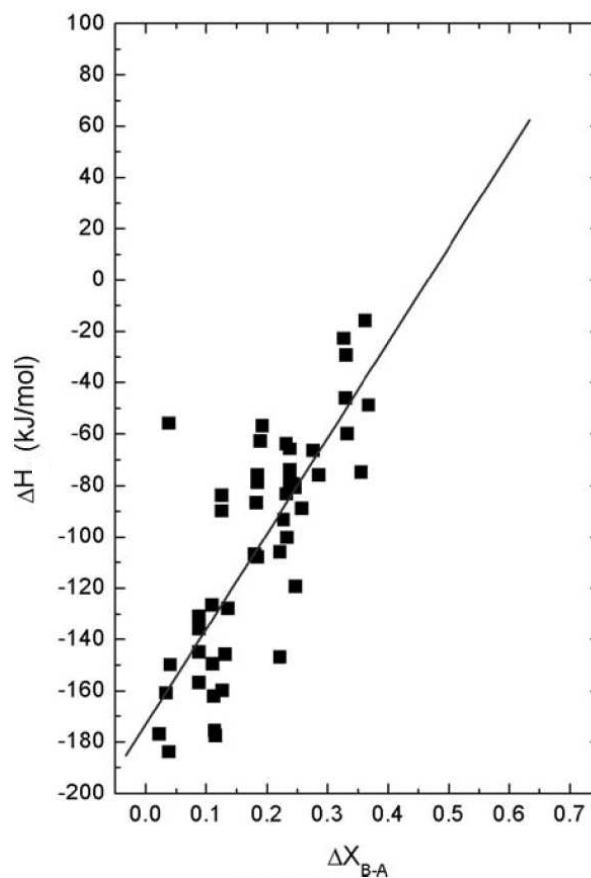


**Figure 1.4** Hydration enthalpy vs difference in Rochow-Allred electronegativities between B- and A-site constituents in perovskites [9].

The standard entropy change ( $\Delta S^\circ$ ) appears to end up around  $-120 \text{ J/mol}\cdot\text{K}$ , as expected empirically for the loss of 1 mol of gas [21]. Nevertheless, some perovskites, such as  $\text{BaCeO}_3$ , have large negative values (exothermic) of more than  $-150 \text{ J/mol}$ , and they are thus dominated by protons in wet atmospheres, and suppose a high temperature to

shift the equilibrium to the left. Others, such as  $\text{SrTiO}_3$ , have moderate negative entropies and are dominated by protons only at relatively low temperatures [9].

### 1.2.3 Proton transport

It is well known that proton transport includes transport of protons ( $\text{H}^+$ ) and any assembly that carries protons ( $\text{H}_3\text{O}^+$ ,  $\text{NH}_4^+$ ,  $\text{OH}^-$ , *et al.*). There are two principal mechanisms well recognized to describe the transport of proton: the vehicle mechanism and the Grotthuss mechanism [4, 8, 23-25].

For the vehicle mechanism, the proton moves together with a “vehicle” as a passenger on a larger ion ( $\text{H}_3\text{O}^+$ ,  $\text{NH}_4^+$ ,  $\text{OH}^-$ , *et al.*). This mechanism is mainly observed in aqueous solution, other liquids/metal, and compounds with loose bonded small molecules, which is usually restricted to materials with open structures (*i.e.* channels, layers) to allow the passage for the large ions and molecules.

The other mechanism is the so-called Grotthuss mechanism. This was proposed to explain the high diffusivity of  $\text{H}^+$  ions in water and involves the protons tunneling from one water molecule to the next via hydrogen bonding. This mechanism is thought to be at the origin of the high proton mobility in solid acid salts and proton conducting oxides. Actually, quantum MD simulations revealed the details of a typical Grotthuss mechanism in proton conducting perovskite oxides [17, 25, 26]. The protons, always residing on oxide host ions, exhibit thermal rotation and stretching vibrations. The principal features of the proton diffusion process are the rotational diffusion of the proton to set up the hydrogen bonds OH-O between the two oxide ions, the decrease of their distance, and the proton transfer towards the adjacent oxygen ion via stretching vibration. The rotational motion of the proton in the O-H group is rapid, which allows the reorientation of the proton towards the next oxygen ion before the transfer process. The transfer process was calculated to be the rate-limiting step in the considered perovskites. A typical proton diffusion trace as obtained from MD calculations is shown in **Figure1.5** [27].

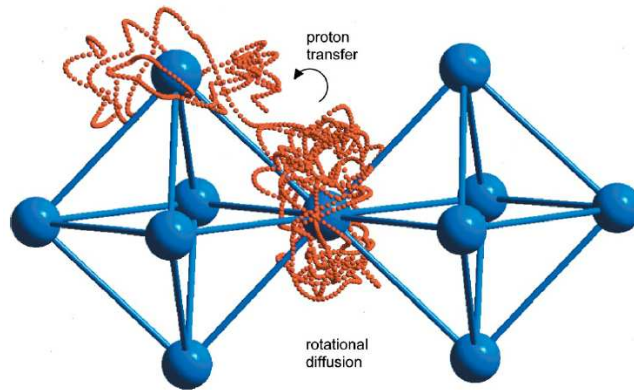


**Figure 1.5** The trace of a proton in a perovskite showing the two principal features of proton transport: rotational diffusion and proton transfer [27].

#### 1.2.4 Effects of defect-dopant association

The mutual association of the proton defects, oxide ions and metal cations in the proton conducting oxides comprises not only hydrogen bonding, but also stronger covalent and ionic interactions [25]. For instance, the association between oxygen vacancies and acceptor dopants has been reported to explain the non-Arrhenius behaviour of oxygen ion conduction in acceptor-doped oxides such as zirconia, ceria, lanthanum gallate, and others [21]. Oxygen vacancies associated to acceptor dopants can be written:



If the oxygen vacancies are trapped as associates, it will also influence the hydration thermodynamics. The hydration of the associate will be written [9]:



The oxygen vacancies are stabilized and the hydration enthalpy can perhaps be expected to be less favorable than that of the free vacancies, provided that the protons dissolved are less associated to the acceptor [9, 21].

Similar association between the proton and the dopant might also act in the opposite direction favouring a higher proton concentration, but giving a smaller mobility.

Protons will tend to be trapped by acceptors according to this equation [9]:



Kreuer *et al.* [28] found that BaZrO<sub>3</sub> doped with Y exhibits a lower activation energy and higher conductivity than with the same amount of Sc, while the hydration enthalpy of BaZrO<sub>3</sub> doped with Sc (-119.4 kJ/mole) is much more negative than with Y (-79.5 kJ/mole). They attributed this to oxide ions coordinated to Sc becoming more electron rich (basic), thus bonding protons more strongly. Islam *et al.* [29] also predicted that the lowest binding energy of hydroxyl-dopants is for Y and the strongest association is for Sc for BaZrO<sub>3</sub> as calculated by atomistic simulation, which is in agreement with Kreuer's results. All in all, it seems that there are effects of dopants, but trapping leading to associates is hardly evidenced experimentally in conductivity measurements so far [9].

### 1.2.5 Isotope effect [30-34]

Isotope effect is a major tool to confirm the protonic nature of conductivity in solid oxide conductors. The study of the isotope effect most often involves substitution of D for H. This produces a mass change by a factor of 2, which is far greater than that available from isotopes of other elements. Different theories have been developed to understand the mechanism of isotope effect, such as classical theory, semi-classical theory and tunneling theory.

The classical theory is adopted first to describe the isotope effect due to influence of the pre-exponential term of conductivity. The proton (or deuteron) "hops" from one lattice site to another over a potential energy barrier, as depicted in **Figure 1.6**, as a function of the configurational coordinate.

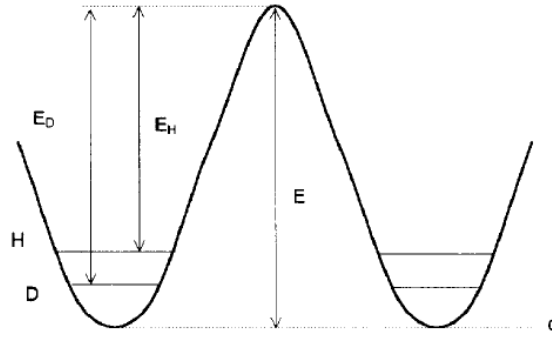


**Figure 1.6** Schematic diagram of potential barrier for a proton (or deuteron) transfer reaction as a function of the configurational coordinate of the hopping atom [30].

For an ionic conductor, the conductivity has an Arrhenius form described by:

$$\sigma = \frac{A}{T} \exp\left(-\frac{E_a}{kT}\right) \quad (1-13)$$

Where  $A$  is a pre-exponential term,  $T$  is the absolute temperature,  $k$  is Boltzmann constant and  $E_a$  is the activation energy. More specially, the pre-exponential term is described by:

$$A = \frac{zq^2 \lambda^2 \omega_o c_o}{6Vk} \quad (1-14)$$

Where,  $z$  is the number of directions in which the conductivity jump may occur,  $q$  is the charge of hopping ion,  $\lambda$  is the jump distance,  $c_o$  is the charge of hopping ion,  $V$  is the volume of unit cell,  $k$  is Boltzmann constant,  $\omega_o$  is the frequency factor, described by:

$$\omega_o = \nu_o \exp\left(\frac{\Delta S}{k}\right) \quad (1-15)$$

Where  $\Delta S$  is a vibrational entropy,  $\nu_o$  is an appropriate ‘attempt frequency’ which, for a light atom, involves an effective mass that falls close to the mass of the hopping atom. In the case where  $\nu_o$  is only the OH stretching frequency, a harmonic oscillator model is used, which yields the relationship  $\nu_o \propto 1/\sqrt{m}$  where  $m$  is the effective mass.

Therefore, the conductivity can be written as:

$$\sigma = \frac{A}{T} \exp\left(-\frac{E_a}{kT}\right) \propto \frac{1}{\sqrt{m}} \exp\left(-\frac{E_a}{kT}\right) \quad (1-16)$$

Thus, in the classical theory, the activation energy is independent of the isotope, and the effective mass is the only parameter that affects the conductivity. The heavier mass of deuteron compared with hydrogen leads to a lower conductivity which contributes to the observable isotope effect.

However, experimentally, the activation energy is in most cases different for hydrogen and deuteron with  $E_D > E_H$  as described by **Figure 1.6**. This suggests that the activation energy,  $E_a$ , sees some contributions from the isotope effect. Semi-classical theory, which takes the zero-energy difference into consideration, is adopted here. If the activated state is independent of the isotopic mass, we can expect for the activation energy difference:

$$E_D - E_H = \frac{1}{2}h(\nu_H - \nu_D) \quad (1-17)$$

For the *OH* ion in perovskite oxides, the OH stretching frequency  $\nu_H$  is close to  $10^{14} \text{ s}^{-1}$  [35], and with  $\nu_D / \nu_H = 1/\sqrt{2}$ , we obtain  $E_D - E_H \cong 0.055 \text{ eV}$ .

If the proton is the dominating charge carrier, the isotope effect will be clearly observable first from conductivities values, then from activation energies. Otherwise it can be concluded that the conductivity mechanism is not protonic.

In practice, both classical and non-classical isotope effects are encountered. For example, with  $\text{SrZr}_{0.94}\text{Y}_{0.06}\text{O}_{2.97}$ , Huang *et al.* [36] observed a classical isotope effect of  $\sqrt{2}$  from 150 to 500 °C, but this disappeared at higher temperatures, where electronic conductivity becomes dominant, while Scherban *et al.* [37] reported that  $\sigma_H / \sigma_D$  is close to 2.5 in 5 mol % Yb-doped  $\text{SrCeO}_3$  compound at room temperature, and concluded that protonic hopping follows a non-classical behavior. Initially, tunneling was suggested to explain how protons could overcome the strong bond to their host oxygen ions, and enhance proton diffusion at low temperature. However, tunneling was abandoned as the experimental evidence for the large isotope effects was proven wrong [38] and proton migration could be described by use of oxygen ion dynamics [21].

### 1.2.6 Mixed conductivity in proton conductors

Until now, we only considered ionic species as compensating charges in response to doping. Nevertheless, it is widely accepted and reported that the electrical properties of perovskite-type protonic conductors at temperatures above 700 °C are often characterised of course by oxygen ion conductivity but also by *n*- or *p*-type conductivity [39-41]. The relationship between the oxygen ion, *n*- and *p*-type electronic conductivities and oxygen partial pressure in acceptor-doped perovskite compounds, is presented in this section based on defect chemistry.

When trivalent dopants are incorporated into perovskite oxides, oxygen ion vacancies ( $V_o^{''}$ ) are created to maintain charge neutrality. In oxygen rich atmosphere, the oxygen vacancies tend to react with gaseous oxygen to produce electron holes:



On the opposite, at low oxygen partial pressure, the oxygen ions can leave their sub-lattice generating oxygen ion vacancies ( $V_o^{''}$ ) and electrons ( $e^{\cdot}$ ):



In hydrogen-free atmosphere and low water pressure, the electroneutrality equation, is given by:

$$2[V_o^{''}] + p = [M_B^{\cdot}] + n \quad (1-20)$$

There are three different Brouwer-type charge neutrality conditions, ( $e^{\cdot}, V_o^{''}$ ), ( $[M_B^{\cdot}], V_o^{''}$ ), ( $[M_B^{\cdot}], h^{\cdot}$ ) from low to high oxygen partial pressure [42]. However, for mostly proton conductor with high oxygen concentration formed by acceptor-dopant perovskite oxides,  $[M_B^{\cdot}] \gg p, n$ , with the concentration of oxygen vacancies fixed by [43]:

$$2[V_o^{''}] = [M_B^{\cdot}] = \text{constant} \quad (1-21)$$

Combining **Eqs. (1-18)-(1-21)**, the concentration of different charge carriers can

be expressed as:

$$p = h' = 2^{-\frac{1}{2}} K_{ox}^{\frac{1}{2}} [M_B']^{\frac{1}{2}} P_{O_2}^{\frac{1}{4}} \quad (1-22)$$

$$n = e' = 2^{-\frac{1}{2}} K_{red}^{\frac{1}{2}} [M_B']^{-\frac{1}{2}} P_{O_2}^{-\frac{1}{4}} \quad (1-23)$$

Where,  $K_{ox}$  and  $K_{red}$  are the equilibrium constant of **Eq. (1-18) and (1-19)**,  $p$ ,  $n$ ,  $[M_B']$  are the concentration of holes, electrons and dopant,  $p_{O_2}$  is the oxygen partial pressure.

The effective charge carriers consist then of oxygen vacancies, electrons and holes, which lead to oxygen ion, electronic and hole conductivity, respectively. The conductivity of mixed conductors is described as

$$\sigma_T = \sum \sigma_i = \sum q_i C_i B_i \quad (1-24)$$

Where  $\sigma_i$  is the conductivity component contributed by charge carrier species  $i$ ,  $C_i$  is the concentration of the charge carrier,  $q_i$  is the charge and  $B_i$  is the mobility of charge carrier species  $i$ . In most cases, the component  $C_i$  is the parameter that is modified by controlled atmosphere and chemical composition while the mobility  $B_i$  is essentially affected by temperature.

Combing **Eqs. (1-22)-(1-24)**, the conductivity of mixed conductors can also be described as [43]:

$$\sigma_T = A + B p_{O_2}^{-\frac{1}{4}} + C p_{O_2}^{\frac{1}{4}} \quad (1-25)$$

Where the first term ( $A$ ) is the  $p_{O_2}$  - independent oxygen ion conductivity, the second and the third terms are the contributions from electrons and electron holes, respectively. Given the total conductivities in different oxygen pressures at different temperatures, we can use **Eq. (1-25)** to fit the data and deconvolute and determine the ionic,  $p$ - and  $n$ -type conductivities as a function of temperature and oxygen partial pressure.

For proton conductors, we should also take into account proton defects at high water vapor pressure. When increasing oxygen partial pressure from low oxygen partial

pressure, three different charge neutrality conditions have to be considered *i.e.* the major defect pairs are changed sequentially from  $(e', OH_o^\bullet)$  to  $([M_B^\cdot], OH_o^\bullet)$ ,  $([M_B^\cdot], h')$  [42]. The dominant ionic defect shifts from  $V_o^{\bullet\bullet}$  to  $OH_o^\bullet$  as  $P(H_2O)$  increases at immediate oxygen pressure. In order to avoid a situation into which we have at the same time oxygen vacancies, holes and protons, we investigated the effect of dopants nature and contents on transport properties in an atmosphere (Argon) at which oxygen vacancies were measured to be the main charge carrier in dry atmosphere. It is nevertheless clear that at intermediate temperature in air, which is actually the atmosphere encountered at cathode side in fuel cells, the coexistence of holes and protons beside that of oxygen vacancies should be considered.

### 1.3 Proton conducting oxides: Materials

#### 1.3.1 Proton conductivity in acceptor-doped perovskite oxides

Perovskite oxides offer in almost all respects a wide variety of properties because of the structure ability to host varying cations, substitutions, non-stoichiometry, and defects of many kinds. Proton conductivity is found in a range of perovskites oxides,  $ABO_3$ . Perovskite-type oxides have the general formula  $A^{2+}B^{4+}O_3$  <sup>(1)</sup>, where A can be group IIA element or transition metal in the +2 oxidation state, and B is a transition metal, Ce, Zr, Sn, Ti in the +4 oxidation state. The structure of perovskites-type oxide (*i.e.*  $BaSnO_3$ ) is described in **Figure 1.7**. In the cubic perovskite structure, A ions occupy the corners of the elementary cell, the B ions the volume center and  $O^{2-}$  ions the surface center. In this structure, the larger  $A^{2+}$  and the  $O^{2-}$  ions build a cubic densest ball packing together and a quarter of the octahedral holes is filled with small  $B^{4+}$  ions. Each  $A^{2+}$  ion is coordinated with 12  $O^{2-}$  ions, each  $O^{2-}$  ion is surrounded by four  $A^{2+}$  ions and two  $B^{4+}$  ions. The octahedrons of  $(BO_6)$  are linked by sharing corners structure can distort and deform under definite conditions so that the structure symmetry degree is lowered. **Figure 1.8** show the partial proton conductivity for a number of acceptor-doped perovskites,

<sup>1</sup>  $A^{+1}B^{+5}O_3$ ,  $A^{+3}B^{+3}O_3$  or  $B^{+6}O_3$  can also exist.

calculated from data for proton mobility and thermodynamics of hydration [9].

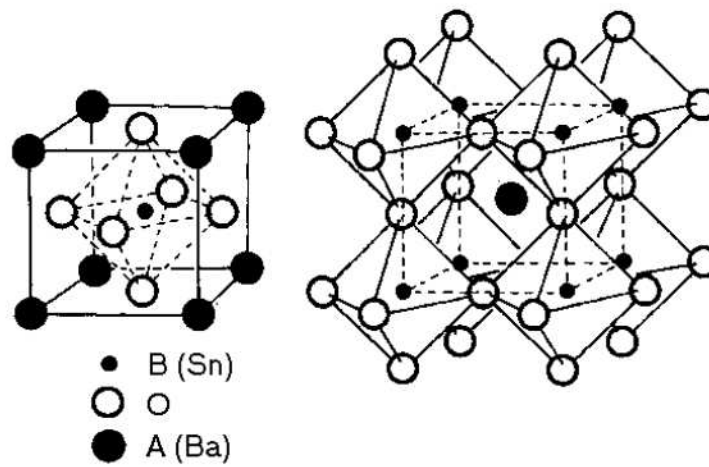


**Figure 1.7** Perovskite structure of  $\text{BaSnO}_3$

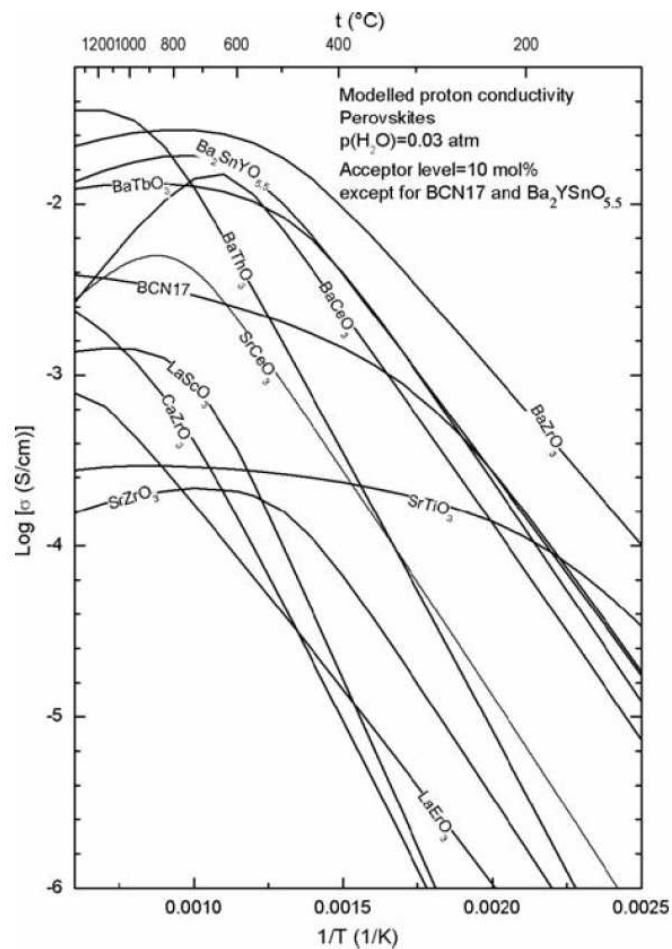


**Figure 1.8** Partial proton conductivity vs.  $1/T$  for bulk of selected perovskites at  $P(\text{H}_2\text{O}) = 0.03$  atm, calculated on basis of proton mobility and hydration thermodynamics parameters [9].

Among II-IV perovskites ( $A^{2+}B^{4+}O_3$ ), a recent analysis of available data provided the following guidelines for the composition of perovskite with high proton conductivity and good thermodynamics stability [44]: (1) Except for the stability with acidic gases, which is almost independent of the choice of the A-cation, all relevant properties are superior for an A-site occupation by barium compared to other alkaline earth ions. (2) The choice of B-cation, however, requires some compromise. The B-cations should be of medium size with an amphoteric nature and should form no significant covalent bonds with oxygen ligands. Small B-cations lead to high packing densities and reduce the water solubility, while large B-cations reduce the thermodynamics stability. It is well known that cerates and zirconates exhibit large negative hydration enthalpies and small activation energies for proton migration. Among these materials, Gd-substituted BaCeO<sub>3</sub> exhibits the highest protonic conductivity, *i.e.*  $\sim 0.05 \text{ S}\cdot\text{cm}^{-1}$  at 600 °C, temperature at which protons are the main charge carriers [45, 46]. This makes barium cerate considered as a potential candidate for fuel cell electrolyte. However, its long-term stability remains a concern in the presence of CO<sub>2</sub> and water-containing atmosphere [45, 47]. BaCeO<sub>3</sub> and SrCeO<sub>3</sub> react with CO<sub>2</sub> to form carbonates, and form alkaline earth hydroxides at high water activities. Of course, this excludes the use of any hydrocarbons from being used as fuels because this inevitably leads to the production of some CO<sub>2</sub> and H<sub>2</sub>O. The stability of cerates can be increased by chemical modifications, *i.e.* by partially replacing Ce by Zr ( $\geq 0.4$ ), although the proton conductivity will decrease with increasing Zr content [48-50]. The developments of these materials require thus to find a compromise between conductivity and stability characteristics.

Zirconates [33, 51, 52], in particular Y-doped BaZrO<sub>3</sub> combine high bulk proton conductivity with high thermodynamics stability (they are stable in acidic media and CO<sub>2</sub>). At low temperature ( $< 700 \text{ }^\circ\text{C}$ ) under wet atmosphere, the bulk conductivity of Y-doped BaZrO<sub>3</sub> is even slightly higher than the proton conductivity of BaCeO<sub>3</sub>-based oxides [8], and is considered to be a good candidate electrolyte material in the intermediate-temperature range. However, low sinterability and high grain boundary impedance are two

major problems, which is unfavorable to make these materials commercial. If these problems are solved, BaZrO<sub>3</sub> can be an excellent electrolyte material for intermediate temperature fuel cells [53].

Other ABO<sub>3</sub> perovskites, such as praseodymiate [54, 55], hafnate [56], thorates and terbates [57] (B site occupied by Pr, Hf, Th and Tb, respectively) were also studied as new proton conducting materials. They readily incorporate some protons at intermediate temperature but their conductivity is limited or in part due to hole contribution.

Among III-III perovskites ( $A^{3+}B^{3+}O_3$ ), La<sup>3+</sup> is the only common A-site cation, B is Sc<sup>3+</sup>, Y<sup>3+</sup>, In<sup>3+</sup>, Er<sup>3+</sup> *et al.* [58-64]. Of these, LaScO<sub>3</sub> hydrates well but exhibits medium proton mobility and a proton conductivity peaking just above 10<sup>-3</sup> S/cm. LaYO<sub>3</sub> and LaErO<sub>3</sub> are also perovskite related, but with lower tolerance factors and lower conductivity.

“Complex perovskites” represent another family of compounds, and usually suppose two B-site cations of different valence, typically in simple ratio to form a certain valence sums. Nowick and coworkers introduced this new class of complex perovskites as oxide ion and proton conductors in which the B-site cation ordering is essential [35, 65, 66]. These complex perovskites have the general formula  $A_2(B'_{1+x}B''_{1-x})O_{6-\delta}$  and  $A_3(B'_{1+x}B''_{2-x})O_{9-\delta}$ , both of which have two different ions occupying B-sites. In both cases, the A ions is charged 2+, in the former compound B' is 3+ and B'' is 5+, while in the later, B' is 2+ and B'' is 5+, respectively. Thus, the average charge on the B-site is 4+ in both cases. By changing the ratio of B' to B'' ions, oxygen vacancies can be formed intrinsically, and can then induce proton defects under wet atmosphere, *e.g.*  $Ba_3Ca'_{1+x}Nb''_{2-x}O_{9-\delta}$  or  $Sr_3Ca'_{1+x}Nb''_{2-x}O_{9-\delta}$  [35]. They were found to combine both good chemical stability and high conductivity.

### 1.3.2 Proton conductivity in non-perovskite oxide and phosphates

Proton conduction is also observed for many non-perovskite classes of oxides, comprising fluorite-related structures and structures with oxide ion tetrahedral. Among the

fluorite-related oxides, the  $\text{MO}_2$  oxides ( $\text{M} = \text{Zr}, \text{Hf}$  and  $\text{Ce}$ ) exhibit very little bulk solubility of protons [9], and the acceptor-doped oxides remain pure oxide ion conductors with negligible proton conductivity at all temperatures.

Proton conductivity in acceptor doped and undoped  $\text{Ln}_6\text{WO}_{12}$  ( $\text{Ln} = \text{La}, \text{Nd}, \text{Gd}$  and  $\text{Er}$ ) has recently been studied. The structure of the tungstate can be described as an ordered defective fluorite or a disordered pyrochlore [67, 68]. Undoped  $\text{La}_6\text{WO}_{12}$  exhibits proton conductivity peaking at  $5 \times 10^{-3}$  S/cm in wet hydrogen at  $900^\circ\text{C}$  [69]. The major disadvantage with the rare-earth tungstates with respect to applications is the chemical stability. Reaction with C-containing species may affect the tungstates, since the formation of  $\text{WC}_x$  is very stable. The volatility of  $\text{WO}_x$  is another problem, in particular, during the fabrication. Some other acceptor-doped pyrochlores, *i.e.*  $\text{La}_2\text{Zr}_2\text{O}_7$ , exhibit quite high and pure proton conductivity in wet atmospheres [70].

Proton conductivity in rare-earth sesquioxides were systematically studied within the framework of a consistent description of their defect chemistry by Norby *et al.* [22, 71, 72]. Sesquioxides are more stable in  $\text{CO}_2$ -containing atmosphere, but show more than one order of magnitude lower proton conductivity than  $\text{BaCeO}_3$ -based perovskites compounds [73]. The maximum conductivity,  $7.5 \times 10^{-4}$  S/cm, was observed for Ca-doped  $\text{Gd}_2\text{O}_3$  ( $900^\circ\text{C}$ ).

Acceptor-doped rare earth phosphates,  $\text{LnPO}_4$  ( $\text{Ln} = \text{La}, \text{Ce}, \text{Pr}, \text{Nd}, \text{Sm}$  with the monoclinic monazite-type structure, and  $\text{Ln} = \text{Y}$  with the tetragonal xenotime-type structure), form another class of  $\text{CO}_2$ -tolerant materials with appreciable proton conductivity [74-78]. Sr-doped  $\text{LaP}_3\text{O}_7$  has been studied due to its relatively high conductivity and especially because the protonic conduction appeared to be dominating even under low  $\text{P}(\text{H}_2\text{O})$  conditions [79].

Acceptor-doped rare earth orthoniobates and orthotantalates,  $\text{LnNbO}_4$  and  $\text{LnTaO}_4$ , have been recently investigated as more stable proton-conducting materials by Haugsrud and Norby [80]. The proton conductivity is dominated in these materials in wet atmospheres, and the highest conductivity was found for Ca-doped  $\text{LaNbO}_4$ ,  $\sim 0.001$  S/cm

at 950 °C with  $P(\text{H}_2\text{O}) = 0.025 \text{ Pa}$  [73]. Also  $\text{La}_3\text{NbO}_7$  shows similar proton conduction [81]. These materials are proved to be stable in  $\text{CO}_2$ -containing atmosphere, thus they are interesting candidates to operate, for example, using reformed natural gas.

### 1.3.3 Proton-conducting oxides: application in fuel cells

The development of proton-conducting oxides for fuel cell have stranded by the conflict between high proton conductivity and chemical and electrochemical stability under fuel cell operating conditions, *i.e.* acceptor-doped  $\text{BaCeO}_3$  shows the highest proton conductivity, but the long stability in water and  $\text{CO}_2$ -containing atmosphere becomes a problem [45, 47]. The electrolytes based on  $\text{BaZrO}_3$  exhibit good stability, but the conductivity is not high. Additional problems are related to the insufficient knowledge and research on electrodes for these new fuel cells [9]. However, due to the advantages of proton-conducting oxides fuel cells at intermediate temperature, more and more research institutions and companies have devoted to research and development on the proton-conducting oxide fuel cells.

Ito *et al.* [82] made a laboratory fuel cell with a 0.7  $\mu\text{m}$ -thick, Y-doped  $\text{BaCeO}_3$  electrolyte deposited on a Pd anode substrate (40  $\mu\text{m}$ ) and with a perovskite cathode. The cell showed high power densities, 1.4  $\text{W}/\text{cm}^2$  at 600 °C and 0.9  $\text{W}/\text{cm}^2$  at as low as 400 °C. This performance is higher than typical polymer exchange fuel cells and as high as that of high temperature SOFCs, even though it is operated at intermediate temperatures, but substantial lifetimes were not reported.

Meng *et al.* [83] reported the power density of the cell using 50  $\mu\text{m}$  films of Gd-doped  $\text{BaCeO}_3$  (BGCO) as electrolyte,  $\text{La}_{0.5}\text{Sr}_{0.5}\text{CoO}_3$ -BGCO as cathode, Ni-BGCO cermets as anode, is around 300  $\text{mW}/\text{cm}^2$  at about 700°C for industrial ammonia or  $\text{H}_2$  as fuel. This work shows how the unstable  $\text{BaCeO}_3$  may be used with a basic fuel such as ammonia. It is very interesting and promising for application in fuel cells.

Acceptor-doped mixed barium zirconate cerates  $\text{Ba}(\text{Zr,Ce})\text{O}_3$  have been investigated for their better stability of the zirconate combined with the better conduction

of cerate, but fuel cell tests have not given convincing results [84, 85].

## 1.4 Barium Stannate Compounds

Barium stannate with formula  $BaSnO_3$  belongs to the family of perovskite compounds like the best protons conductors  $BaCeO_3$  or  $BaZrO_3$ . Until now, quite few studies have been published on this compound in spite of the potential interest in many applications. In this part, we thus give some details on the synthesis of  $BaSnO_3$  and on the envisaged applications for  $BaSnO_3$ , in particular as proton conductors. This will allow introducing the objective of our study.

### 1.4.1 Synthesis

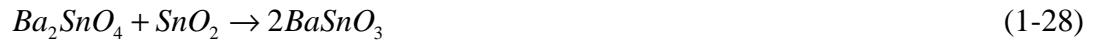
Barium stannate for the applications detailed below is almost always prepared via solid state reaction. It requires high temperature (above 1000 °C), results in coarse-grained powders and leads to very poor densification after sintering. In recent years, many preparation procedures have been developed to obtain fine-grained  $BaSnO_3$  powders at relatively low temperatures. We describe some of them below insisting on the success (or not) of the methods to favour sintering.

#### 1.4.1.1 Solid state reaction

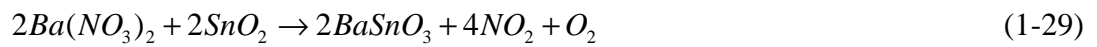
$BaSnO_3$  is conventionally prepared by ceramic solid state reaction through sintering of  $BaCO_3$  and  $SnO_2$  at a high temperature ranging from 1000 °C to 1400 °C according to equation [86, 87]:



If the stoichiometric mixture of  $BaCO_3$  and  $SnO_2$  powders is heated at a temperature between 900 °C and 1000°C,  $Ba_2SnO_4$  not  $BaSnO_3$  is first formed as **Eq.(1-27)**, and it reacts continually at 1100°C to form  $BaSnO_3$ . Single phase  $BaSnO_3$  appears in the sample after being sintered at 1200°C for 2 h. The reactions are described as follows [88]:



To lower the preparation temperature, Azad and Hon [86] employed barium nitrate to substitute barium carbonate and successfully prepared BaSnO<sub>3</sub> at 1000°C. The formation of BaSnO<sub>3</sub> from metal nitrates via solid state reaction is assumed to take place as follows:



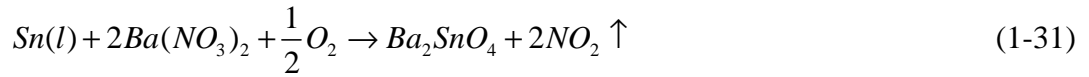
In this case, the mixture of raw materials was ball milled for 4 h, then calcined first at 800°C for 8 h and fired again at 1000°C for 24 h. The traditional several repetitions of “crush and calcination” steps are thus avoided in this modified route.

**However, up to date, a high degree of densification in the solid-state derived BaSnO<sub>3</sub> samples has not been achieved. The relative density of sintered bodies is only up to 70-80 % of the theoretical value even in samples sintered at 1600 °C for 12 h.**

#### 1.4.1.2 Self-heat-sustained (SHS) method [86]

The self-propagating or self-heat-sustained synthesis is an attractive and viable alternative to the conventional methods of advanced materials production in the field of ceramic- and metal-matrix composites. In the self-heat-sustained process for preparing barium stannate, metallic tin powder is intimately mixed with anhydrous Ba(NO<sub>3</sub>)<sub>2</sub>. Tin can disperse uniformly in Ba(NO<sub>3</sub>)<sub>2</sub> when heated at 250°C due to the low melting point of metallic tin (232°C). The compound formation was found to have initiated at about 800°C via an intermediate Ba-rich phase, Ba<sub>2</sub>SnO<sub>4</sub> as in solid state reaction. In the initial stages, molten metallic tin reacts as in **Eq. (1-30) and (1-31)**. The Ba-rich phase subsequently reacts with more Sn or SnO<sub>2</sub> to form BaSnO<sub>3</sub> as **Eq. (1-32) and (1-33)**.

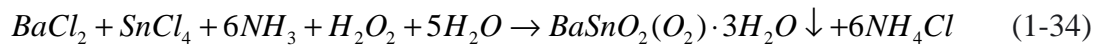




**The SHS derived BaSnO<sub>3</sub> powders could be well densified (near zero porosity) sintered at 1600°C for 2 h with uniform particle size (1-2 μm) and good microstructural features.**

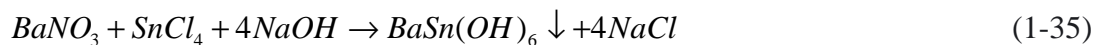
#### 1.4.1.3 Coprecipitation method

It consists of preparing an aqueous solution containing the desired cations and then mixing with another solution which contains the precipitating agent. The precipitated product is separated from the liquid by filtration, dried and thermally treated to attain the desired compounds. The BaSnO<sub>3</sub> powders were synthesized from peroxoprecursor, which is precipitated by adding BaCl<sub>2</sub> and SnCl<sub>4</sub> solution to a solution of ammonia and H<sub>2</sub>O<sub>2</sub> in water as follows [89]:



The peroxo-precursor calcined at 900°C for 1 h forms pure BaSnO<sub>3</sub> powder with uniform small particles sizes (50 to 200 nm) and high specific surface area (14 m<sup>2</sup>/g). The powders are very sinterable since 93% of the theoretical density is reached after sintering at 1400°C for 4 h.

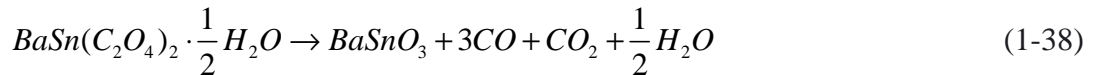
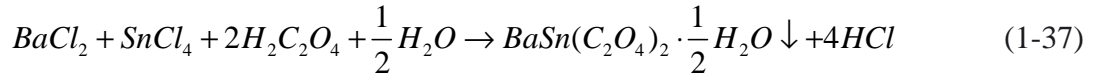
It has also been reported that BaSnO<sub>3</sub> can be prepared by coprecipitation of tin chloride and barium nitrate solutions [90] by adding NaOH precipitating agent.



The dried precipitation is mainly composed of BaSn(OH)<sub>6</sub>, which is poorly crystallised. After calcining at 600°C, the pure cubic BaSnO<sub>3</sub> phase forms as follows:



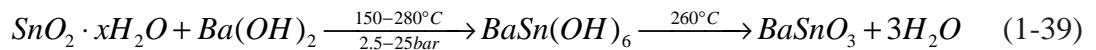
Oxalic acid has also been used as a precipitating agent by Bao *et al.* [91] for preparing BaSnO<sub>3</sub>. The chemical reactions during synthesis processing are described as follows:



The oxalate precursor converts to pure BaSnO<sub>3</sub> when treated at 1000 °C with less than 0.2 μm particle sizes.

#### 1.4.1.4 Hydrothermal synthesis method

Hydrothermal synthesis has been widely employed to prepare ceramic powders. The BaSnO<sub>3</sub> preparation via hydrothermal synthesis route, used stannic hydroxide gel ( $SnO_2 \cdot xH_2O$ ) which was freshly precipitated from tin chloride solution by addition of ammonia, and  $Ba(OH)_2$  solution as starting materials. The mixture was then handled in a Teflon-lined autoclave at a temperature between 150°C and 280°C. The as-prepared powder was the hydrated phase  $BaSn(OH)_6$ . On heating in air or on heating the pressure of the autoclave in situ at about 260°C, this hydrated phase converted into fine BaSnO<sub>3</sub> powders. The whole process is presented as follows:



The advantage of this method for the preparation of BaSnO<sub>3</sub> lies in the very low process temperature (260°C). Such a temperature makes possible to keep the nano size and very high specific surface area.

#### 1.4.1.5 Polymerized complex method

Polymerized complex method is widely applied for preparation of the multi-component oxides, and is also called modified Pechini method. The advantage of the

method lies in the limitation of segregation of different metal ions, which is achieved by forming stable metal-chelate complexes by polymerization [92].

The  $\text{BaSnO}_3$  and  $(\text{Ba}_x\text{Sr}_{1-x})\text{SnO}_3$  powders were synthesized by Udawatte *et al.* [92, 93] by polymerized complex method,  $\text{SnCl}_4 \cdot x\text{HO}$  and  $\text{BaCO}_3$  as starting materials, citric acid and ethylene glycol ( $\text{C}_2\text{H}_6\text{O}_2$ ) as chelating agent and polymerization agent. The polymerization was promoted among citric acid and ethylene glycol heated continually at  $135^\circ\text{C}$ , and attained the gel (transparent brown resin) with no precipitation. The resin was pyrolyzed at  $350^\circ\text{C}$  for 3 h in static air. The powders thus formed are called “precursor”. The precursor heated at  $600^\circ\text{C}$  for 2 h in static air contained tiny needle-like crystals of  $\text{BaCO}_3$  among aggregated  $\text{BaSnO}_3$  fine powder with definite morphology. When the powder was heated at  $800^\circ\text{C}$  for 2 h in static air, somewhat larger particles ranging from 80 to 100 nm in size were observed with faceted morphology but no needle-like  $\text{BaCO}_3$  crystals.

Licheron *et al.* [94] dissolved tin chloride in distilled water and stabilized it with chelating agent to prevent hydrolysis or condensation. They then mixed it with  $\text{BaCO}_3$  and citric acid. The obtained transparent solution was neutralized by addition of ammonia. It was then added acrylamide and N, N, N', N'- tetramethylethylenediamine. The mixed solution was thereafter heated at  $80^\circ\text{C}$ , and the gelification occurred in a few minutes after introducing N-N'-methylene-bis-azobisisobutyronitrile (AIBN). This aqueous gel was transformed into powders by calcination in air at  $600^\circ\text{C}$  for 5 h. The powders converts into pure  $\text{BaSnO}_3$  calcined at  $1000^\circ\text{C}$  for 12 h.

The method we used in the present study is very similar to polyacrylamide polymerization but uses much less toxic organic species (monomers or initiator). We will give more details in *Chapter 2*.

#### 1.4.2 Properties and applications

Barium stannate is known to have a perfectly cubic perovskite structure at room temperature (space group:  $Pm\bar{3}m$ ). The lattice constant of  $\text{BaSnO}_3$  is  $a = 4.116 \text{ \AA}$ , and the

thermal expansion coefficient is  $9.6 \times 10^{-6} \text{ K}^{-1}$  (200 K-800 K) [95], The X-ray density measured at 25°C is  $7.238 \text{ g/cm}^3$ . Barium stannate attracts some attention in material technology with good chemical and physical properties. It can be used to prepare thermally stable capacitors and to fabricate ceramic boundary layer capacitors [96], solid state sensor [97, 98], electrochemical devices [44, 99-101] and photoelectrochemical applications [102-104].

#### 1.4.2.1 Capacitors

Barium stannate is paraelectric and nonferroelectric [105]. The dielectric coefficient ( $\epsilon'$ ) and dielectric loss factor  $\delta$  varies in the range of 14 to 15 and 0.0001 to 0.001 respectively under the frequencies from  $10^2$  to  $10^5$  Hz and the temperatures from -200 to 400 °C [88]. Bevillon *et al.* [95] reported that the dielectric constant measured at 10 kHz is around 40, and also showed no significant evolution with temperature between 10 K and room temperature. The capacity is barely dependent on frequency at normal temperature in the region from  $10^2$  to  $10^6$  Hz [88]. With its characteristic dielectric properties, BaSnO<sub>3</sub> has been used to prepare thermally stable capacitors [96].

Barium stannate titanate compounds are important for practical application in ceramic capacitors as well as in functionally graded materials [106, 107]. The increase of Sn-substitution on Ti-sites leads to an increase of dielectric constant, while the Curie point shifts to a lower temperature. Furthermore, the multilayer barium stannate titanate ceramics have a relatively high dielectric constant in a wide temperature range [107, 108].

#### 1.4.2.2 Sensors

In recent years, BaSnO<sub>3</sub> compounds have attracted more and more attention as a sensor material since its electrical properties such as conductivity, resistance or impedance are dependent on oxygen partial pressure, the nature of the measured gases and their concentrations [109]. Based on these properties, many gas sensor devices made from BaSnO<sub>3</sub> powder have been developed. For instance, sensors based on BaSnO<sub>3</sub> are sensitive to a variety of gases, *i.e.* a maximum sensitivity for CO in the temperature range

of 600-700°C [110], NO in the temperature range of 450-550°C [97], and other gas including H<sub>2</sub>, CH<sub>4</sub>, CO and O<sub>2</sub>; their best sensitivities were obtained at temperatures below 700°C [111, 112]. Tao *et al.* [90] reported that a sensor made of BaSnO<sub>3</sub> also exhibits low response to LPG and petrol, but a high response and good selectivity to ethanol, and was proposed as a promising ethanol sensor. Chu reported that BaSnO<sub>3</sub> sensor exhibits a high sensitivity and good selectivity to dilute CH<sub>3</sub>S gas (0.01 ppm) at 300°C [113]. The gas-sensing properties of BaSnO<sub>3</sub> are thought a surface reaction process [110]. Therefore, the gas-sensing properties of BaSnO<sub>3</sub>, to a certain extent, depend on the surface state of the sensitive layer, which relates to the preparation process. Therefore, to achieve high gas sensitivity, BaSnO<sub>3</sub> is usually fabricated at reduced temperature or as a thin film.

The wide diversity of tested gases and the lack of explanations to relate gas sensing properties to structural and chemical features of BaSnO<sub>3</sub> make doubting about the real selectivity of BaSnO<sub>3</sub> gas sensors. This nevertheless reflects a probable evolution of conductivity with  $P(O_2)$  and a possible high reactivity of the material surface.

### 1.4.2.3 Photocatalysts

The photocatalytic production of hydrogen via direct photodecomposition of water over oxide semiconductors has attracted much attention for the solar energy conversion and environment preservation. Cubic BaSnO<sub>3</sub> has also been suggested to have promising potentialities in photoelectrochemical applications due to its  $d^{10}$  electronic configuration and to its band gap ( $\approx 3.4$  eV) close to those of classical photocatalysts [104, 114]. Borse *et al.* [104] reported that the Pb-substitution on Sn site can convert visible-light-inactive BaSnO<sub>3</sub> into a visible-light-active photocatalyst for O<sub>2</sub> production through the electronic structure tuning, *i.e.* the BaPb<sub>0.8</sub>Sn<sub>0.2</sub>O<sub>3</sub> system produce 32  $\mu$  mol/h of O<sub>2</sub> under  $\lambda \geq 420$  nm photons, while no O<sub>2</sub> for pure BaSnO<sub>3</sub>. Yuan *et al.* [115] showed that Sr substitution on the A site in BaSnO<sub>3</sub> enhances greatly H<sub>2</sub> evolution rate, and theoretical calculation reveals that strontium substitution not only pushes up the bottom of the conduction band but also increases the contribution of the Sr 5s orbitals to the bottom of the conduction

band. Recently, the theoretical electronic structure calculation based on density functional theory of  $\text{Ba}(\text{M}_{0.5}\text{Sn}_{0.5})\text{O}_3$  with some tetravalent metal ions, *i.e.*  $\text{M} = \text{Ti}, \text{V}, \text{Cr}, \text{Zr}, \text{Ce}$  and  $\text{Pb}$ , shows that the comparison of computed optical absorption coefficients can be arranged for  $\text{M}$ : *i)*  $\text{Cr} > \text{V} > \text{Ti}$  and *ii)*  $\text{Pb} > \text{Ce} > \text{Zr}$  [114].

#### 1.4.2.4 Proton conductors

$\text{BaSnO}_3$  has recently been proposed as a protonic conductor [20, 44, 99] with potential applications in fuel cells, when  $\text{Sn}$  is partially substituted by trivalent metals ( $\text{Y}$  [44] and  $\text{In}$  [99]), and activated by reaction with ambient moisture. 50 mol %  $\text{Y}$ -doped  $\text{BaSnO}_3$  can be hydrated (enthalpy is  $-101.5 \text{ kJ mol}^{-1}$ ) to a high degree which leads to the formation of protonic charge carriers and the occurrence of very high proton conductivity with low activation enthalpy ( $E_a = 0.51 \text{ eV}$ ) comparable to that of  $\text{BaCeO}_3$  based materials (see **Figure 1.8**) and rather good stability in  $\text{CO}_2$ -contained atmosphere [44]. Xie *et al.* [116] reported that  $\text{Sn}$  substitution  $\text{Ce}$  site in  $\text{BaCe}_{0.8}\text{Y}_{0.2}\text{O}_{3-\delta}$  enhances the chemical stability in  $\text{CO}_2$ -containing atmosphere and sinterability, and also shows good conductivity, *i.e.* the conductivity of  $\text{BaCe}_{0.7}\text{Sn}_{0.1}\text{Y}_{0.2}\text{O}_{3-\delta}$  reaches  $0.007 \text{ S/cm}$  at  $700 \text{ }^\circ\text{C}$ . The hydration properties of barium stannate doped by trivalent elements (12.5%) investigated by density-functional calculations shows that  $\text{Y}$ -,  $\text{In}$ - and  $\text{La}$ -doped  $\text{BaSnO}_3$  exhibit more negative hydration energies than other trivalent dopants, *i.e.*  $-0.71 \text{ eV}$  for  $\text{In}$ ,  $-0.69 \text{ eV}$  for  $\text{Y}$ , and  $-1.02$  for  $\text{La}$  [19]. In the case of  $\text{Y}$ , the hydration energy of  $\text{Y}$ -doped  $\text{BaSnO}_3$  changes with  $\text{Y}$  contents, *i.e.*  $-0.62 \text{ eV}$  for 10 mol %, and  $-0.83 \text{ eV}$  for 25 mol % [20].

However, the experiment results also indicated that  $\text{Ba}_2\text{SnYO}_{5.5}$  compound exhibits the collapse of the structure and the formation of a brownmillerite phase upon reduction, and the macrocracking induced by lattice strain resulting from hydration due to the high concentration of oxygen ion vacancies [44].

## 1.5 Objectives

Despite the possible interest of barium stannate oxides in the field of proton conductors, as mentioned above, there are only few studies dealing with these properties. Barium stannate compounds seem to present levels of proton conductivity sufficient for fuel cells applications and applications could be envisaged if their stability, in particular, in humidified reducing atmosphere, do not impede their use.

Taking into account the possible advantages and problems of barium stannate as a proton conductor, we decided to start a systematic study of barium stannate with trivalent dopant elements for the point of view of defect chemistry, chemical stability, transport properties, and suitability for fuel cells. This let us to get further insight into the following points:

### 1. Preparation of doped barium stannate by gel polymerization

$\text{BaSn}_{1-x}\text{M}_x\text{O}_{3-\delta}$  ( $x = 0.125$  and  $0.25$ ,  $M = \text{Fe}, \text{Sc}, \text{In}, \text{Y}, \text{Gd}, \text{Sm}, \text{Nd}$  and  $\text{La}$ ) were synthesized using gel polymerization. The chemical and physical properties of raw powder samples were characterized using X-ray powder diffraction (XRD), scanning electronic microscopy (SEM) and thermogravimetry to optimize the experimental conditions for pure powder preparation.

### 2. Site incorporation selectivity in pure and doped barium stannate

Site incorporation selectivity was analyzed by the evolution lattice parameters and incorporation energies of doped barium stannate. Empirical defect model and atomistic simulation are combined to comprehensively study the question of site incorporation selectivity.

### 3. Impact of dopants on hydration energy of doped barium stannate

The enthalpy and entropy of doped barium stannate were obtained by thermogravimetric analysis, and thereafter the impact of dopants and contents on hydration energy was studied.

### 4. Proton conductivities of doped barium stannate

The conductivities of doped barium stannate were investigated under different atmospheres (wet and dry Ar, Air and H<sub>2</sub>, different oxygen pressures) by AC impedance spectroscopy (IS), to probe the effect of dopants properties and contents, and atmosphere on the electron, hole, oxygen ion and proton conductivities of doped barium stannate.

### **5. Chemical stability of doped barium stannate**

The chemical stability of doped barium stannate was investigated in different atmospheres and conditions, *i.e.* H<sub>2</sub>O- and CO<sub>2</sub>-rich atmospheres.

### **6. Optimisation of sintering through ZnO addition**

The conductivity and sinterability of doped barium stannate with ZnO as a sintering aid and as a second dopant were investigated, anticipating that ZnO can decrease the sintering temperature, without affecting the conductivity.

## References

- [1] U.S. Department of Energy Office of Fossil Energy, Fuel Cell Handbook (7ed), **2004**.
- [2] S. M. Haile, *Acta Materialia* **2003**, *51*, 5981.
- [3] A. H. Brian C.H.Steele, *Nature* **2001**, *414*, 345.
- [4] N. Bonanos, *Solid State Ionics* **1992**, *53-56*, 967.
- [5] R. Hempelmann, *Physica B: Condensed Matter* **1996**, *226*, 72.
- [6] H. Iwahara, T. Esaka, H. Uchida, N. Maeda, *Solid State Ionics* **1981**, *3-4*, 359.
- [7] H. Iwahara, H. Uchida, S. Tanaka, *Solid State Ionics* **1983**, *9-10*, 1021.
- [8] K. D. Kreuer, *Ann. Rev. Mater. Res.* **2003**, *33*, 333.
- [9] T. Ishihara, *Perovskite Oxide for Solid Oxide Fuel Cells (Fuel Cells and Hydrogen Energy)*, Springer, **2009**.
- [10] N. Bonanos, *Solid State Ionics* **2001**, *145*, 265.
- [11] P. Babilo, T. Uda, S. M. Haile, *Journal of Materials Research* **2007**, *22*, 1322.
- [12] J. Wu, L. P. Li, W. T. P. Espinosa, S. M. Haile, *J. Mat. Res.* **2004**, 2366.
- [13] D. Makovec, Z. Samardzija, D. Kolar, *Journal of the American Ceramic Society* **1997**, *80*, 3145.
- [14] R. Glockner, M. S. Islam, T. Norby, *Solid State Ionics* **1999**, *122*, 145.
- [15] R. A. Davies, M. S. Islam, J. D. Gale, *Solid State Ionics* **1999**, *126*, 323.
- [16] C. R. A. Catlow, *Journal of Physics and Chemistry of Solids* **1977**, *38*, 1131.
- [17] M. S. Islam, *Journal of Materials Chemistry* **2000**, *10*, 1027.
- [18] P. G. Sundell, M. E. Bjorketun, G. Wahnstrom, *Physical Review B* **2006**, *73*, 104112.
- [19] E. Bevilion, G. Geneste, *Physical Review B* **2008**, *77*, 184113.
- [20] K. D. Kreuer, *Solid State Ionics* **1999**, *125*, 285.
- [21] T. Norby, M. Widerøe, R. Glöckner, *Dalton Trans* **2004**, 3012.
- [22] Y. Larring, T. Norby, *Solid State Ionics* **1995**, *77*, 147.
- [23] T. Norby, *Solid State Ionics* **1999**, *125*, 1.
- [24] K. D. Kreuer, *Chem.Mater* **1996**, 610.

- [25] K. D. Kreuer, *Solid State Ionics* **2000**, 136-137, 149.
- [26] W. Munch, K. D. Kreuer, G. Seifertli, J. Majer, *Solid State Ionics* **1999**, 125, 39.
- [27] W. Munch, G. Seifert, K. D. Kreuer, J. Maier, *Solid State Ionics* **1996**, 86-88, 647.
- [28] K. D. Kreuer, S. Adams, W. Munch, A. Fuchs, U. Klock, J. Maier, *Solid State Ionics* **2001**, 145, 295.
- [29] M. S. Islam, P. R. Slater, J. R. Tolchard, T. Dinges, *Dalton Transactions* **2004**, 3061.
- [30] A. S. Nowick, A. V. Vaysleyb, *Solid State Ionics* **1997**, 97, 17.
- [31] T. Scherban, Y. M. Baikov, E. K. Shalkova, *Solid State Ionics* **1993**, 66, 159.
- [32] J. F. Liu, A. S. Nowick, *Solid State Ionics* **1992**, 50, 131.
- [33] H. H. Huang, M. Ishigame, S. Shin, *Solid State Ionics* **1991**, 47, 251.
- [34] T. Norby, M. Friesel, B. E. Mallander, *Solid State Ionics* **1995**, 77, 105.
- [35] A. S. Nowick, Y. Du, *Solid State Ionics* **1995**, 77, 137.
- [36] S. Shin, H. H. Huang, M. Ishigame, H. Iwahara, *Solid State Ionics* **1990**, 40-41, 910.
- [37] T. Scherban, W. K. Lee, A. S. Nowick, *Solid State Ionics* **1988**, 28-30, 585.
- [38] T. Norby, M. Friesel, B. E. Mellander, *Solid State Ionics* **1995**, 77, 105.
- [39] A. N. Virkar, H. S. Maiti, *Journal of Power Sources* **1985**, 14, 295.
- [40] M. K. Paria, H. S. Maiti, *Solid State Ionics* **1984**, 13, 285.
- [41] N. Bonanos, B. Ellis, M. N. Mahmood, *Solid State Ionics* **1988**, 28-30, 579.
- [42] S. Song, E. D. Wachsman, S. E. Dorris, U. Balachandran, *Solid State Ionics* **2002**, 149, 1.
- [43] I. Kosacki, H. L. Tuller, *Solid State Ionics* **1995**, 80, 223.
- [44] P. Murugaraj, K. D. Kreuer, T. He, T. Schober, J. Maier, *Solid State Ionics* **1997**, 98, 1.
- [45] S. V. Bhide, A. V. Virkar, *Journal of The Electrochemical Society* **1999**, 146, 2038.
- [46] N. Taniguchi, K. Hatoh, J. Niikura, T. Gamo, H. Iwahara, *Solid State Ionics* **1992**, 53-56, 998.
- [47] N. Bonanos, K. S. Knight, B. Ellis, *Solid State Ionics* **1995**, 79, 161.
- [48] K. Katahira, Y. Kohchi, T. Shimura, H. Iwahara, *Solid State Ionics* **2000**, 138, 91.
- [49] J. Lv, L. Wang, D. Lei, H. Guo, R. V. Kumar, *Journal of Alloys and Compounds* **2009**,

467, 376.

[50] K. H. Ryu, S. M. Haile, *Solid State Ionics* **1999**, 125, 355.

[51] H. Iwahara, T. Yajima, T. Hibino, K. Ozaki, H. Suzuki, *Solid State Ionics* **1993**, 61, 65.

[52] R. C. T. Slade, S. D. Flint, N. Singh, *Solid State Ionics* **1995**, 82, 135.

[53] N. Ito, H. Matsumoto, Y. Kawasaki, S. Okada, T. Ishihara, *Solid State Ionics* **2008**, 179, 324.

[54] A. Magraso, F. Espiell, M. Segarra, J. T. S. Irvine, *Journal of Power Sources* **2007**, 169, 53.

[55] S. Mimuro, S. Shibako, Y. Oyama, K. Kobayashi, T. Higuchi, S. Shin, S. Yamaguchi, *Solid State Ionics* **2007**, 178, 641.

[56] F. M. M. Snijkers, A. Buekenhoudt, J. J. Luyten, J. Cooymans, M. Mertens, *Scripta Materialia* **2004**, 51, 1129.

[57] K. A. Furoy, R. Haugsrud, M. Hansel, A. Magraso, T. Norby, *Solid State Ionics* **2007**, 178, 461.

[58] E. Ruiz-Trejo, J. A. Kilner, *Solid State Ionics* **1997**, 97, 529.

[59] H. Fujii, Y. Katayama, T. Shimura, H. Iwahara, *Journal of Electroceramics* **1998**, 2, 119.

[60] D. Lybye, N. Bonanos, *Solid State Ionics* **1999**, 125, 339.

[61] S. Kim, K. H. Lee, H. L. Lee, *Solid State Ionics* **2001**, 144, 109.

[62] K. Nomura, T. Takeuchi, S. Tanase, H. Kageyama, K. Tanimoto, Y. Miyazaki, *Solid State Ionics* **2002**, 154-155, 647.

[63] K. Nomura, T. Takeuchi, S.-i. Kamo, H. Kageyama, Y. Miyazaki, *Solid State Ionics* **2004**, 175, 553.

[64] J. Liu, Y. Chiba, J. Kawamura, H. Yugami, *Solid State Ionics* **2006**, 177, 2329.

[65] K. C. Liang, A. S. Nowick, *Solid State Ionics* **1993**, 61, 77.

[66] K. C. Liang, Y. Du, A. S. Nowick, *Solid State Ionics* **1994**, 69, 117.

[67] N. Diot, O. Larcher, R. Marchand, J. Y. Kempf, P. Macaudière, *Journal of Alloys and Compounds* **2001**, 323-324, 45.

- [68] R. Haugrud, *Solid State Ionics* **2007**, 178, 555.
- [69] T. Shimura, S. Fujimoto, H. Iwahara, *Solid State Ionics* **2001**, 143, 117.
- [70] T. Shimura, M. Komori, H. Iwahara, *Solid State Ionics* **1996**, 86-88, 685.
- [71] T. Norby, P. Kofstad, *Solid State Ionics* **1986**, 20, 169.
- [72] T. Norby, O. Dyrlye, P. Kofstad, *Solid State Ionics* **1992**, 53-56, 446.
- [73] R. Haugrud, T. Norby, *Solid State Ionics* **2006**, 177, 1129.
- [74] K. Amezawa, Y. Kitajima, Y. Tomii, N. Yamamoto, M. Widerye, T. Norby, *Solid State Ionics* **2005**, 176, 2867.
- [75] K. Amezawa, H. Maekawa, Y. Tomii, N. Yamamoto, *Solid State Ionics* **2001**, 145, 233.
- [76] T. Norby, N. Christiansen, *Solid State Ionics* **1995**, 77, 240.
- [77] N. Kitamura, K. Amezawa, Y. Tomii, T. Hanada, N. Yamamoto, *Solid State Ionics* **2005**, 176, 2875.
- [78] K. Amezawa, Y. Tomii, N. Yamamoto, *Solid State Ionics* **2003**, 162-163, 175.
- [79] K. Amezawa, Y. Uchimoto, Y. Tomii, *Solid State Ionics* **2006**, 177, 2407.
- [80] R. Haugrud, T. Norby, *Nature Materials* **2006**, 5, 193.
- [81] T. Shimura, Y. Tokiwa, H. Iwahara, *Solid State Ionics* **2002**, 154-155, 653.
- [82] N. Ito, M. Iijima, K. Kimura, S. Iguchi, *Journal of Power Sources* **2005**, 152, 200.
- [83] G. Meng, G. Ma, Q. Ma, R. Peng, X. Liu, *Solid State Ionics* **2007**, 178, 697.
- [84] E. Fabbri, A. D'Epifanio, E. Di Bartolomeo, S. Licoccia, E. Traversa, *Solid State Ionics* **2008**, 179, 558.
- [85] Y. Guo, Y. Lin, R. Ran, Z. Shao, *Journal of Power Sources* **2009**, 193, 400.
- [86] A. M. Azad, N. C. Hon, *Journal of Alloys and Compounds* **1998**, 270, 95.
- [87] S. Upadhyay, O. Parkash, D. Kumar, *J. Mater. Sci. Lett.* **1997**, 16, 1330.
- [88] W. Lu, in *Lehrstuhl fuer Neue Materialien*, Universitaet des Saarlandes, **2002**.
- [89] G. Pfaff, *Journal of the European Ceramic Society* **1993**, 12, 159.
- [90] S. Tao, F. Gao, X. Liu, O. T. Sorensen, *Sensors and Actuators B: Chemical* **2000**, 71, 223.
- [91] M. BAO, W. LI, *J. Mater. Sci.* **1993**, 28, 6617.

- [92] C. P. Udawatte, M. Kakihana, M. Yoshimura, *Solid State Ionics* **1998**, 108, 23.
- [93] C. P. Udawatte, M. Kakihana, M. Yoshimura, *Solid State Ionics* **2000**, 128, 217.
- [94] M. Licheron, G. Jouan, E. Husson, *Journal of the European Ceramic Society* **1997**, 17, 1453.
- [95] E. Bévillon, A. Chesnaud, Y. Wang, G. Dezanneau, G. Geneste, *J. Phys.: Condens. Matter* **2008**, 145217
- [96] E. C. Subbarao, *Ferroelectrics* **1981**, 35, 143.
- [97] U. Lampe, J. Gerblinger, H. Meixner, *Sensors and Actuators B: Chemical* **1995**, 26, 97.
- [98] V. Jayaraman, G. Mangamma, T. Gnanasekaran, G. Periaswami, *Solid State Ionics* **1996**, 86-88, 1111.
- [99] T. Schober, *Solid State Ionics* **1998**, 109, 1.
- [100] V. Thangadurai, P. Schmid Beurmann, W. Weppner, *Materials Science and Engineering B* **2003**, 100, 18.
- [101] V. Thangadurai, P. Schmid-Beurmann, W. Weppner, *Materials Research Bulletin* **2002**, 37, 599.
- [102] P. H. Borse, J. S. Lee, H. G. Kim, *Journal of Applied Physics* **2006**, 100, 124915.
- [103] W. F. Zhang, J. Tang, J. Ye, *Chemical Physics Letters* **2006**, 418, 174.
- [104] P. H. Borse, U. A. Joshi, S. M. Ji, J. S. Jang, J. S. Lee, E. D. Jeong, H. G. Kim, *Applied Physics Letters* **2007**, 90, 034103.
- [105] X. Wei, Y. Feng, X. Yao, *Applied Physics Letters* **2003**, 83, 2031.
- [106] R. Steinhausen, A. Kouvatov, H. Beige, H. T. Langhammer, H. P. Abicht, *Journal of the European Ceramic Society* **2004**, 24, 1677.
- [107] S. Markovic, M. Mitric, N. Cvjeticanin, D. Uskokovic, *Journal of the European Ceramic Society* **2007**, 27, 505.
- [108] X. Wei, X. Yao, *Materials Science and Engineering: B* **2007**, 137, 184.
- [109] B. Ostrick, M. Fleischer, H. Meixner, *Journal of the American Ceramic Society* **1997**, 80, 2153.

- [110] U. Lampe, J. Gerblinger, H. Meixner, *Sensors and Actuators B: Chemical* **1995**, 25, 657.
- [111] B. Ostrick, M. Fleischer, U. Lampe, H. Meixner, *Sensors and Actuators B: Chemical* **1997**, 44, 601.
- [112] J. Cerda, J. Arbiol, G. Dezanneau, R. Dvaz, J. R. Morante, *Sensors and Actuators B: Chemical* **2002**, 84, 21.
- [113] X. Chu, *Materials Science and Engineering B* **2004**, 106, 305.
- [114] P. H. Borse, J. S. Lee, H. G. Kim, *Journal of Applied Physics* **2006**, 100, 124915.
- [115] Y. Yuan, J. Lv, X. Jiang, Z. Li, T. Yu, Z. Zou, J. Ye, *Applied Physics Letters* **2007**, 91, 094107.
- [116] K. Xie, R. Yan, X. Chen, S. Wang, Y. Jiang, X. Liu, G. Meng, *Journal of Alloys and Compounds* **2009**, 473, 323.

# Chapter 2 Experimental Techniques

## 2.1 Introduction

In this chapter, the experimental techniques and processing method used for the characterisation and fabrication of powders and sintered pellets in this thesis are explained in detail.

## 2.2 Chemical and structural characterization

### 2.2.1 X-ray powder diffraction (XRD)

X-ray powder diffraction is an essential technique for phase identification and crystal structure refinement. XRD data obtained in this work were collected at room temperature and under ambient conditions with Siemens D-5000 powder diffractometer using Cu  $K_{\alpha 1+2}$  radiation ( $\lambda = 1.5418 \text{ \AA}$ ) and an applied voltage and current of 35 kV and 40 mA, respectively. The data were collected, in the  $2\theta$  region from  $20^\circ$  to  $60^\circ$  in  $2\theta$  with  $0.03^\circ$  for  $2\theta$ -step and 5 s/step for powders, and  $2\theta$  region from  $20^\circ$  to  $110^\circ$  in  $2\theta$  with  $0.02^\circ$  for  $2\theta$ -step and 8 s/step for pellets. For pellets at different temperatures, each pattern was recorded in vacuum on a high accuracy two-axis diffraction meter, in a Bragg-Brentano geometry, using Cu  $K_{\alpha 1+2}$  radiation filtered with a nickel foil to remove Cu  $K_\beta$  as X-ray source which is generated by a 18 kW rotating anode. Both phase identification and lattice parameter refinement were performed using DIFFRACplus Eva [1] and Topas [2], and Cellref V3 [3] programs, respectively.

### 2.2.2 Scanning electron microscope/Energy dispersive spectroscopy (SEM/EDS)

Scanning electron microscope in conjunction with EDS was used to examine microstructure and chemical feature of sintered samples. Samples' morphologies were observed using a Hitachi S-4700 scanning electron microscope operating at 5 kV. At the same time, EDS was utilized with a link system digital spectrometer PFT (Princeton Gamma Tech, PRISM) to determine compositional difference between bulk and grain

boundary regions of selected sintered pellets. For microstructural characterisation of sintered bodies, the surface and fracture of samples were observed. Samples surfaces were previously polished using SiC papers until the surfaces of optical quality were obtained, and then were etched thermally at 50 °C below the sintering temperature for 5 min with a heating rate of 2 °C/min. To allow their observation, a fine layer of gold metal was deposited onto the sample by radio frequency sputtering.

### 2.2.3 Fourier transform infrared spectroscopy (FTIR)

FTIR spectroscopy was performed on a Bruker IFS66 spectrometer in flowing nitrogen, in order to detect the evolution of precursor phase with thermal treatment temperature. Calcined powders were diluted in optically transparent KBr and pressed into pellets (sample: KBr mass ratio of 1:300). Various beam splitters and detectors were used to optimally cover the range from 4000  $\text{cm}^{-1}$  to 100  $\text{cm}^{-1}$ , from the far infrared to mid infrared range.

### 2.2.4 Thermogravimetric analysis/differential temperature analysis (TGA/DTA)

The behavior of compounds as a function of temperature was probed by TGA/DTA (SETARAM TG/DSC, Model 92-1750). Thermal analysis was utilized for the characterization of decomposition behaviour of powder precursors and proton incorporation.

For decomposition of doped  $\text{BaSnO}_3$  precursor, thermogravimetric analyses were performed on a small quantity (~17 mg) of precursor. They have been carried out using the same instrument (with alumina crucible as reference) to observe the decomposition behaviour and to determine the lowest calcination temperature. These analyses have been undertaken in a flowing air, from room temperature (RT) to 1400°C, with a heating and cooling rate of 10 °C/min.

For the detection of proton incorporation, TGA was performed in flowing wet Ar with constant water pressure 21 Kpa (50 % water gas pressure at 30°C). The powders (~1g) were first shaped as pellets using low pressure. The sample was first treated under dry

Ar at 1200°C during 2h at heat rate 5°C/min, to desorb water and remove the barium carbonate from the surface completely. The mass gain was then measured at different temperatures under wet Ar. During each measurement, the temperature and water pressure was kept constant and keeping enough time to make the water hydration reaction reach chemical equilibrium. Above 600°C, the step in temperature was 100°C, and below 600°C, the temperature step was 50°C.

For the calculation of proton concentration, the apparent change of mass must be corrected taking account of “buoyancy effect” since the samples are suspended in a variable atmosphere (its density changes with temperature and water content) during TGA measurements. The apparent mass difference between two measurements temperature  $T_0$  and  $T_1$ , can be corrected as:

$$\Delta m = \Delta m_{real} + V(\rho_1 - \rho_0) \quad (2-1)$$

Where  $V$  is the volume of the sample, and determined simply using the theoretical density of the material.  $\rho_1$  and  $\rho_0$  are the densities of wet Ar at  $T_1$  and  $T_0$  respectively.

## 2.3 Electrical characterisation

### 2.3.1 The principle of AC impedance spectroscopy (IS)

Alternating current (AC) impedance spectroscopy is widely used in characterising electrical properties of materials and their interface with electronically conducting electrodes [4]. The interest of AC impedance spectroscopy lies in its effectiveness in isolating individual reaction/migration steps in a multistep process. This is, because each electrode and electrolyte (grain and grain boundary) process has, ideally, a unique time constant associated with it. Accordingly the relaxation frequency range for each process should also be different. If the relaxation frequency range for each of the process is widely separated, their respective contributions can be separated in the frequency domain [5].

Experimentally, this technique is based on applying a sinusoidal voltage frequency and very small amplitude over the sample, and measuring the corresponding voltage

response. The current through the electrolyte must remain small, in order to avoid polarization problems and/or to irreversibly damage the material. The ratio of the voltage response to the current perturbation is the impedance ( $Z$ ).

The quantity used for expressing models of impedance is the complex number, defined as:

$$Z = Z' + jZ'' \quad (2-2)$$

Where, the real part of the impedance ( $Z'$ ) comprises the resistive component ( $R$ ), the imaginary part ( $Z''$ ), includes capacitive and inductive components.

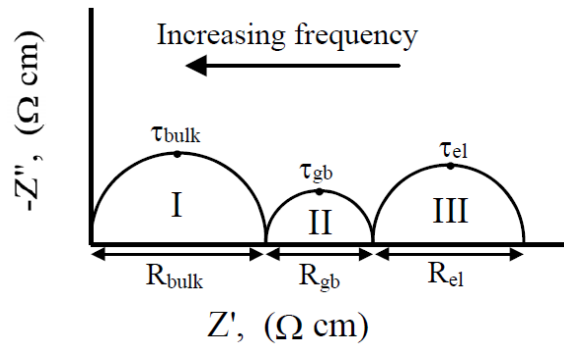


**Figure 2.1** Idealised Nyquist impedance plot showing the: I) grain, II) grain boundary, and III) electrode resistivities.  $R_{\text{bulk}}$ ,  $R_{\text{gb}}$  and  $R_{\text{el}}$  are the impedances for the grain, grain boundary and electrode contributions.  $\tau_{\text{bulk}}$ ,  $\tau_{\text{gb}}$ ,  $\tau_{\text{el}}$  are the relaxation times for the grain, grain boundary and electrode processes.

The representation of imaginary impedance ( $Z''$ ) versus the real part ( $Z'$ ) in a complex plane is called a Nyquist plot. The output of a simulated solid electrolyte cell is shown in **Figure 2.1**. In an electrically inhomogeneous sample, which contains several components (bulk, grain boundary, electrode *etc.*), each semicircle corresponds to the grain, grain boundary and electrode contributions respectively, which may be represented by a parallel  $RC$  element, where  $R$  is the resistance and  $C$  the capacitance. An equivalent circuit for such a sample is given in **Figure 2.2** and consists of individual  $RC$  sub-circuits denoting the various processes in a typical solid electrolyte cell. It is desired to separate each parallel  $RC$  element and measure its component  $R$  and  $C$  values. The magnitude of  $R$

will give the resistance of the specific process, and the magnitude of  $C$  will serve to identify the process. The famous software package Zview software has been employed to analyze IS data based on equivalent circuits [6].

**Figure 2.1** also demonstrates how the impedance and relaxation time information is deduced from the data. The relaxation time for each process is calculated from **Eq. (2-3)** using the apex frequency shown in **Figure 2.1**.  $\omega_o$  is the angular frequency and  $f_o$  is the relaxation frequency (Hz)

$$\tau_o = \omega_o^{-1} = RC = (2\pi f_o)^{-1} \quad (2-3)$$

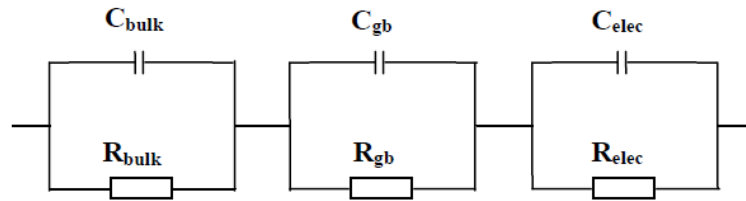


**Figure 2.2** Equivalent circuits for complex impedance spectroscopy measurements showing the bulk, grain boundary and electrode  $RC$  sub-circuits.

Frequently, the experimental data for many systems give complex plane diagrams that form circular arcs with center lying below the axis (that is a depressed semicircle). This is the so-called dispersing phenomenon. In the case of the dispersing effect, the double-layer capacitance and pseudo-capacitance involved in electrochemical reactions do not function as pure capacitors, but as constant phase elements (CPEs), whose admittance and impedance, respectively, are defined as:

$$Y_{CPE} = Y_o(j\omega)^a \quad (2-4)$$

$$\text{And } Z_{CPE} = \frac{1}{Y_o(j\omega)^a}$$

Where  $Y_o$  is the admittance magnitude and  $a$  the exponential term,  $a=1$  in a perfect capacitor and  $a=0$  for a pure resistor. Capacitors should be substituted by CPEs in the

equivalent circuits to result in a better fit when the dispersing impedance data are encountered.

### 2.3.2 Experimental method

Electrical measurements were performed on a commercial sample-holder (Systems-Ionics) coupled to a Solartron 1260 frequency response analyzer. Acquisitions were performed at fixed temperatures after a stabilization of more than 1 h. The two sides of the pellets were painted by platinum ink (METALOR n° 6926), dried at 373 K in an oven, and further heat-treated at 1373 K during 2 h. The measurements were either carried out in dry and wet atmosphere, or in controlled  $P(\text{O}_2)$  and  $P(\text{H}_2\text{O})$  atmospheres. Measurements in dry and wet atmospheres were performed on cooling starting from 850°C, with a cooling rate of 200°C/h for dry atmosphere and 50 °C/h for wet atmosphere. In the first case, drying was achieved by running the gas through a column of  $\text{P}_2\text{O}_5$  desiccant, and humidification was obtained by bubbling gas through water. The oxygen partial pressure was controlled by an electrochemical pump (Zirox electrolysis cell) coupled to a couple of Ar/air - delivering mass flow controllers. This system allows the control of oxygen partial pressure in a continuous way from  $10^{-6}$  atm to 1 atm. For low oxygen partial pressure ( $P(\text{O}_2) < 10^{-6}$  atm.), the oxygen partial pressure was deduced by chemical equilibrium calculation between  $\text{H}_2$ , Ar and water partial pressure at 1 atm. 5  $\text{H}_2/\text{Ar}$  and Ar gas were mixed by mass flow controllers, and water partial pressure was controlled by gas humidifier (OMI-SP280C-A, OMICRON Technologies). The impedance spectra were obtained in the frequency range of 0.1 Hz to 10 MHz, where the AC potential amplitude was 50 mV. ZView2 electrochemical impedance software of Scribner Associates Inc. was used for data analysis.

## 2.4 Synthesis of ceramics oxides

Materials examined in this work were synthesized by both solid state reaction (SSR) and a chemical solution route. Acceptor-doped samples were prepared by acrylic acid

polymerization, while the samples with ZnO additive were prepared by solid state reaction method.

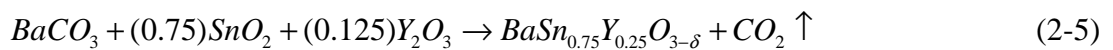
### 2.4.1 Solid state reaction

The conventional SSR is the most common used method for multi-component ceramic powders synthesis with the advantage of its simplicity. It involves intimate mechanical mixing of the ceramic precursors (oxides, carbonates and nitrates), repeated grinding and heating cycles to achieve pure crystalline results. However, this method has clear disadvantages in that the non-homogeneities of the initial powders necessitate multiple repetitions of prolonged thermal treatment and grinding. As a consequence, it produces large grains, and induces chemical and grain size non-uniformity.

In this work, we have combined the ball milling and SSR methods. The precursors are first milled using ball milling, to obtain homogenous fine powders, which also help decreasing the calcination temperature to obtain a single phase.

For example; the SSR route for  $BaSn_{0.75}Y_{0.25}O_{3-\delta}$  is as follows. Starting materials were high purity  $BaCO_3$  (Alfa Aesar, 99.9 -101 %),  $SnO_2$  (Alfa, 99.9 %),  $Y_2O_3$  (Rhône-Poulenc, 99.999 %). Firstly,  $BaCO_3$  powders were dried at 120 °C in the oven;  $SnO_2$  and  $Y_2O_3$  were fired at 800 °C for 2 h before mixing together. The mixtures were milled in a  $ZrO_2$  container with  $ZrO_2$  balls (Retsch, PM100) at 450 rpm for 12 h and subsequently calcined in air at 1400 °C for 10 h.

The nominal formation reaction is:



For the other compositions, the synthesis follows the same route, with different starting materials and temperature.

### 2.4.2 Acrylic acid polymerization

Syntheses using wet chemistry routes can overcome many of the disadvantages of SSR method. The homogeneity of the product is expected due to the mixing of the

reagents at the molecular level in solution. The resulting oxide powders have a high specific surface area and, consequently, a high reactivity, which decreases the final temperature and time of treatment. There are many different wet chemical routes existing to synthesise fine ceramic powders, such as co-precipitation, spray drying, freeze drying, Pechini method, and sol-gel, which were presented in **Chapter 1** for the particular case of BaSnO<sub>3</sub>. Unfortunately, these methods are time consuming if large quantities of fine powders are required. In this work, we utilized acrylic acid polymerisation method for fine powders synthesis. Cations are chelated strongly by citric acid in aqueous solution, and stable solutions of citrates are easily and rapidly gelled by in situ formation of auxiliary three-dimensional tangled network: the polyacrylic gel, in which the appropriate cations are chelated in nanocavities. After drying in microwave oven, pyrolysis then yields very fine and highly dispersed powders of mixed oxides and solid solution [7]. It has widely been used to prepare a broad range of electroceramic oxides [8-10].

#### 2.4.2.1 Experimental process

In this wet chemical method, nitrate compounds were preferred, which easily dissolve into water and favor combustion reactions. In this study, we successfully prepared citric acid stabilised tin nitrate solution (with Sn<sup>2+</sup> content of 0.2 mol•L<sup>-1</sup>). Tin metals were dissolved into diluted nitric acid ( $n_{\text{nitric acid}} = 4 n_{\text{tin metal}}$ ,  $C_{\text{nitric acid}} = 2 \text{ mol}\cdot\text{L}^{-1}$ ) and citric acid solution ( $n_{\text{citric acid}} = 2 n_{\text{tin}}$ ), citric acid serving as chelating reagent. Some precipitates were observed during dissolution, and the color of solution became gray. After all tin metal were dissolved, the pH value was then increased till a value of 6 by adding ammonia. Almost all precipitates disappeared. However, there were still some precipitates in the solution, so it needed to be filtered before using. **Figure 2.3** shows the transparent tin solution after filtering. To determine tin concentration, 10 ml of solution was measured 3 times, and then calcined at 1000°C for 4 h. The resulting mass of SnO<sub>2</sub> was then measured. The concentration of tin solution deduced.



**Figure 2.3** Tin solution

$\text{BaSn}_{1-x}\text{M}_x\text{O}_{3-\delta}$  (denoted  $x = 0-0.5$ ,  $M = \text{Fe}, \text{Sc}, \text{In}, \text{Y}\dots$ ) powders were synthesized by gel polymerisation route from an aqueous solution containing cation. Firstly,  $\text{Ba}(\text{NO}_3)_2$ , tin solution and  $\text{M}(\text{NO}_3)_3$  were completely dissolved into de-ionized water in different beakers. Then, the three solutions were mixed together resulting in a clear transparent solution with total volume equal to 250 mL. The pH value was then increased till a value of 6 by adding ammonia. The mixed solution was heated until boiling, then added 25 mL of acrylic acid followed by 1.4 g of N, N'-methylene bis-acrylamide. The solution was then heated until boiling again, and then we added several droplets of hydrogen peroxide as an ignition reagent. At this moment, the two monomers reacted together to form a cross-linked polymer containing the solution, immediately forming a transparent gel, as shown in **Figure 2.4 (a)**.

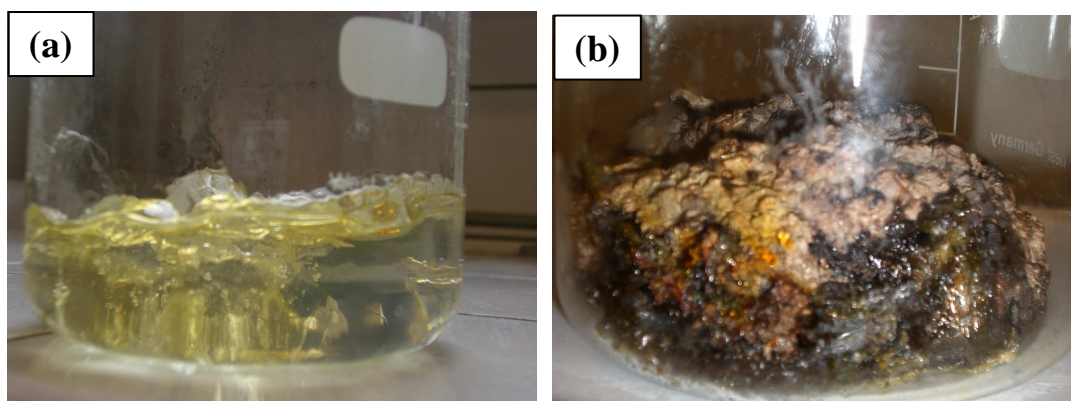


**Figure 2.4** (a) Gel, (b) Precursor after combustion

The gel obtained was then dried in a microwave oven for 30 min. The precursor obtained was heat-treated between 700 °C and 1200°C for 4 h leading to the desired  $\text{BaSn}_{1-x}\text{M}_x\text{O}_{3-\delta}$  compounds. The experimental process is presented in **Figure 2.5**.

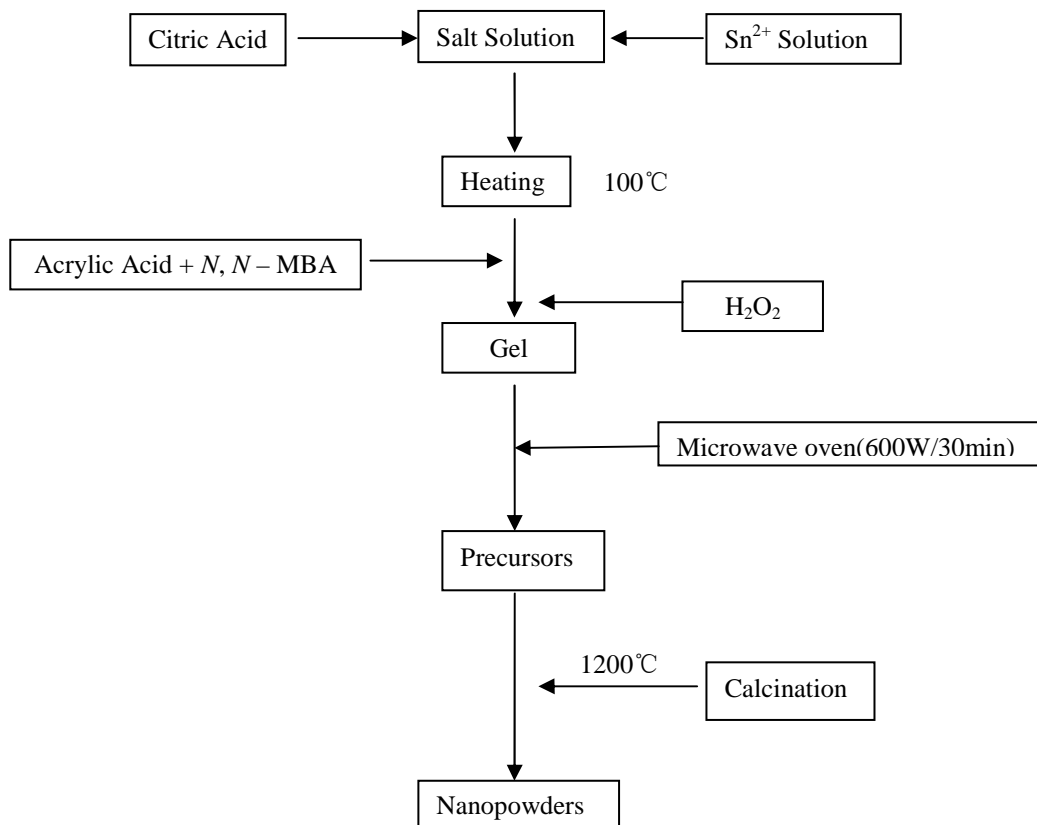


**Figure 2.5** The synthesis process of  $\text{BaSn}_{1-x}\text{M}_x\text{O}_{3-\delta}$  powders

#### 2.4.2.2 Physico-chemical characteristics of powders

$\text{BaSnO}_3$  based powders were synthesized using gel polymerisation, *i.e.* pure  $\text{BaSnO}_3$  (denoted BSO) and  $\text{BaSn}_{0.5}\text{Y}_{0.5}\text{O}_{3-\delta}$  (denoted BSY50). These two extreme compounds in terms of composition were used to optimise the pure powder preparation.

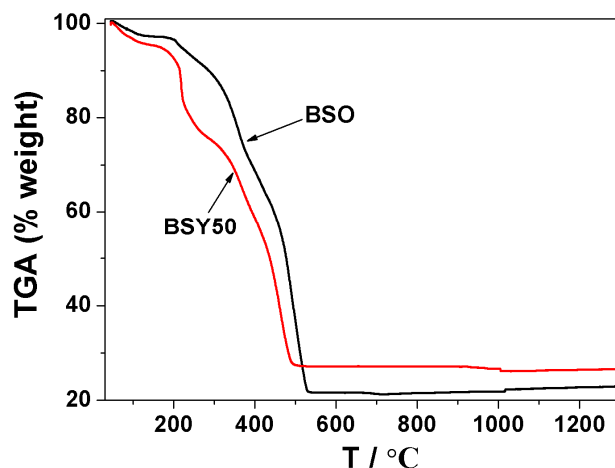


**Figure 2.6** TGA experiments applied to BSO and BSY50 precursors in air.

In the TGA curve, the weight loss is about 4 % for  $T < 150^{\circ}\text{C}$ , which is attributed to departure of residual water. Most of weight loss occurs below  $500^{\circ}\text{C}$ , it includes two steps: step I ( $T = 200\text{--}300^{\circ}\text{C}$ ) and step II ( $T = 300\text{--}520^{\circ}\text{C}$ ), and the weight loss is about 70 % due to the decomposition and oxidation of acrylic polymer and nitrate ions with the acrylamide polymerisation route [11]. It was also reported that two exothermic peaks appear at  $390^{\circ}\text{C}$  and  $460^{\circ}\text{C}$  under air atmosphere, which is in accord with our results [11]. Above  $520^{\circ}\text{C}$ , the weight loss is about 5 %, and may be due to the decomposition of residual carbonate. The weight loss of BSO is higher than that of BSY50 because the total citric acid content decreases with increasing Y content.

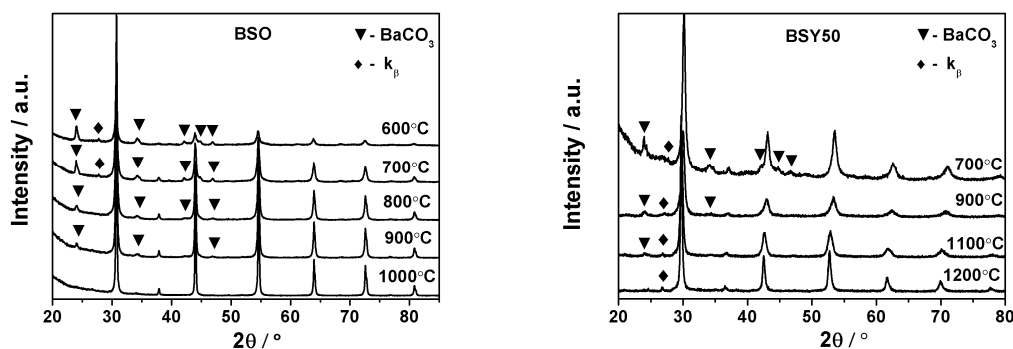


**Figure 2.7** XRD patterns of BSO and BSY50 powders calcined at different temperatures.

X-ray diffraction patterns of powders calcined at different temperatures are displayed in **Figure 2.7**. Analysis of XRD diffraction patterns shows the existence of the typical peaks of barium stannate after thermal treatment at 600°C for 4h, although the residual impurity BaCO<sub>3</sub> with the main diffraction peak at 23.9° [12] is detected until 900°C for BSO and till 1100°C for BSY50. The intensity of the main peak of BaCO<sub>3</sub> decreases with increasing calcination temperature, and is not further detected in the sample calcined at 1000°C for BSO, 1200°C for BSY50. Y dopant seems to make the formation of the perovskite phase more difficult and thus also the elimination of BaCO<sub>3</sub>. In **Figure 2.7**, diffraction peaks are thinner for undoped sample indicating a greater grain size for pure BaSnO<sub>3</sub>.

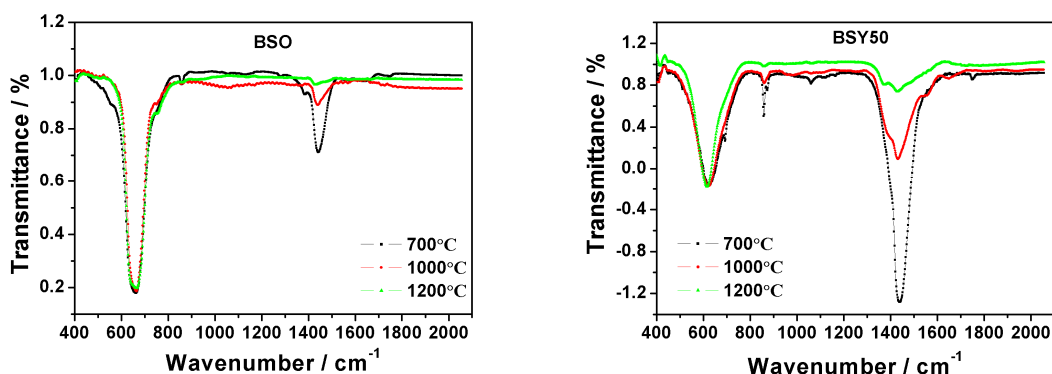


**Figure 2.8** Infrared spectroscopy of BSO and BSY50 compounds.

FTIR spectra for precursor calcined at different temperatures are presented in **Figure 2.8**. The band with absorption bands at 627 cm<sup>-1</sup> is the characteristic stretching mode of Sn-O bonds [13]. Two absorption bands at 1443 cm<sup>-1</sup> and 861 cm<sup>-1</sup> correspond to BaCO<sub>3</sub> [14-15], and the intensity decreases with increasing temperature. However, this band is also detected after thermal treatment at 1200°C in contradiction with X-ray diffraction measurements. Barium carbonate is difficult to remove completely in wet chemical method. It was reported that the decomposition temperature of pure barium carbonate is above 1300°C, and the single phase of BaSnO<sub>3</sub> powders was obtained at 1500°C [12]. Sin *et al.* [16] reported that the precursor first calcined at 600°C in oxygen,

and calcined at 1000°C and 1100°C in Ar, will remove effectively BaCO<sub>3</sub>. The persistence of carbonate peaks after high temperature thermal treatment could also be due to post-treatment surface carbonation of the samples.

#### 2.4.2.3 Microstructure of pure and doped BaSnO<sub>3</sub> powders

The surface morphology and microstructure of BSO and BSY50 powders were observed by SEM, as shown in **Figure 2.9** and **Figure 2.10**, respectively. The shape and agglomeration of BSO and BSY50 powder is very different. **Figure 2.9** shows that BSO powders exhibit an almost spherical morphology and porous agglomeration, and the agglomeration and grain size increase obviously with temperature. Below 1000°C, BSY50 powders consist in soft agglomerates of small size grains with some characteristic cubic shapes. Grain size, between 50 nm and 70 nm, alters slightly with thermal treatment at low temperature. However, above 1100°C, the distributions of grain size start to be very wide, and the grain size is from 100 nm to 200 nm.

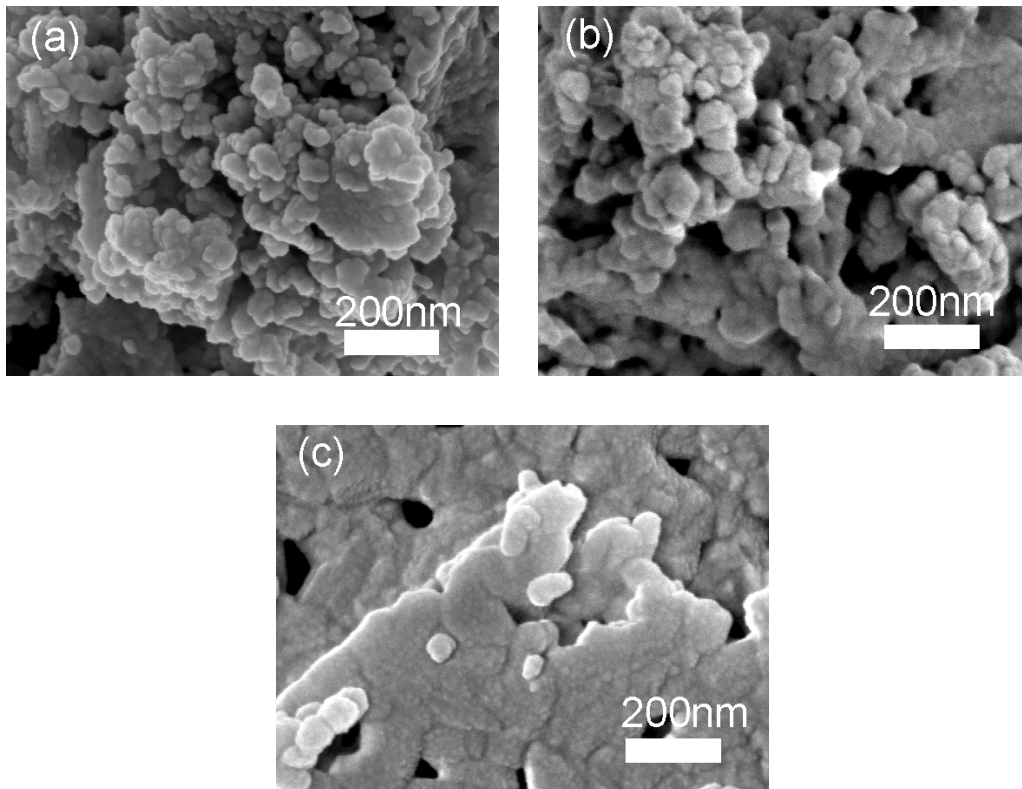


**Figure 2.9** SEM pictures of BaSnO<sub>3</sub> powders: (a) 800°C, (b) 1000°C, (c) 1200°C for 4 h.

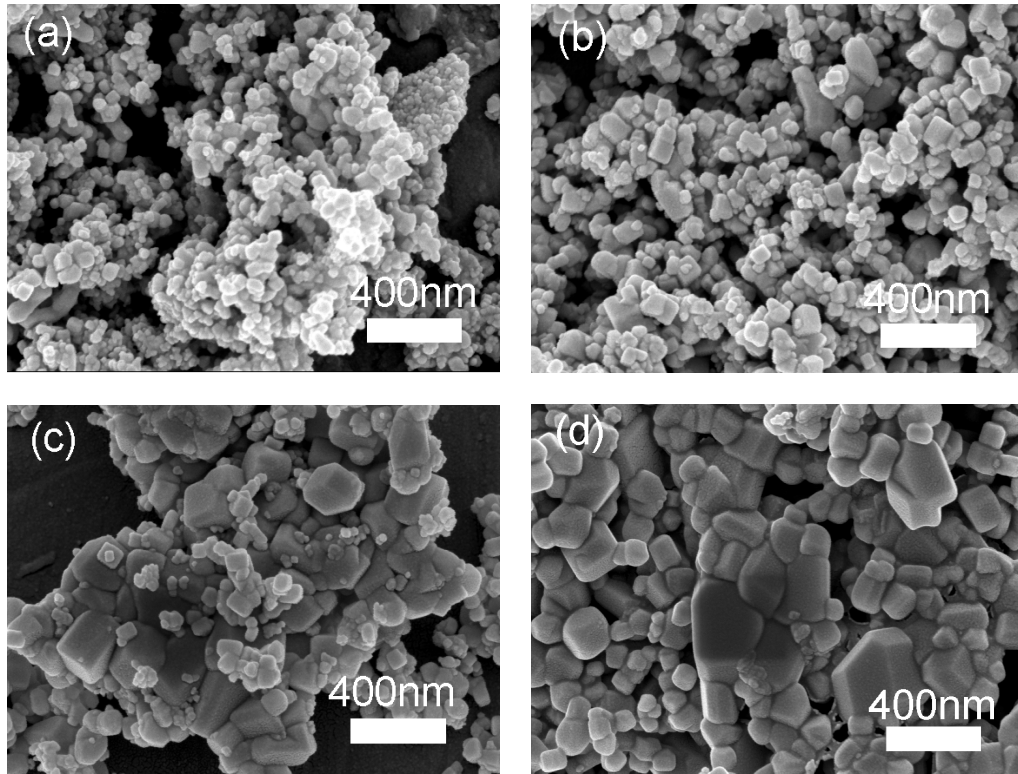


**Figure 2.10** SEM pictures of BSY50 powders: (a) 800 °C, (b) 1000 °C, (c) 1100 °C, (d) 1200 °C for 4 h.

### 2.4.3 Sintering

The powders calcined were dispersed using ball milling in a  $ZrO_2$  container with  $ZrO_2$  balls at 400 rpm for 2 h. Green pellets (9 mm in diameter, 60-70 % in relative density) were obtained by uniaxial pressing at 4 t pressures for 1 min, and isostatic pressing at 750 Mpa during 10 min. High density pellets were obtained by sintering in air at 1500°C and 1600°C during 12 h. The density, determined by simple measurement of pellet mass and dimensions after polishing the surfaces, was superior or equal to 90 %.

### 2.5 Conclusion

The experimental methods used in this study have been presented in detailed, in particular, for the powders preparation. Two extreme compounds in terms of composition, pure  $BaSnO_3$  and 50 mol % Y-doped  $BaSnO_3$  were used to optimize the pure powder preparation. XRD and FTIR show that barium carbonate is difficult to remove completely

using gel polymerization method even if calcined at 1200°C. Y dopant seems to make the formation of the perovskite phase more difficult and thus also the elimination of barium carbonate. A compromise between the preparation of pure phase (*i.e.* without barium carbonate) and the obtention of small grain size corresponds to a thermal treatment of 1200°C for 4 h. This treatment was the one used in the following to prepare nanopowders from the polymerization route. Let us precise here that whatever the composition, the pellets prepared from this nanopowders had always a density around 90 % after sintering at 1500°C for 12 h. This constitutes already a very good result considering the aversion toward densification of BaSnO<sub>3</sub> based compounds.

## References

- [1] Bruker AXS InC., *EVA 2*, **2001**.
- [2] Bruker AXS InC., *Topas V2.1*, **1999**.
- [3] J. Laugier, Celref V3, Laboratoire des Materiaux et du Génie Physique de l'Ecole Supérieure de Physique de Grenoble **1999**.
- [4] E. Barsoukov, J. R. Macdonald, *Impedance Spectroscopy Theory, Experiment, and Applications ( 2ed)*, John Wiley & Sons, Inc, Hoboken, New Jersey **2005**.
- [5] W. Lai, S. M. Haile, *Journal of the American Ceramic Society* **2005**, 88, 2979.
- [6] Scribner, Associates InC., *Zview V 2.9C*, **1990-2005**.
- [7] A. Douy, *International Journal of Inorganic Materials* **2001**, 3, 699.
- [8] P. O. Agusti Sin, *Adv. Mater.* **2000**, 12, 646.
- [9] A. Tarancon, G. Dezanneau, J. Arbiol, F. Peiro, J. R. Morante, *Journal of Power Sources* **2003**, 118, 256.
- [10] A. Calleja, X. Casas, I. G. Serradilla, M. Segarra, A. Sin, P. Odier, F. Espiell, *Physica C: Superconductivity* **2002**, 372-376, 1115.
- [11] A. Magraso, A. Calleja, X. G. Capdevila, F. Espiell, *Solid State Ionics* **2004**, 166, 359.
- [12] C. P. Udawatte, M. Kakihana, M. Yoshimura, *Solid State Ionics* **1998**, 108, 23.
- [13] H. S. Wensheng Lu, *J Sol-Gel Sci Techn* **2007**, 42.
- [14] W. Lu, H. Schmidt, *Ceramics International* **2008**, 34, 645.
- [15] P. Duran, D. Gutierrez, J. Tartaj, M. A. Bapares, C. Moure, *Journal of the European Ceramic Society* **2002**, 22, 797.
- [16] A. Sin, B. Montaser, P. Odier, F. Weiss, *Journal of the American Ceramic Society* **2002**, 85, 1928.

# Chapter 3 Synthesis, Structure and Electrical Properties of $\text{BaSn}_{1-x}\text{M}_x\text{O}_{3-\delta}$

## 3.1 Introduction

In this chapter, we want to explore the structural and transport properties of doped  $\text{BaSnO}_3$ . From the beginning, the number of possible dopants is chosen as wide as possible and we will then restrict our study to the most interesting ones. This chapter is interesting for the application since it helps to identify the dopants giving the most interesting properties but also from the fundamental point of view since it helps understanding the defect chemistry of acceptor-doped perovskite compounds.

For perovskite-type oxides, the site-incorporation mechanism of  $\text{M}^{3+}$  dopants controls the overall defect chemistry and thus their transport properties. The incorporation of  $\text{M}^{3+}$  dopants onto  $\text{B}^{4+}$ -site will generate oxygen vacancies, and introduce protons into crystal structure via the dissolution of hydroxyl ions at oxygen vacancy site in humidified atmosphere, but the incorporation of the  $\text{M}^{3+}$  dopant onto the  $\text{A}^{2+}$  site will reduce oxygen vacancies contents and thus proton conductivity. Some studies have shown that for  $\text{M}^{3+}$ -doped  $\text{A}^{2+}\text{B}^{4+}\text{O}_3$  perovskites the  $\text{M}^{3+}$  dopants distribute over the two cation sites, and that the effect, is greater for large dopant ions [1-3].

In this chapter, the defect chemistry, especially possible incorporation onto A-site of  $\text{M}^{3+}$ -doped  $\text{BaSn}_{1-x}\text{M}_x\text{O}_{3-\delta}$  ( $x = 0.125$  and  $0.25$ ,  $\text{M} = \text{Fe}, \text{Sc}, \text{In}, \text{Y}, \text{Gd}, \text{Sm}, \text{Nd}$  and  $\text{La}$ ) were investigated based on lattice parameter and empirical defect model. The  $\text{Sc}, \text{In}, \text{Y}$  and  $\text{Gd}$  dopants were explored more deeply by powder X-ray diffraction, thermogravimetry analysis, scanning electronic microscopy and impedance spectroscopy to investigate the effect of dopants nature on the microstructure and transport properties of doped barium stannate compounds.

### 3.2 Structural properties of $BaSn_{1-x}M_xO_{3-\delta}$ compounds

Doped  $BaSnO_3$  nanopowders were prepared by polymerisation as shown in Chapter 2. No major difference was observed during the process depending on dopant nature. In all cases, as shown in **chapter 2**, a compromise between small grain size and phase purity is obtained for a thermal treatment at  $1200^\circ\text{C}$  for 4 h. X-ray diffraction patterns of powders presented in **Figure 3.1**. Except the presence of residual  $BaCO_3$  impurity, there are no other impurities observed. However, for La and Nd dopants, we can not obtain the pure phase at  $1200^\circ\text{C}$ . As shown below, higher temperatures are needed in these cases.

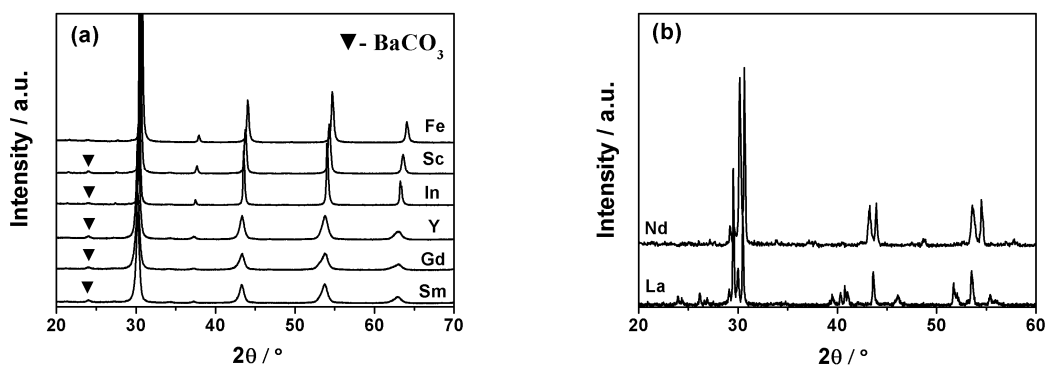


**Figure 3.1** X-ray diffraction of powders calcined at  $1200^\circ\text{C}$  for 4 h: (a)  $BaSn_{0.75}M_{0.25}O_{3-\delta}$  (Fe, Sc, In, Y, Sm and Gd), (b) Nd and La doped  $BaSnO_3$ .

$BaSn_{0.75}M_{0.25}O_{3-\delta}$  powders were pressed into pellets under pressure 750 MPa, and sintered at  $1500^\circ\text{C}$  and  $1600^\circ\text{C}$  for 12 h. The XRD patterns of the sintered  $BaSn_{0.75}M_{0.25}O_{3-\delta}$  are shown in **Figure 3.2**. Single phase perovskite is obtained for all different dopants, and the peak corresponding to the phase of  $BaCO_3$  impurity is not detected. Indexing of the powder X-ray diffraction patterns is realised considering the space groups  $Pm\bar{3}m$ . The measured densities and cell parameters of sample are summarized in **Table 3.1**.

From the cell parameters values and considering an occupation of sites equal to that supposed by the chemical formula, we can also calculate the theoretical density of these compounds (see **Table 3.1**).

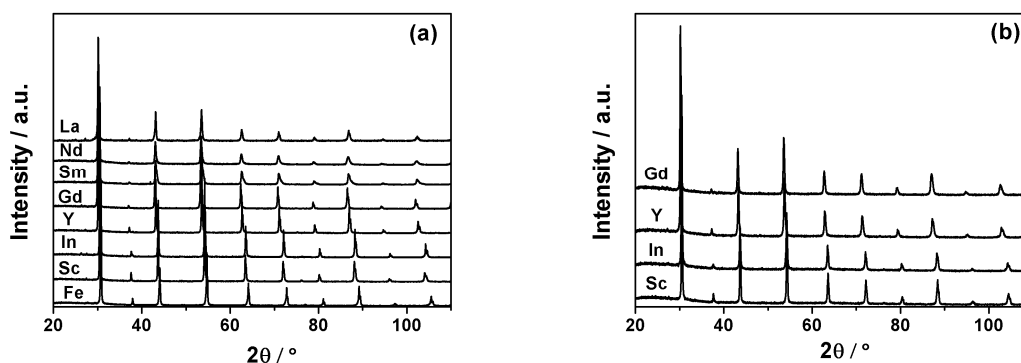


**Figure 3.2** X-ray diffraction patterns of  $BaSn_{0.75}M_{0.25}O_{3-\delta}$  samples: (a) 1500°C for 12 h, (b) 1600°C for 12 h.

Compounds	Cell parameter (Å)	Theoretical density (g/cm <sup>3</sup> )	Observed Density (g/cm <sup>3</sup> )	Relative Density (%)
BSFe25	4.1048(11)	6.87	6.68	97.2
BSSc25	4.1453(5)	6.61	5.78	87.5
BSIn25	4.1403(3)	7.04	6.94	98.5
BSY25	4.1895(3)	6.65	5.94	89.3
BSGd25	4.2060(5)	6.95	6.23	89.6
BSSm25	4.2018(11)	6.94	6.3	90.8
BSNd25	4.1997(7)	6.91	5.88	85.1
BSLa25	4.1981(8)	6.89	6.76	98.1

**Table 3.1** Cell parameters, theoretical and experimental densities of  $BaSn_{0.75}M_{0.25}O_{3-\delta}$  compounds sintered at 1500°C for 12h.

**Table 3.1** shows that the relative density of sintered compounds depends on dopants nature. We find that In, Fe and La are favourable to sample sintering while other dopants are not. Ito *et al.* [4] reported that the partial substitution of In or Ga for Y as second dopant improves the sinterability of  $BaZrO_3$ , which was explained by two factors: a dopant oxide with lower melting point and a ionic radius of dopant closer to Zr are favourable to sintering. However, in present study, the radius of La dopant is much higher

than that of Sn, and has a high melting point, but show positive effects on sintering. Thus, further study is needed to fully understand the effect of oxide doping on densification.

### 3.3 Defect Chemistry of doped $BaSnO_3$

The defect chemistry, in particular, the dopant site incorporation selectivity in the perovskite  $BaSn_{0.75}M_{0.25}O_{3-\delta}$  ( $M = Fe, Sc, In, Y, Gd, Sm, Nd$  and  $La$ ) compounds is investigated here using a defect model based on cell parameters proposed by Wu *et al.* [3].

#### 3.3.1 Evolution of cell parameters

The lattice parameters determined by Topas and Cellref v3 programs are given in **Table 3.1**. The lattice parameters of samples sintered at  $1600^\circ\text{C}$  are lower than that of samples sintered at  $1500^\circ\text{C}$ , which might be attributed in part to the evaporation of barium. The lattice parameter evolution as a function of dopant radii (for  $x = 0.25$ ) is presented in **Figure 3.3**. From a simple consideration of ionic radii, the La doped sample would be expected to have the greatest lattice parameter and Fe-doped the smallest, with the Nd, Sm, Gd, Y, In and Sc-doped samples showing a decreasing trend of lattice parameter, respectively. However, it is evident that there is an abnormal lattice parameter drop for Sm, Nd and La, which leaves the Gd-doped sample a larger lattice parameter than that of Sm, Nd and La-doped compounds. Besides, the lattice parameter of In-doped sample is lower than that of Sc-doped sample. This latter fact can be easily explained by considering the possible evaporation of indium at high temperature.

The unexpected lattice parameters of Sm, Nd and La-doped samples are proposed to be a result of dopant incorporation onto the  $Ba^{2+}$ -site as reported for  $Ba_xCe_{0.85}M_{0.15}O_{3-\delta}$  ( $x = 0.85-1.20$ ,  $M = Nd, Gd, Yb$ ) [3]. If we assume that the trivalent dopant ion is incorporated only onto the Sn site,  $BaSn_{0.75}M_{0.25}O_{3-\delta}$ , the lattice parameter should be a monotonic function of dopant ionic radius [5]. Thus the evolution of the lattice parameters for large ions dopants, such as Sm, Nd and La, suggests that these large ions are at least partly incorporated onto Ba site due to BaO evaporation at high sintering temperature.

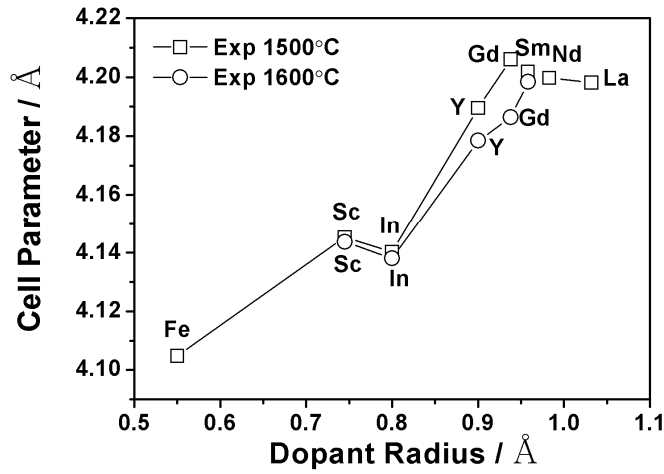


**Figure 3.3** Evolution of cell parameters as a function of dopant radius of  $BaSn_{0.75}M_{0.25}O_{3-\delta}$  compounds.

### 3.3.2 Defect model versus cell parameters

Wu *et al.* [3] quantified the relationship between stoichiometry and lattice parameters, and used this relationship to indirectly determine the concentration of M cations on the A and B sites from experimental values of the lattice parameters. The approach is based on the fact that there is an almost ideally linear relationship between the volume per formula unit of known ( $Ba^{2+}M^{4+}O_3$ ) perovskites and the sum of the volumes of the species comprising the formula unit, although the lattice parameters of a perovskite compounds can not be determined a priori from the ionic radii of the species involved because of the octahedral tilting that is well known to occur in this structure type. The relationship between the volume per formula unit of perovskites and the sum of the volumes of the species proposed by Wu *et al.* methods [3], is presented in **Table 3.2** and **Figure 3.4**.

The correlation was attained by fitting data in the **Figure 3.4**, as follows:

$$V_{cell} = -490.55 + 10.52V_{sum} \text{ \AA}^3 \quad (3-1)$$

	$VolB^{4+}$ ( $\text{\AA}^3$ )	t factor	$Vol(A+B+3O)$ ( $\text{\AA}^3$ )	$V_{ICSD}/unit$ ( $\text{\AA}^3$ )	REF(ICSD#)
$BaTiO_3$	0.9276	1.0615	52.891	64.4	73646
$BaSnO_3$	1.376	1.0184	53.339	69.731	15087
$BaZrO_3$	1.563	1.004	53.526	74.019	43136
$BaTbO_3$	1.839	0.9854	53.802	78.243	89028
$BaAmO_3$	2.572	0.946	54.535	82.313	61317
$BaPuO_3$	2.664	0.9418	54.627	84.192	65033
$BaPrO_3$	2.572	0.946	54.535	83.75	2753
$BaCeO_3$	2.758	0.9376	54.721	85.55	79625
$BaUO_3$	2.953	0.9294	54.916	86.04	84821

**Table 3.2** Calculated and experimental unit cell volume of  $Ba^{2+}M^{4+}O_{3-x}$  perovskite.

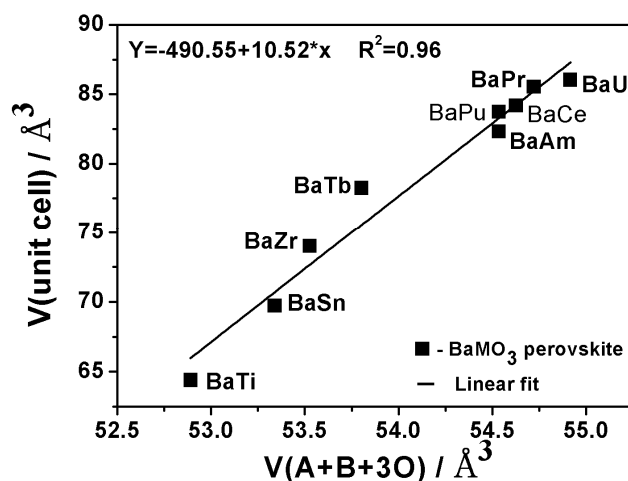


**Figure 3.4** Pseudo-cubic cell volume of barium based perovskites as a function of the sum of the ionic radii of the constituent species.

### 3.3.3 Application to doped $BaSnO_3$

**Figure 3.4** shows that this straight line correlation does not pass exactly through the data point for  $BaSnO_3$ . The experimental cell volume (per formula unit) is  $69.731 \text{ \AA}^3$ , whereas it was calculated at  $70.587 \text{ \AA}^3$  from **Eq. (3-1)**. Accordingly, the relationship is modified by a correction factor according to:

$$V_{cell} = -491.41 + 10.52V_{sum}^o \text{ \AA}^3 \quad (3-2)$$

From this, we can ideally use the measured cell volumes to determine the total volume of the species residing on the three sites of the perovskite cell with the relationship **Eq. (3-2)**. However, in order to apply this correlation to doped barium stannates, and to determine the values of three unknowns, A-site respective cation occupancy, B-site respective cation occupancy, and anion site occupancy, from a single input parameter, we need to take the following assumptions or approximations [3]: (1) both A and B sites are fully occupied (no cation vacancies), (2) M atom occupancy on the barium site will be sufficiently small so as to retain the validity of the correlation curve ( derived only for barium based perovskites) to the new composition and (3) anion vacancies, which are induced by doping, have the same volume as ions that would normally occupy those sites. This is considered reasonable in light of the radius assigned to an oxygen vacancy in perovskite structure ( $r(v_o^-) = 1.14045 \text{ \AA}^3$ ) by Mogensen *et al.* [6].

These approximations imply that the occupation on the A and B sites can be respectively described as [3]:

$$A = \left( \frac{1-2y}{1-y} \right) Ba + \left( \frac{y}{1-y} \right) M \quad (3-3)$$

$$B = \left( \frac{1-x}{1-y} \right) Sn + \left( \frac{x-y}{1-y} \right) M \quad (3-4)$$

Where  $2y/(1-y)$  represents the fraction of Ba lost from the perovskite composition, and  $y/(1-y)$  represents the dopant occupancy on the A-site. The parameter y is the amount of dopant on the A-site before normalization for the adjusted stoichiometry of the perovskite.

The volumes associated with these species were estimated using **Eq. (3-2)**, taking care to employ the ionic radii appropriate for the 12-fold and 6-fold coordination for Ba and Sn sites, respectively. This analysis is applied to the nominally stoichiometric samples sintered at 1500°C and 1600°C. The results, presented in **Table 3.3**, provide a measure of

the extent to which the dopant may incorporate on the A site in nominally stoichiometric compositions. The small cell volume of the Sm, Nd and La can now be explained, and support partial occupation of the A-site by Nd at about 2 % and La 3.1 % level. Of course, the model also foresees partial occupation of A-site for the smaller dopants. In this case, the values are of the order of 1 % dopant A-site. This probably indicate the limitations of such model since the evolution of cell parameters is reasonable for small dopants without considering a possible transfer of dopant atoms on A-site. Besides, let us precise that the assumption of full occupancy on A-site for these calculations is not fully reasonable since perovskite structure is known to accommodate easily vacancies on A-site (for instance due to more important Ba evaporation). The Ba evaporation also leading to a diminishing of cell parameters, the real situation may correspond to an intermediate case with both a partial occupation of dopant atoms on A-site and a non full occupancy of A-site.

Dopant	Sc	In	Y	Gd	Sm	Nd	La
V(exp) 1500°C	71.2308	70.9734	73.5337	74.4060	74.1833	74.0721	73.9875
M on A-site	0.0017	0.0096	0.0087	0.0099	0.0148	0.0202	0.0306
M on B-site	0.2483	0.2404	0.2413	0.2401	0.2352	0.2298	0.2194
V(exp) 1600°C	70.6653	70.8603	72.9508	73.3654	74.0034	-	-
M on A-site	0.005	0.0103	0.0122	0.0161	0.0159	-	-
M on B-site	0.245	0.2397	0.2378	0.2339	0.2341	-	-

**Table 3.3** The occupation of  $M^{3+}$  ions on A- and B-sites of nominally stoichiometric  $BaSn_{0.75}M_{0.25}O_{3-\delta}$  derived from cell volume analysis.

### 3.4 Thermal expansion

X-ray diffraction experiments were performed under vacuum atmosphere from 295K to 1073 K. 25 mol % Y-doped  $BaSnO_3$  as an example is presented in **Figure 3.5**. It shows that even at high temperature doped  $BaSnO_3$  compounds do not present any transition of structure. The indexations of the peaks are always done considering a cubic perovskite structure with space group:  $Pm\bar{3}m$ . The evolution of the lattice parameter with

temperature is shown in **Figure 3.6**, and the measured thermal expansion coefficients are listed in **Table 3.4**. The results show there is no evidence for thermal expansion coefficient evolution with dopant radius. The dopant (excepted Fe) presence increases slightly the thermal expansion coefficients comparing with pure  $BaSnO_3$  ( $9.6 \times 10^{-6} K^{-1}$  from 300 K to 800 K [7]). In the Fe case, the possible evolution of ion valence with temperature might explain the high value observed.

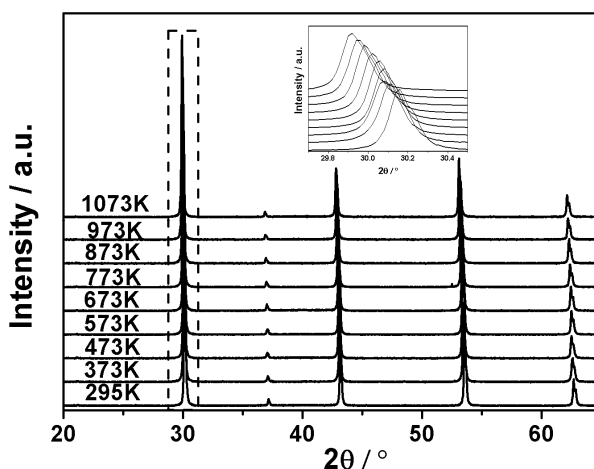


**Figure 3.5** X-ray diffraction of  $BaSn_{0.75}Y_{0.25}O_{3-\delta}$  at different temperatures

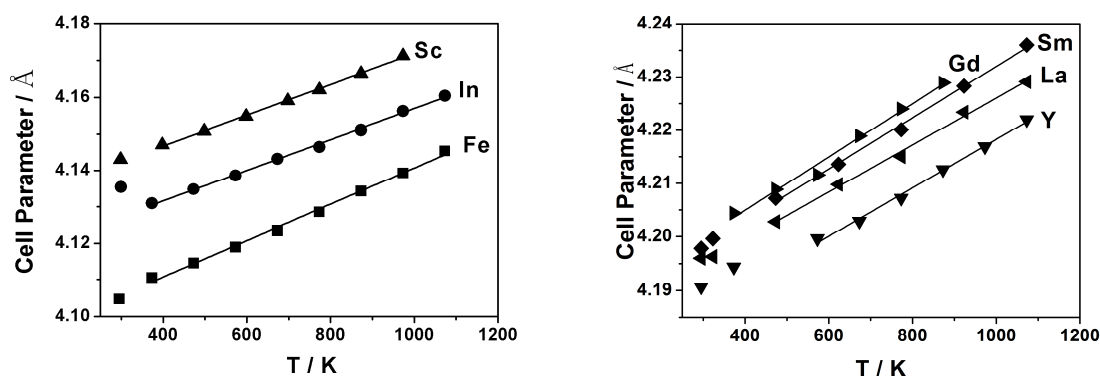


**Figure 3.6** Cell Parameter of  $BaSn_{0.75}M_{0.25}O_{3-\delta}$  ( $M = Fe, Sc, In, Y, Gd, Sm, Nd$  and  $La$ ) at different temperatures.

Dopant ion	Thermal Expansion	Range of temperature
	$\text{K}^{-1}$	K
$\text{Fe}^{3+}$	$1.22 \times 10^{-5}$	373-1073
$\text{Sc}^{3+}$	$1.02 \times 10^{-5}$	373-1073
$\text{In}^{3+}$	$1.01 \times 10^{-5}$	373-1073
$\text{Y}^{3+}$	$1.02 \times 10^{-5}$	573-1073 (*)
$\text{Gd}^{3+}$	$1.19 \times 10^{-5}$	373-873
$\text{Sm}^{3+}$	$1.15 \times 10^{-5}$	373-1073
$\text{La}^{3+}$	$1.05 \times 10^{-5}$	373-1073

(\*) in the case of yttrium, the linear thermal expansion was only observed between 573 and 1073K, probably due to residual water presence in the sample at RT.

**Table 3.4** Thermal Expansion of  $\text{BaSn}_{0.75}\text{M}_{0.25}\text{O}_{3-\delta}$  sintered at 1500°C

### 3.5 Thermodynamics and transport properties of $\text{BaSn}_{1-x}\text{M}_x\text{O}_{3-\delta}$

We now present the thermodynamics and transport properties of  $\text{BaSn}_{1-x}\text{M}_x\text{O}_{3-\delta}$  ( $x = 0.125$  and  $0.25$ ) compounds. The study is limited to those dopants having a radius close to that of tin *i.e.*  $\text{M} = \text{Sc}^{3+}$ ,  $\text{In}^{3+}$ ,  $\text{Y}^{3+}$  and  $\text{Gd}^{3+}$ . Due to the possible partial occupancy of dopant on A-site, Nd and La were not considered further.

#### 3.5.1 Microstructural and structural properties of samples

The XRD patterns for  $x = 0.125$ , are very similar to that presented above for  $x = 0.25$ . Indeed, XRD patterns of  $\text{BaSn}_{0.875}\text{M}_{0.125}\text{O}_{3-\delta}$  ( $\text{M} = \text{Sc}$ ,  $\text{In}$ ,  $\text{Y}$  and  $\text{Gd}$ ) compounds in **Figure 3.7** also show some small peaks corresponding to  $\text{BaCO}_3$  for powders, while the pellets patterns can be indexed in a pure cubic perovskite structure (space group:  $Pm\bar{3}m$ ). The cell parameters are observed to increase with dopant radius as analyzed for  $x = 0.25$ .

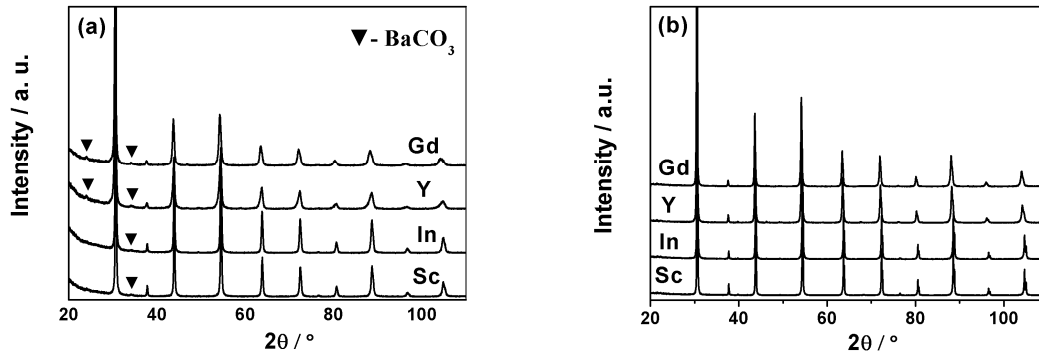


**Figure 3.7** X-ray diffraction of  $\text{BaSn}_{0.875}\text{M}_{0.125}\text{O}_{3-\delta}$  ( $\text{M} = \text{Sc}, \text{In}, \text{Y}$  and  $\text{Gd}$ ): (a) powders calcined at  $1200^\circ\text{C}$  for 4h, (b) pellets sintered at  $1600^\circ\text{C}$  for 12h.

The morphology of sintered pellets is shown in **Figure 3.8** and **Figure 3.9** for  $x = 0.125$  and  $x = 0.25$  respectively. All compounds exhibit dense structure. The grain size of Sc-, Y- and Gd-doped  $\text{BaSnO}_3$  compounds changes slightly with dopants nature and is about  $1\mu\text{m}$ , while the grain size ( $\sim 2\mu\text{m}$ ) of In-doped  $\text{BaSnO}_3$  is greater. The grain size increases significantly with dopant contents, especially for indium dopant, the grain size for  $x = 0.25$  is about  $8\mu\text{m}$ , much higher than that of  $x = 0.125$  ( $\sim 2\mu\text{m}$ ). This may indicate that the presence of oxygen vacancies may help for densification.

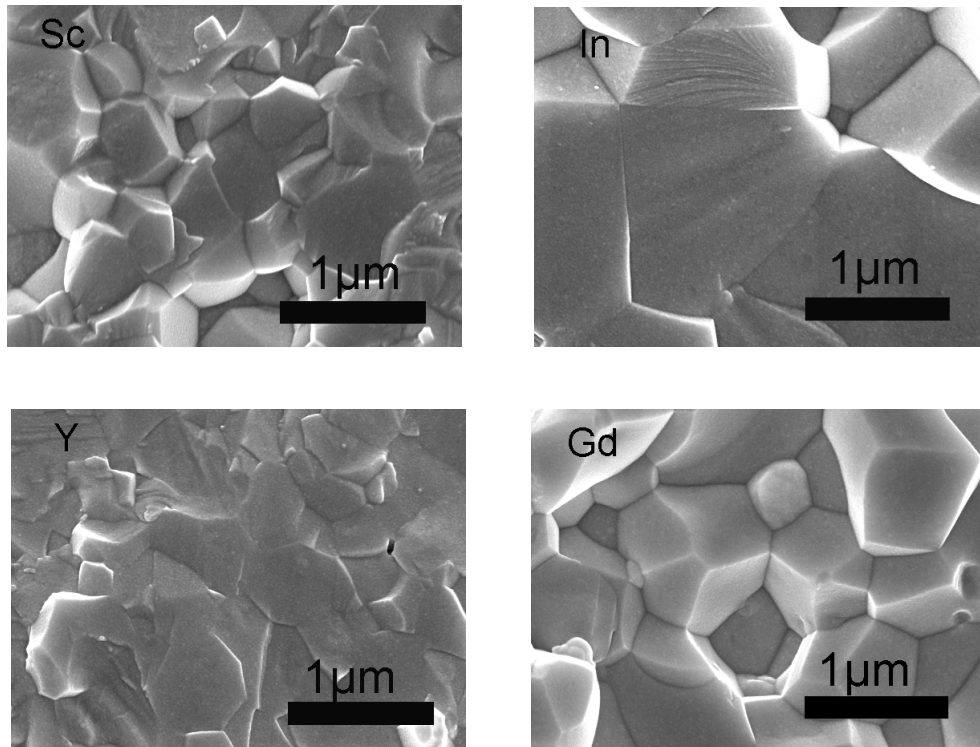


**Figure 3.8** SEM pictures of  $BaSn_{0.875}M_{0.125}O_{3-\delta}$  (M= Sc, In, Y and Gd) compounds sintered at 1600°C for 12 h.

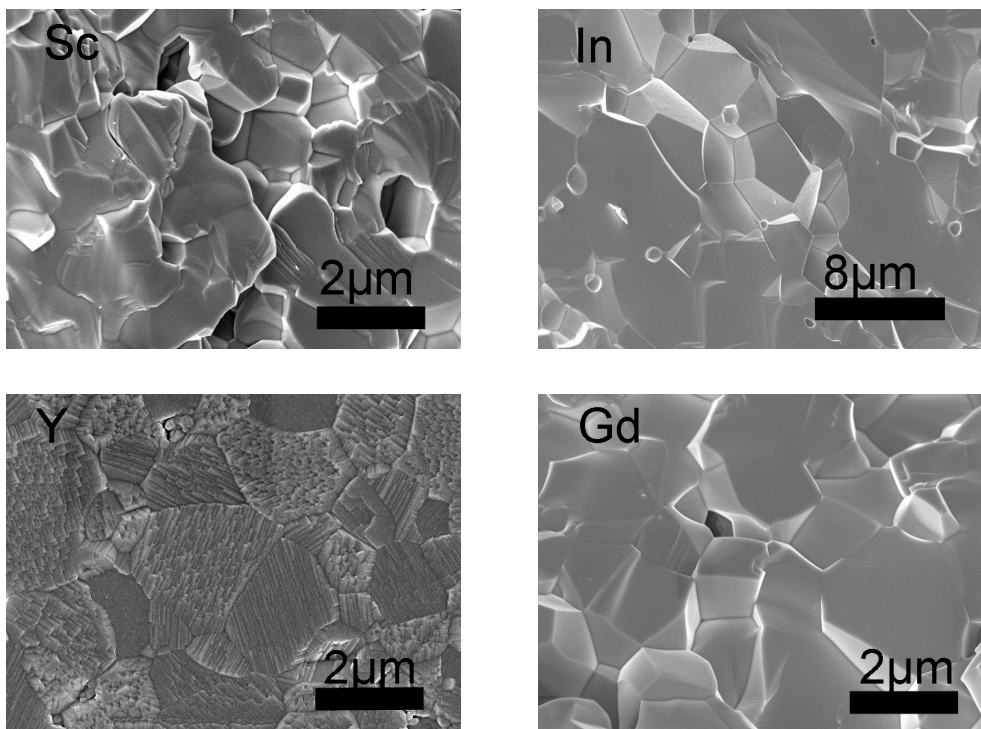


**Figure 3.9** SEM pictures of  $BaSn_{0.75}M_{0.25}O_{3-\delta}$  (M= Sc, In, Y and Gd) compounds sintered at 1600°C for 12 h.

### 3.5.2 Water uptake

Thermogravimetric analysis was performed using a SETARAM TG/DSC (Model 92-1750). The as-prepared powders were first heat-treated at 1200°C for 2 h under dry Ar to remove water from the structure and also possible surface carbon dioxide. The gas was then saturated with water ( $P(\text{H}_2\text{O}) = 0.021 \text{ atm.}$ ). Data were collected every 100°C between 800°C and 600°C, and 50°C between 600°C and 150°C upon cooling, with different time at each temperature in order to reach hydration equilibrium. The experimental results of weight increase due to water uptake are presented in **Figure 3.10**.

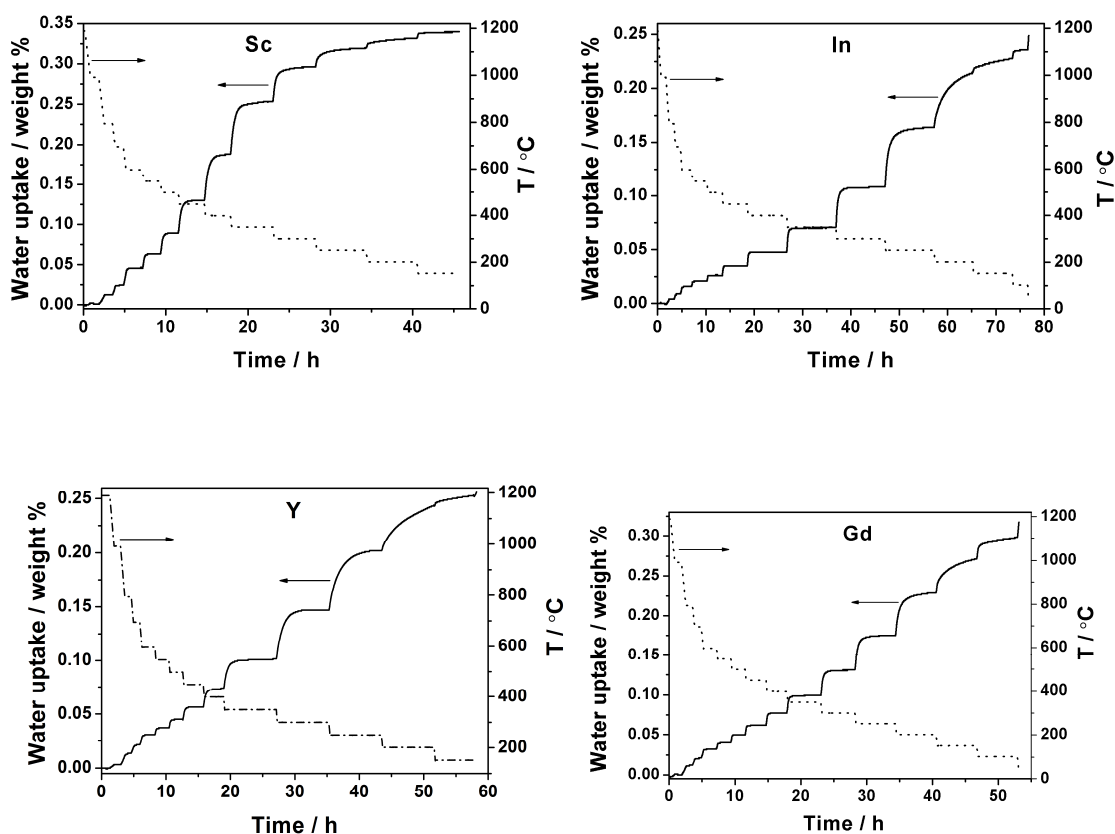


**Figure 3.10** Water uptake of  $\text{BaSn}_{0.875}\text{M}_{0.125}\text{O}_{3-\delta}$  ( $\text{M} = \text{Sc}, \text{In}, \text{Y}$  and  $\text{Gd}$ ) compounds as a function of time under  $P(\text{H}_2\text{O}) = 0.021 \text{ atm.}$

**Figure 3.10** shows that the weight changes significantly between 500°C and 200°C. For  $\text{In}^{3+}$ ,  $\text{Y}^{3+}$  and  $\text{Gd}^{3+}$ , the increase in weight spreads over a wide range of temperatures while for  $\text{Sc}^{3+}$  increase weight at low temperature is very limited. At high temperature ( $>$

550°C), the hydration reaction reaches equilibrium very quickly (1 h), while at low temperature (500-200°C), a long time is needed to reach equilibrium (3-8 h), depending on also on dopant nature. This long time to reach equilibrium is problematic from a practical point of view since experiments can last till more than 3 days.

From the final weight gain at a given temperature, one can deduce the  $OH'$  content for the same temperature. This is currently what has been done in **Figure 3.11 (a)** for the  $x = 0.125$  composition in  $BaSn_{1-x}M_xO_{3-d}$ . In order to extract the thermodynamical parameters characterising hydration, one has to use **Eq. (3-5)** that expresses the  $OH'$  content as a function of temperature, equilibrium constant  $K$ , and acceptor concentration. Nevertheless, as demonstrated by **Figure 3.11**, the  $OH'$  content does not reach the maximum value supposed by acceptor content ( $x = 0.125$ ). In this case, the equation is modified in order to take into account effective dopant content [8], as following:

$$[OH'_o] = \frac{3Kp_{H_2O} - \sqrt{Kp_{H_2O} (9Kp_{H_2O} - 6Kp_{H_2O}S + Kp_{H_2O}S^2 + Kp_{H_2O} + 24S - 4S^2)}}{Kp_{H_2O} - 4} \quad (3-5)$$

Where,  $S$  is the effective dopant content.

During a first approach, we fitted the  $OH'$  content values over the whole temperature range with the **Eq. (3-5)** and considering that the equilibrium constant follows an Arrhenius law with:

$$kT \ln K = T\Delta S^0 - \Delta H^0 \quad (3-6)$$

We obtained the hydration enthalpy, the hydration entropy and the effective dopant concentration. From these values, we expressed the hydration equilibrium constant as a function of the inverse of temperature. These are the curves plotted in **Figure 3.11 (b)**. This figure shows that the equilibrium constant as a function of inverse temperature is not linear in the whole range of temperatures. At intermediate/low temperature (below 600°C), the weight changes are essentially due to hydration and  $\ln K$  is almost linear in the Arrhenius representation. At high temperature, however, the behavior deviates from

linearity, displaying an increase in slope. Recently, Yamzzaki *et al.* [9] also reported a similar behavior in Y-doped  $BaZrO_3$  compounds. This deviation was thought to result from temperature dependences of the entropies and enthalpies of water incorporation, and from the influence of non negligible hole concentration and changes in oxygen content at high temperature. This last point is in agreement with what observed from transport properties (see **chapter 4**). Below  $250^\circ\text{C}$ , the values also deviate from linearity. This deviation may be due to the fact that hydration reaction was not in an equilibrium state due to slow kinetics. For this reason, the equilibrium constant was fitted in the  $600$  to  $200^\circ\text{C}$  temperature range using the equation mentioned above. In this case, only the enthalpy and entropy values were fitted since effective dopant concentration was retained from the previous fit. The results are reported in **Table 3.5** as a complement to the results obtained from the isobar fitting in the whole temperature range.

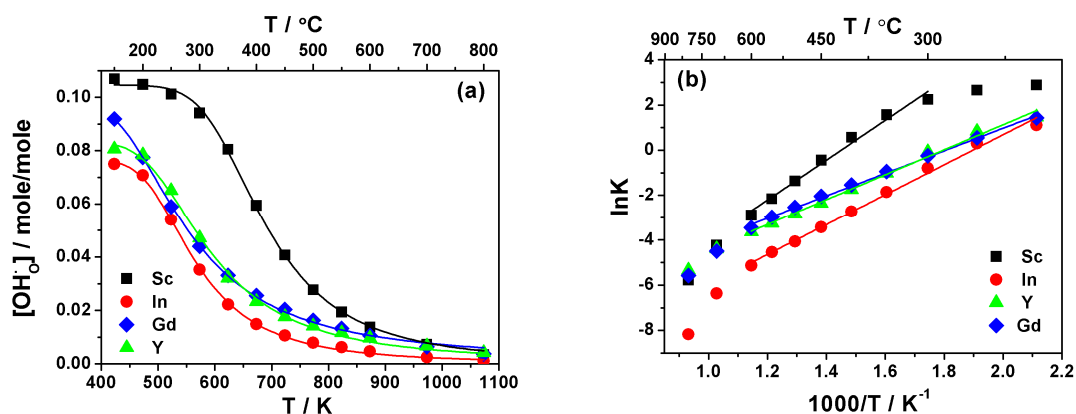


**Figure 3.11** Hydration behaviour of 12.5 mol % with different kinds of dopants: (a) Hydration isobars, (b) Equilibrium constant of the hydration reaction.

In this study, we have thus chosen to fit both hydration isobars and equilibrium constant (**Figure 3.11**) to obtain effective proton concentration, enthalpy and entropy of hydration, and listed in **Table 3.5**. Kreuer *et al.* [10] reported that the direct fitting of the hydration isobars leads to inaccurate enthalpy and entropy values since deviations from ideal behaviour or thermodynamic equilibrium may show up as a deviation from straight

line behaviour in the Arrhenius representation. **Table 3.5** shows that the values of enthalpy and entropy obtained using the direct fitting hydration isobars are more negative than that of a fitting of hydration equilibrium constant due to an increase in slope at higher temperature.

Dopant	$[M'_{Sn}]_{effective}$	$\Delta H_{hydr}^{\circ} / \Delta H_{hydr}^{\circ *}$ $kJmol^{-1}$	$\Delta S_{hydr}^{\circ} / \Delta S_{hydr}^{\circ *}$ $Jmol^{-1}K^{-1}$	$\Delta H_{hydr}^{\circ}$ (DFT)[12] $kJmol^{-1}$
Sc125	0.1046	-86.36/-73.44	-120.93/-106.43	
Sc25	0.176	-77.19/-67.46	-109.94/-100.94	-
In125	0.0769	-69.46/-58.9	-121.04/-109.83	-68.52
In25	0.22	-72.74/-64.13	-128.22/-115.06	-
Y125	0.0836	-59.01/-49.01	-97.17/-86.81	-66.59 ~ -67.55
Y25	0.1046	-69.15/-72.53	-120.38/-123.28	-
Gd125	0.0996	-46.11/-41.54	-79.33/-75.02	-1.93
Gd25	0.18	-46.87/-45.11	-83.01/-84.0	-

Note: Effective dopant concentration was attained by fitting the proton concentration.

(\*): Enthalpy and entropy were obtained by fitting  $\ln K$  versus  $1/T$  between 600°C and 200°C.

**Table 3.5** The hydration thermodynamics parameters for different dopants as determined from thermogravimetry and DFT calculations.

Dopant	$\Delta H_{hydr}^{\circ}$ $kJmol^{-1}$	$\Delta S_{hydr}^{\circ}$ $Jmol^{-1}K^{-1}$
Sc	-119.4	-124.9
In	-66.6	-90.2
Y	-79.5	-88.9
Gd	-66.1	-85.9

Note: The fitting temperature range is between 900°C and 500°C [10].

**Table 3.6** The hydration thermodynamics parameters of 10 mol % dopant level in  $BaZrO_3$

In the **Table 3.5**, both hydration enthalpy and entropy show some trends with the ionic radius of the dopant. In the case of  $BaZrO_3$ , a similar trend is not obvious, see **Table 3.6 [10]**, the values of hydration enthalpies of doped  $BaZrO_3$  are much more negative than that of  $BaSnO_3$ . It may be due to the different basicity and radius of Sn and Zr cations. Kreuer *et al.* [10] proposed that protonic defects seem to be increasingly stabilized with increasing basicity. The most negative enthalpy is observed for Sc dopant since oxygen ions coordinated to Sc show a significantly higher electron density and therefore higher basicity [8, 10, 11]. The thermodynamic data of the hydration reaction is almost independent of the dopant concentration. Only for Y dopant, the apparently more negative hydration enthalpy of 25 mol % Y content compares with 12.5 mol %, which may be a result of local structural distortions as a response to the formation of a high concentration of oxide ion vacancies [10].

Considering the evolution of  $OH'$  content as a function of temperature and taking into account the probable higher mobility of protons (compared to oxygen), one may anticipate that the proton conduction will overpass anion conduction at around 500-600°C.

### 3.5.3 Transport Properties

#### 3.5.3.1 Impedance spectra

Nyquist plots ( $Z_{imag}$  versus  $Z_{real}$  as parametric function of frequency) for the BSSc125 compound at different temperatures under wet and dry argon atmospheres are shown in **Figure 3.12**. It is evident that, under wet atmosphere, the impedance of samples diminishes strongly as compared to dry atmosphere. At low temperature (below 500°C), the impedance spectra consisted of two semicircles. The low frequency arc is attributed to grain-boundary processes whereas the high frequency arc is attributed to the bulk response, and contributions of both bulk and grain boundaries can be most often well identified and separated from the least squares fitting of the impedance data, by using for each contribution an equivalent electrical element consisting of a resistance in parallel with a constant phase element.

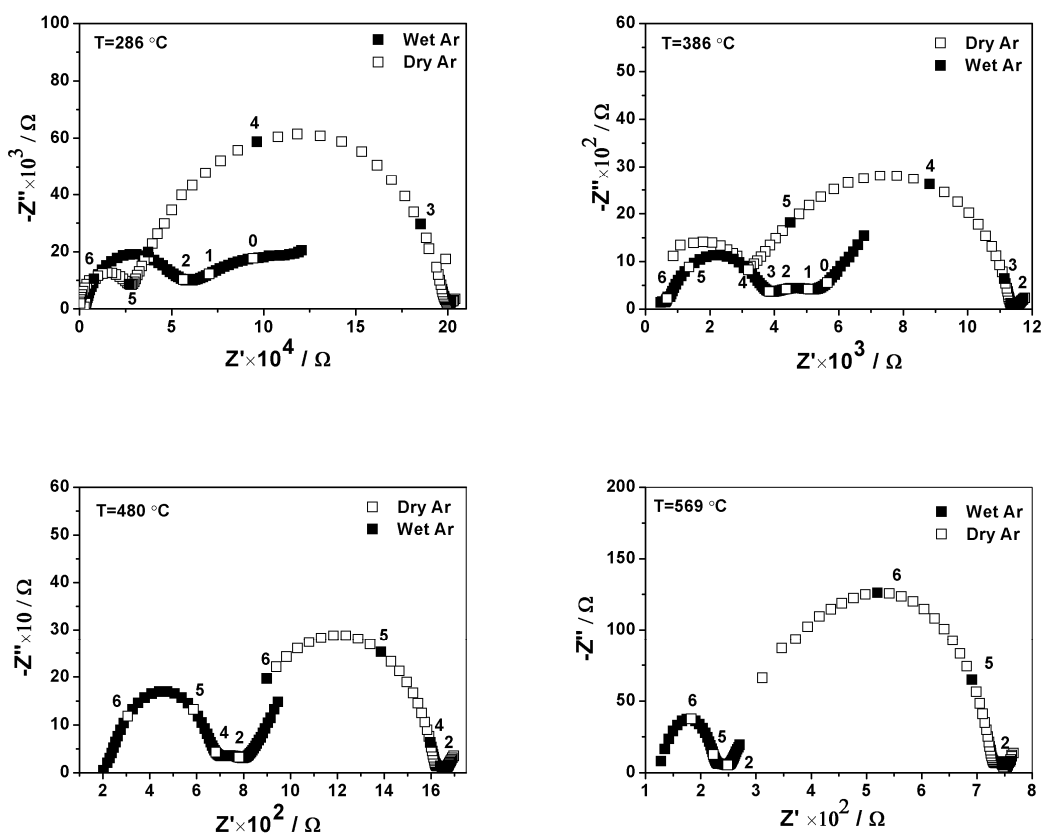


**Figure 3.12** Impedance spectra of  $\text{BaSn}_{0.875}\text{Sc}_{0.125}\text{O}_{3-\delta}$  compound at different temperatures

### 3.5.3.2 Transport properties

The transport properties of  $\text{BaSn}_{1-x}\text{M}_x\text{O}_{3-\delta}$  ( $\text{M} = \text{Sc}, \text{In}, \text{Y}$  and  $\text{Gd}$ ) were investigated by impedance spectroscopy under dry and wet Ar. The conductivities measured are presented in **Figure 3.13** and **Figure 3.14**.

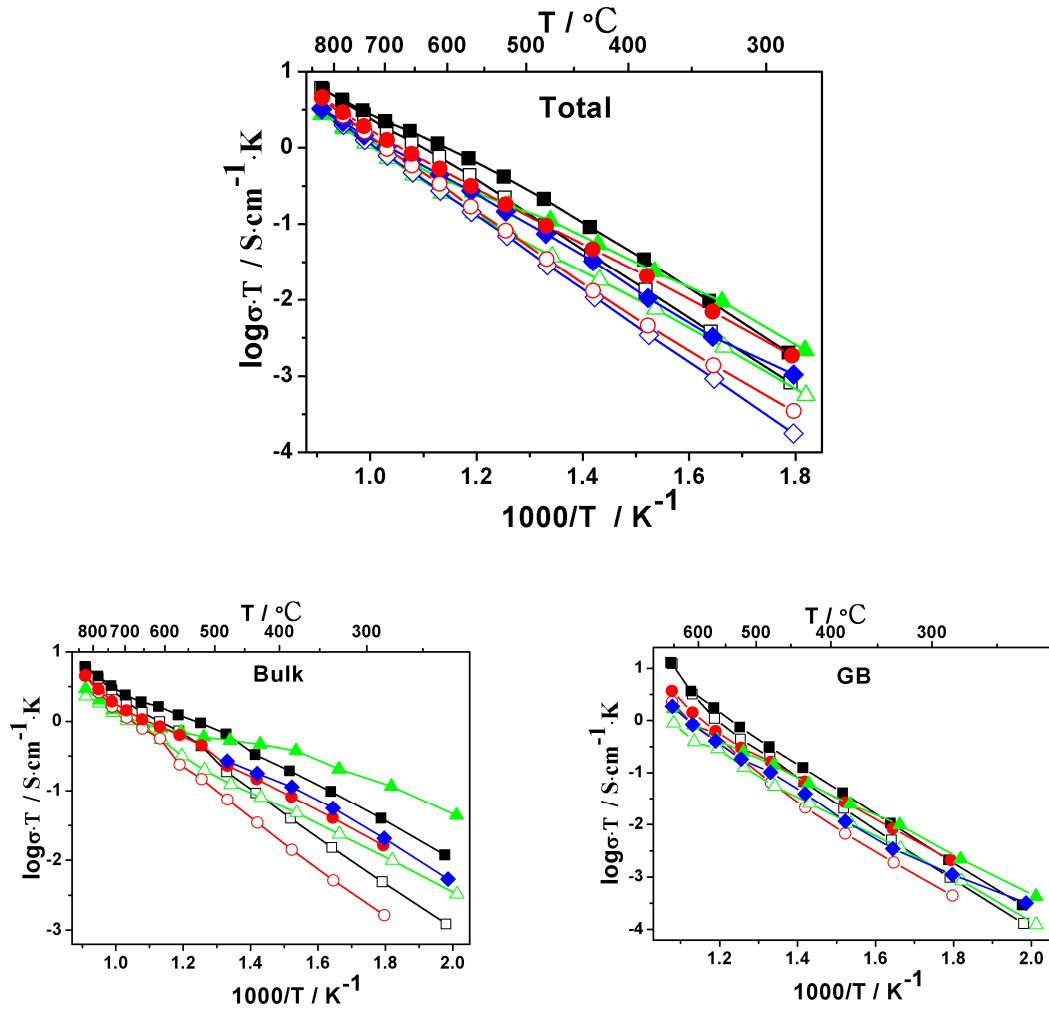


**Figure 3.13** Arrhenius plots of conductivities of  $\text{BaSn}_{0.75}\text{M}_{0.125}\text{O}_{3-\delta}$  ( $\text{M}=\text{Sc}, \text{In}, \text{Y}$  and  $\text{Gd}$ ) in dry and wet Ar. Sc ( $\square$  - Dry Ar,  $\blacksquare$  - Wet Ar), In ( $\circ$  - Dry Ar;  $\bullet$  - Wet Ar), Y ( $\triangle$  - Dry Ar,  $\blacktriangle$  - Wet Ar), Gd ( $\diamond$  - Dry Ar,  $\blacklozenge$  - Wet Ar).

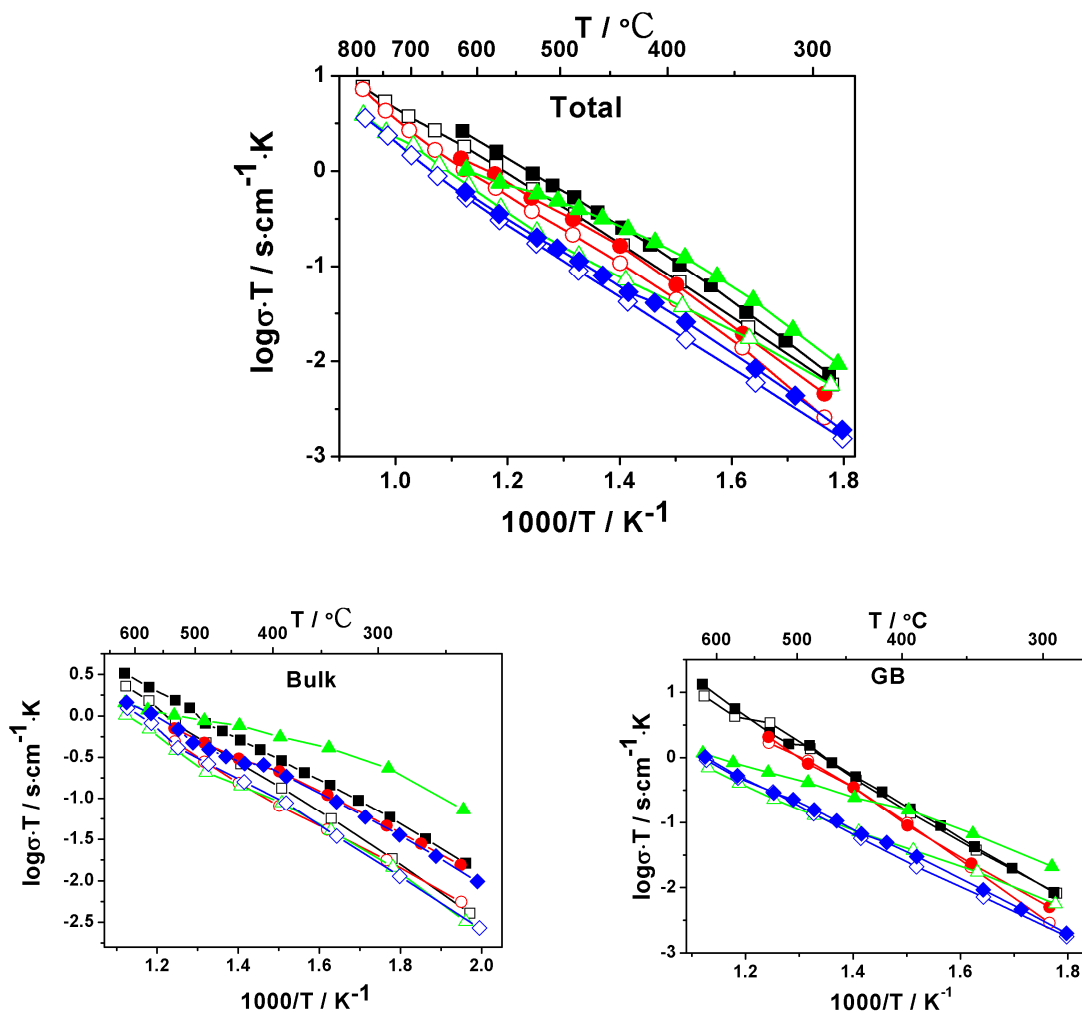


**Figure 3.14** Arrhenius plots of conductivities of  $BaSn_{0.75}M_{0.25}O_{3-\delta}$  ( $M = Sc, In, Y$  and  $Gd$ ) in dry and wet Ar. Sc ( $\square$  - Dry Ar,  $\blacksquare$  - Wet Ar), In ( $\circ$  - Dry Ar;  $\bullet$  - Wet Ar), Y ( $\Delta$  - Dry Ar,  $\blacktriangle$  - Wet Ar), Gd ( $\diamond$  - Dry Ar,  $\blacklozenge$  - Wet Ar).

The conductivities show the same trends with 12.5 mol % and 25 mol % dopant concentration. In the dry atmosphere, the conductivity decreases in the order:  $Sc > Y > In > Gd$ , but in wet Ar at low temperature, the conductivity follows:  $Y > Sc > In > Gd$ . It indicates that there is no obvious correlation between conductivity and the ionic radius of dopant. Similar behaviour was also reported in the  $BaZr_{0.93}R_{0.07}O_{3-\delta}$  ( $R=Sc, Y, Ho, Dy, Gd$  and  $In$ ). In this case, the conductivity in the wet air decreased in the order:  $Y > Ho > Sc > Dy, In > Gd$  [13].

The conductivities increase under wet Ar if compared to under dry Ar, especially for bulk conductivity, suggesting that proton conduction was the main charge carriers at low temperature.

Compound	Total Dry (eV)	Bulk Dry (eV)	Total Wet (eV)	Bulk Wet (eV)
Sc125	0.96	0.69	0.87	0.52
Sc25	0.73	0.63	0.73	0.52
In125	0.97	0.72	0.73	0.50
In25	0.79	0.54	0.76	0.51
Y125	0.89	0.48	0.72	0.38
Y25	0.75	0.50	0.58	0.35
Gd125	0.95	-	0.84	0.52
Gd25	0.78	0.59	0.72	0.53

Note: activation energy was attained by fitting Arrhenius plots with the temperature between 600°C and 800°C for dry Ar, 550°C and 250°C for wet Ar. For Gd dopant, the bulk conductivity can not be separated from the impedance spectrum.

**Table 3.7** Activation energy of  $BaSn_{1-x}M_xO_{3-\delta}$  compounds under dry and wet Ar

The conductivity of Y doped  $BaSnO_3$  under wet Ar is much higher than that of other dopants. In the above section, it was shown that the hydration energies of Y-doped  $BaSnO_3$  is lower than that of Sc- and In-doped, suggesting that the proton concentration is lower for this dopant under wet atmosphere. Thus this high conductivity observed suggests that Y as an acceptor dopant is favourable for the proton mobility. Similar results have been reported for Y-doped  $BaZrO_3$  and it was argued that Y dopant tends to “push” the proton out of the edge of the  $BO_6$ -octahedron, *i.e.* bend hydrogen bonds are formed [10]. Table 3.7 also shows that the proton mobility in Y-doped  $BaSnO_3$  is significantly higher with much lower activation energy (0.35 eV~0.38 eV), and is almost independent of the dopant concentration. Islam *et al.* [14] also reported that there is an association between the dopant ion and the protonic defect (hydroxyl ion at oxygen site), which may affect proton mobility, and he calculated the binding energies of hydroxyl ion and a

neighbouring dopant substitution ( $OH_oM'_{Zr}$ ) in  $BaZrO_3$ : Sc (-0.74 eV), Y (-0.26 eV) and In (-0.58 eV). These results indicate that proton mobility is very sensitive to the type of acceptor dopant ion, and that  $Y^{3+}$  would be favourable for low dopant-proton association energy.

### 3.6 Conclusion

The synthesis, defect chemistry and proton conductivities in the perovskite  $BaSn_{1-x}M_xO_{3-\delta}$  ( $x = 0.125$  and  $0.25$ ,  $M = Fe, Sc, In, Y, Gd, Sm, Nd$  and  $La$ ) have been investigated. Structural characterization reveals that all compounds present cubic perovskite structure (Space group:  $Pm\bar{3}m$ ). The lattice parameters do not show the systemic trend with the radii of dopants, but an abnormal drop for Sm, Nd and La. The small cell parameters of the Sm-, Nd- and La- doped  $BaSnO_3$  can be explained by a partial occupation of the Ba-site. The thermal expansion is almost independent on dopants ions. The highest values of water uptake and proton conductivities are observed for Sc- and Y-doped  $BaSnO_3$ , respectively. It indicates that Y as acceptor dopant is favourable for the proton mobility, while high negative hydration enthalpy for Sc-doped  $BaSnO_3$  stabilise the proton at higher temperature within the structure and probably traps it and thus impedes its movement.

## References

- [1] R. Glockner, M. S. Islam, T. Norby, *Solid State Ionics* **1999**, 122, 145.
- [2] R. A. Davies, M. S. Islam, J. D. Gale, *Solid State Ionics* **1999**, 126, 323.
- [3] J. Wu, L. P. Li, W. T. P. Espinosa, S. M. Haile, *J. Mat. Res.* **2004**, 2366.
- [4] N. Ito, H. Matsumoto, Y. Kawasaki, S. Okada, T. Ishihara, *Solid State Ionics* **2008**, 179, 324.
- [5] R. D. Shannon, *Acta Cryst.* **1976**, A32, 751.
- [6] M. Mogensen, D. Lybye, N. Bonanos, P. V. Hendriksen, F. W. Poulsen, *International conference on ionic and mixed conducting ceramics*, San Francisco, CA (US), 2002, **2001**.
- [7] E. Bévillon, A. Chesnaud, Y. Z. Wang, G. Dezanneau, G. Geneste, *J. Phys.: Condens. Matter* **2008**, 145217
- [8] K. D. Kreuer, *Ann. Rev. Mater. Res.* **2003**, 33, 333.
- [9] Y. Yamazaki, P. Babilo, S. M. Haile, *Chemistry of Materials* **2008**, 20, 6352.
- [10] K. D. Kreuer, S. Adams, W. Munch, A. Fuchs, U. Klock, J. Maier, *Solid State Ionics* **2001**, 145, 295.
- [11] P. Murugaraj, K. D. Kreuer, T. He, T. Schober, J. Maier, *Solid State Ionics* **1997**, 98, 1.
- [12] E. Bevillon, G. Geneste, *Physical Review B* **2008**, 77, 184113.
- [13] V. P. Gorelov, V. B. Balakireva, Y. N. Kleshchev, V. P. Brusentsov, *Inorganic Materials* **2001**, 37, 535.
- [14] M. S. Islam, P. R. Slater, J. R. Tolchard, T. Dinges, *Dalton Transactions* **2004**, 3061.

# Chapter 4 Structure, Proton Incorporation and Conductivity of Y-Doped BaSnO<sub>3</sub>

## 4.1 Introduction

In the previous chapter, the structural properties, proton incorporation and conductivities of acceptor doped BaSnO<sub>3</sub> have been systemically studied. The results have shown that Y-doped BaSnO<sub>3</sub> compounds possess good conductivity, in particular, significant proton conductivity at low temperature in humidified atmosphere. In this chapter, BaSn<sub>1-x</sub>Y<sub>x</sub>O<sub>3-δ</sub> compounds (denoted  $x = 0, 0.05, 0.125, 0.25, 0.375$  and  $0.50$  as BSO, BSY5, BSY125, BSY25, BSY375 and BSY50 in the following) were investigated deeply in order to understand the effect of dopant content on the microstructure, chemical stability and transport properties.

BaSn<sub>1-x</sub>Y<sub>x</sub>O<sub>3-δ</sub> compounds were synthesised by a gel polymerization route, calcined at 1200°C for 4 h, and then sintered at 1600°C for 12 h to give dense materials, *i.e.* following the same experimental process as described in chapter 2. The structural and microstructural properties were characterized by XRD and SEM. Water incorporation was analyzed by TGA. The conductivities as a function of temperature, oxygen partial pressure and humidity were investigated by impedance spectroscopy, which allows revealing the main charge carriers depending on thermodynamic conditions. From these measurements, we discuss the influence of microstructure and dopant content on transport properties.

## 4.2 Microstructural and structural properties

The morphology of the as-prepared powder is presented by SEM micrographs in **Figure 4.1**. It consists in flake-like aggregates with around 1 μm size. For these powders obtained at 1200°C, the grain size is about 50 nm. These agglomerates were in part broken down by a ball milling at 400 rpm for 2 h. The ball-milling also leads to more homogeneous powders as evidenced by **Figure 4.1 (b)**. Nevertheless, some agglomeration

still subsists after this treatment. The morphology of sintered pellets is shown in **Figure 4.2**. In this case, the grain size of the compounds seems to increase with the yttrium content from less than 0.5  $\mu\text{m}$  for the BSY5 to several microns for higher yttrium contents. These SEM micrographs also reveal the high density obtained for the sintered samples.

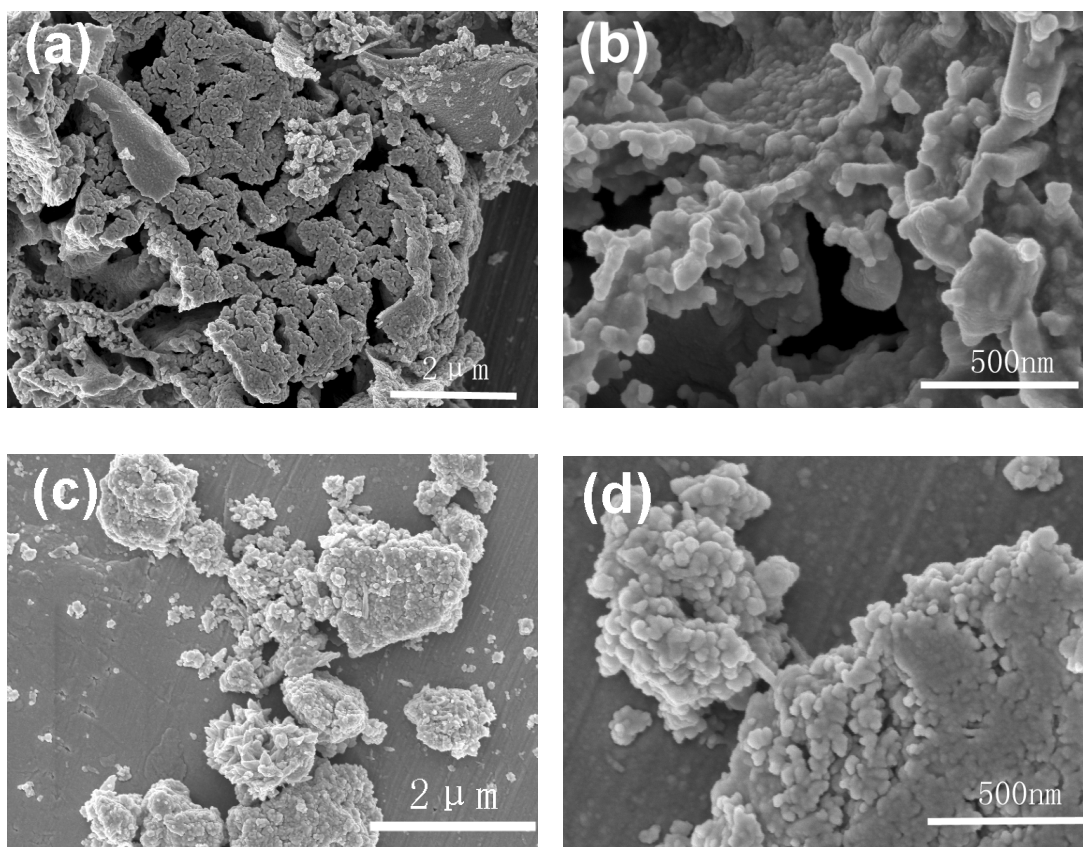


**Figure 4.1** SEM pictures of BSY375 powder heat-treated at 1200°C for 4 h: (a) and (b): not milled, (c) and (d): after ball milling.

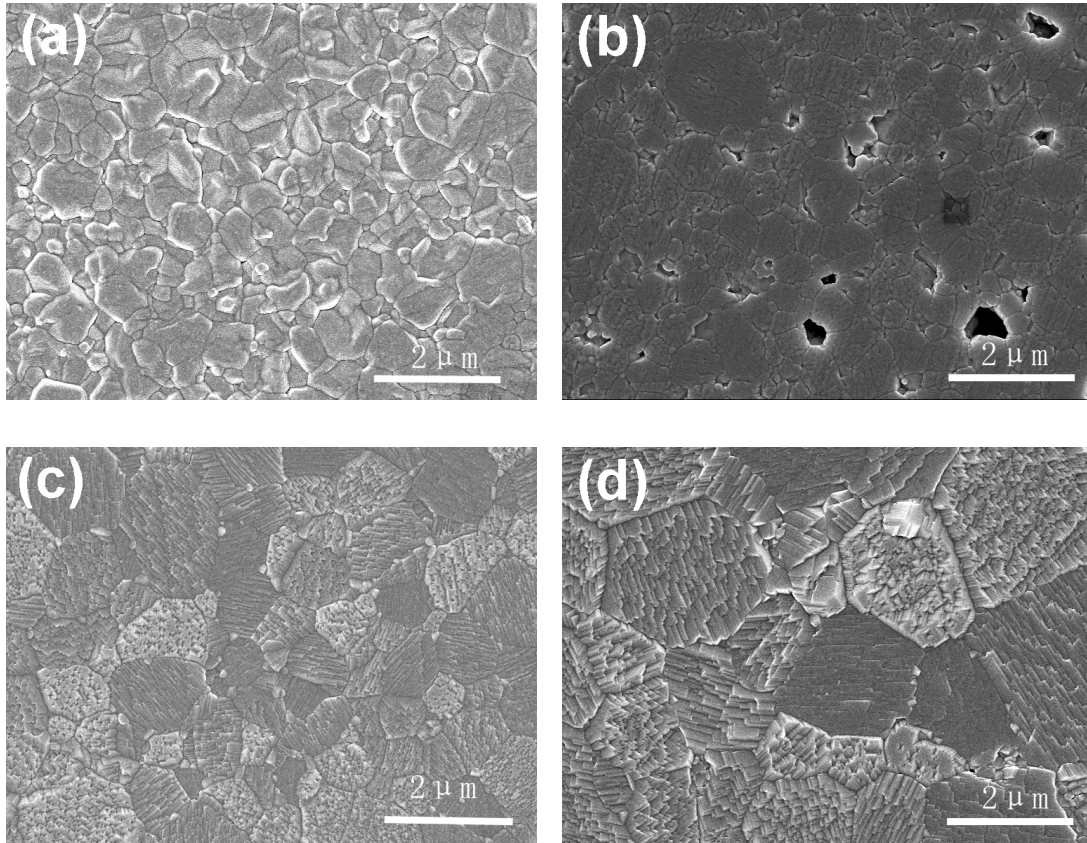


**Figure 4.2** SEM pictures of BaSn<sub>1-x</sub>Y<sub>x</sub>O<sub>3- $\delta$</sub>  pellets sintered at 1600°C for 12 h: (a)  $x = 0.05$ , (b)  $x = 0.125$ , (c)  $x = 0.25$ , (d)  $x = 0.375$ .

X-ray diffraction of the BaSn<sub>1-x</sub>Y<sub>x</sub>O<sub>3- $\delta$</sub>  powders and pellets are shown in **Figure 4.3(a) and (b)**, respectively. While some small “parasitic” peaks are observed for the powders, corresponding to barium carbonate and to the  $k_{\beta}$  diffraction peak, the pellets diagrams can be indexed in a pure non-distorted cubic perovskite phase (Space Group:  $Pm\bar{3}m$ ). BSY50 composition was reported to crystallise in a perovskite-type structure with a double unit cell ( $a = 844$  pm) due to an ordering of the B-site cations [1]. This doubling of unit cell is never observed here even for the  $x = 0.5$  composition. Besides, while powders for  $x = 0.5$  could be obtained with an almost pure perovskite phase after heat-treatment at 1200°C, the pellet prepared for the same composition break during sintering. The other pellets for this composition will break into pieces during the heat treatment after polishing and deposition of electrodes, indicating a poor stability. The poor stability of this composition was actually mentioned to exist by Murugaraj *et al.* [1] under

wet and reducing conditions.

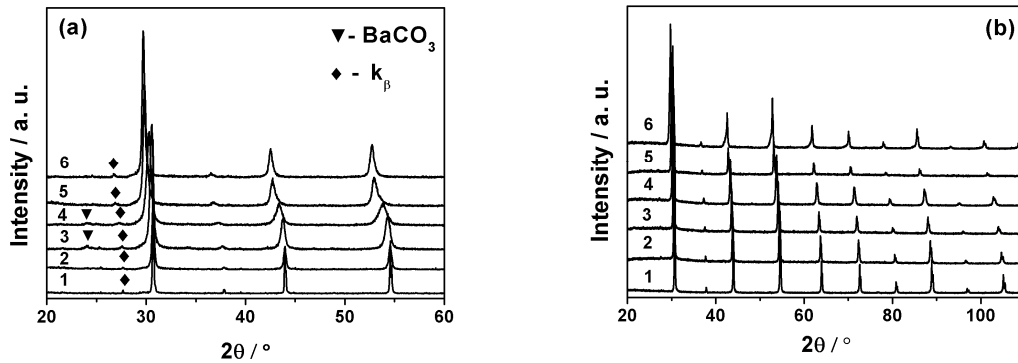


**Figure 4.3** X-ray diffraction patterns of BaSn<sub>1-x</sub>Y<sub>x</sub>O<sub>3-δ</sub> powders and Pellets: (a) Powders calcined at 1200°C for 4 h in air, (b) Pellets sintered at 1600°C for 12 h in air. (1)  $x = 0.0$ , (2)  $x = 0.05$ , (3)  $x = 0.125$ , (4)  $x = 0.25$ , (5)  $x = 0.375$ , (6)  $x = 0.50$ .

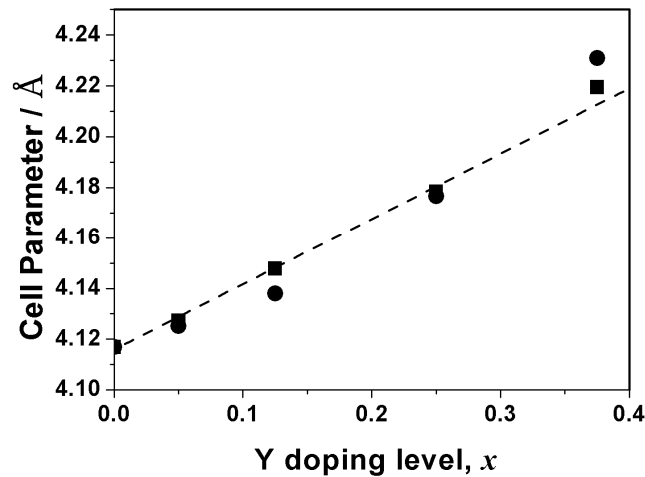


**Figure 4.4** Cell parameter as a function of Y doping level in BaSn<sub>1-x</sub>Y<sub>x</sub>O<sub>3-δ</sub> (●: powder, ■: pellet).

The cell parameters increase with yttrium content, see **Figure 4.4**, as might be expected from the respective ionic radii in a 6-fold coordination of Sn<sup>4+</sup> ions (0.69 Å) and Y<sup>3+</sup> ions (0.9 Å) according to the tabulation of Shannon [2]. The question nevertheless arises whether this linear evolution is fully coherent with the difference in radius size between Sn<sup>4+</sup> and Y<sup>3+</sup> cations. The previous chapter, we have shown from the study of Wu *et al.* [3] that it exists a clear correlation between the respective volume of cations in Ba-containing perovskite and the cell volume. An empirical law was then proposed:

$$V_{\text{cell}} = -478 + 10.3 V_{\text{sum-ions}} \quad (4-1)$$

Where,  $V_{\text{cell}}$  corresponds to the volume of the ABO<sub>3</sub> perovskite cell and  $V_{\text{sum-ions}}$  to the sum of equivalent volumes of the different cations considered as spheres. The radii of atoms are those given by Shannon [2].

In the case of two cations on a same site, the equivalent volume will correspond to that of a sphere with the mean radius. On the following graph (Figure 4.5), we present the results of such calculations in the case of BaSn<sub>1-x</sub>Y<sub>x</sub>O<sub>3-δ</sub> compounds. We also present on this graph the results previously given by Wu *et al.* [3] corresponding to different barium-based perovskite materials. Let us precise here that, as proposed by Wu *et al.*, the volume of oxygen vacancies is considered to be equal to that of oxygen atoms. Here, we also considered that Y<sup>3+</sup> cations were placed only on B-site in substitution to Sn<sup>4+</sup>. The results reveal a very good agreement between the proposed law and what found for BSY compounds. This confirms that such law works well for acceptor-doped compounds with oxygen vacancies and that the model of substitution of Sn<sup>4+</sup> by Y<sup>3+</sup> atoms on B-site is reasonable.

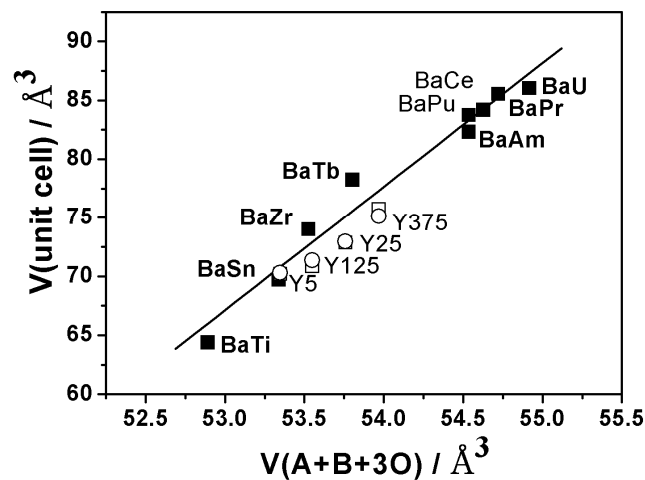


**Figure 4.5** Pseudo-cubic cell volume of barium-based perovskites as a function of the sum of the ionic radii of the constituent species for standard compounds (solid squares. See ref.[3]).

BaSn<sub>1-x</sub>Y<sub>x</sub>O<sub>3-δ</sub> powders (open circles) and BaSn<sub>1-x</sub>Y<sub>x</sub>O<sub>3-δ</sub> pellets (open squares).

From X-ray data, we could also calculate the theoretical density of BaSn<sub>1-x</sub>Y<sub>x</sub>O<sub>3-δ</sub> compounds. This theoretical density is shown to diminish with Yttrium content corresponding both to a diminishing of the molecular weight of the formula unit and to the increase of cell parameters. The relative density of pellets is almost the same for all compositions, *i.e.* around 90 %. This seems to indicate that the native microstructure of powders with some aggregates impedes the preparation of fully dense pellets. Surprisingly, the yttrium content has a small influence on densification in spite the fact that the grain size and thus the diffusion seems to be favoured by higher yttrium contents. The greater density *i.e.* 94 % is nevertheless observed for the  $x = 0.375$  compound, as also proved by SEM pictures (**Figure 4.2**).

Compounds	Molecular Weight (g/mol)	Cell parameter (Å)	Cell volume (Å <sup>3</sup> )	Theoretical density (g/cm <sup>3</sup> )	Observed Density (g/cm <sup>3</sup> )	Relative Density (%)
BSO	304.03	4.1169(4)	69.776	7.23	6.52	90.2
BSY5	302.14	4.1273(14)	70.306	7.14	6.31	88.4
BSY125	299.31	4.1478(7)	71.359	6.96	6.31	90.6
BSY25	294.58	4.1784(48)	72.950	6.70	6.09	90.9
BSY375	289.86	4.2195(22)	75.1247	6.41	6.04	94.3

**Table 4.1** Cell parameters, theoretical and experimental density of BaSn<sub>1-x</sub>Y<sub>x</sub>O<sub>3-d</sub> compounds.

### 4.3 Thermodynamic analysis of water uptake

The experimental process and data analysis for water uptake are the same as those described in **chapter 3**. Water uptake obtained from the thermogravimetric analysis is presented in **Figure 4.6**. The behaviour is similar for all compounds. At high temperature (600-1000°C), the weight becomes constant within 2 h for all compounds. At lower temperature, the time for equilibrium of hydration reaction changes slightly with composition, being in the range of 5-10 h for high Y content. Water uptake increases with Y content due to the increase of oxygen vacancies available for reaction with water, and water uptake mainly occurs at low temperature (below 550°C), which is a typical temperature range of water uptake for perovskite proton conductor [1, 4-6].

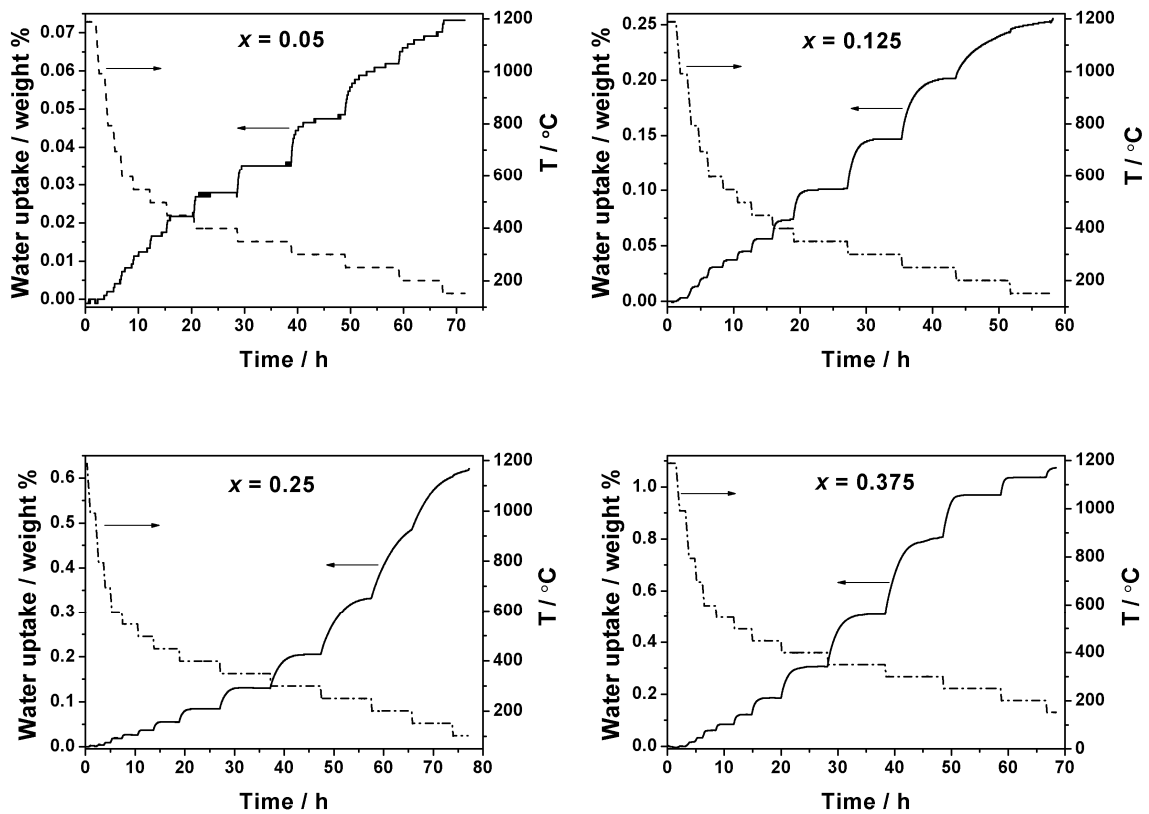


**Figure 4.6** Water uptake of BaSn<sub>1-x</sub>Y<sub>x</sub>O<sub>3-δ</sub> samples and temperature as a function of time under P(H<sub>2</sub>O) = 0.021 atm.

Analysis of the raw data in the **Figure 4.6** yields the proton concentration and equilibrium constant as a function of temperature summarized in **Figure 4.7 (a) and (b)**, respectively.

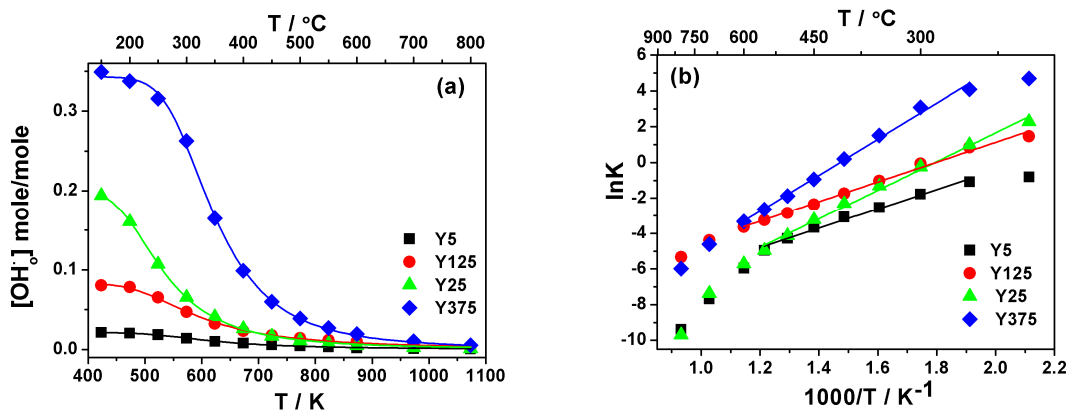


**Figure 4.7** Hydration behaviour of BaSn<sub>1-x</sub>Y<sub>x</sub>O<sub>3-δ</sub> with Y doping level: (a) Hydration isobars, (b) Equilibrium constant of the hydration reaction.

**Figure 4.7 (b)** shows that the equilibrium constant as a function of inverse temperature is not linear in the whole range of temperatures. At low temperature (below 600 °C), the weight changes are mostly due to hydration,  $\ln K$  is linear in the Arrhenius representation. At high temperature, however, the behaviour deviates from linearity. As already shown in the previous chapter and recently argued by Yamzzaki *et al.* [6], this is probably due to the an evolution of the thermodynamic parameters with temperature or to the contribution of holes (see below). Below 250°C, the values also deviate from linearity, probably because of too slow hydration kinetics.

Y Dopant level (mol %)	$\Delta H_{hydr}^{\circ} / \Delta H_{hydr}^{\circ *}$ kJ mol <sup>-1</sup>	$\Delta S_{hydr}^{\circ} / \Delta S_{hydr}^{\circ *}$ J mol <sup>-1</sup> K <sup>-1</sup>	$[M'_{Sn}]_{effective}$	Reference
0.05	-60.24/-45.36	-106.73/-94.29	0.0213	This study
0.125	-59.37/-49.10	-97.11/-86.98	0.0836	
0.25	-69.15/-72.53	-120.38/-128.52	0.2010	
0.375	-93.81/-83.91	-136.33/-123.45	0.3431	
0.1	-60	-	-	[7]
0.25	-79.1	-	-	
0.375	-81.95	-	-	
0.40	-84.27	-	-	

Note: Effective dopant concentration was attained by fitting the proton concentration.

(\*): Enthalpy and entropy were obtained by fitting  $\ln K$  verse  $1/T$  between 600 °C and 200 °C.

**Table 4.2** The effective dopant concentration, entropy and enthalpy of doped BaSnO<sub>3</sub>.

The enthalpy and entropy of hydration are obtained by fitting hydration isobars between 200°C and 800°C and equilibrium constant in the linear part between 600°C and 200°C in the **Figure 4.7**, summarized in **Table 4.2**. The effective dopants concentrations are obtained by fitting the proton concentration as shown in the **Figure 4.7 (a)**. They are 0.0213, 0.0836, 0.201 and 0.3431 for BSY5, BSY125, BSY25 and BSY375 compounds, respectively. These values are not very close to what expected for full saturation of protons into structure, 0.05, 0.125, 0.25 and 0.375, respectively. Similar results were

reported in Y-doped BaZrO<sub>3</sub> [6]. **Table 4.2** shows that the hydration enthalpy is close to the data reported by Kreuer [7], and the values of enthalpy and entropy obtained using the direct fitting hydration isobars are more negative than that of a fitting of hydration equilibrium constant due to an increase in slope at higher temperature. Yamzzaki *et al.* [6] showed that the values of  $\Delta H$  and  $\Delta S$  depend on the temperature range chosen for fitting, *i.e.* for 20 mol % Y-doped BaZrO<sub>3</sub>, the values of  $\Delta H$  and  $\Delta S$  obtained are  $-22 \pm 1$  kJ/mol and  $-39 \pm 1$  J/mol respectively at temperature between 50°C and 500°C [6], and  $-93.3$  kJ/mol and  $-103.2$  J/mol respectively at temperature between 550°C and 900°C [5]. However, in the present study, the values of  $\Delta H$  and  $\Delta S$  deduced from the fitting of  $[OH_o]$  are only slightly different from the values obtained from the fitting of  $\ln K$ .

## 4.4 Transport properties

### 4.4.1 Analysis of impedance spectra

We represent Nyquist plots ( $Z_{\text{imag}}$  versus  $Z_{\text{real}}$  as parametric function of frequency) for the BSY125 compound at different temperatures in wet and dry argon atmospheres in **Figure 4.8**. These graphs are representative of the general aspect of impedance spectra observed in the whole series of samples. They evidence first that, under wet atmosphere, the impedance of sample diminishes strongly as compared to dry atmosphere. Besides, as shown in this figure, contributions of both bulk and grain boundaries can most often be well identified and separated. The conductivities associated to the bulk and grain-boundary contributions are then deduced from the least squares fitting of the impedance data, by using for each contribution an equivalent electrical element consisting of a resistance in parallel with a constant phase element.

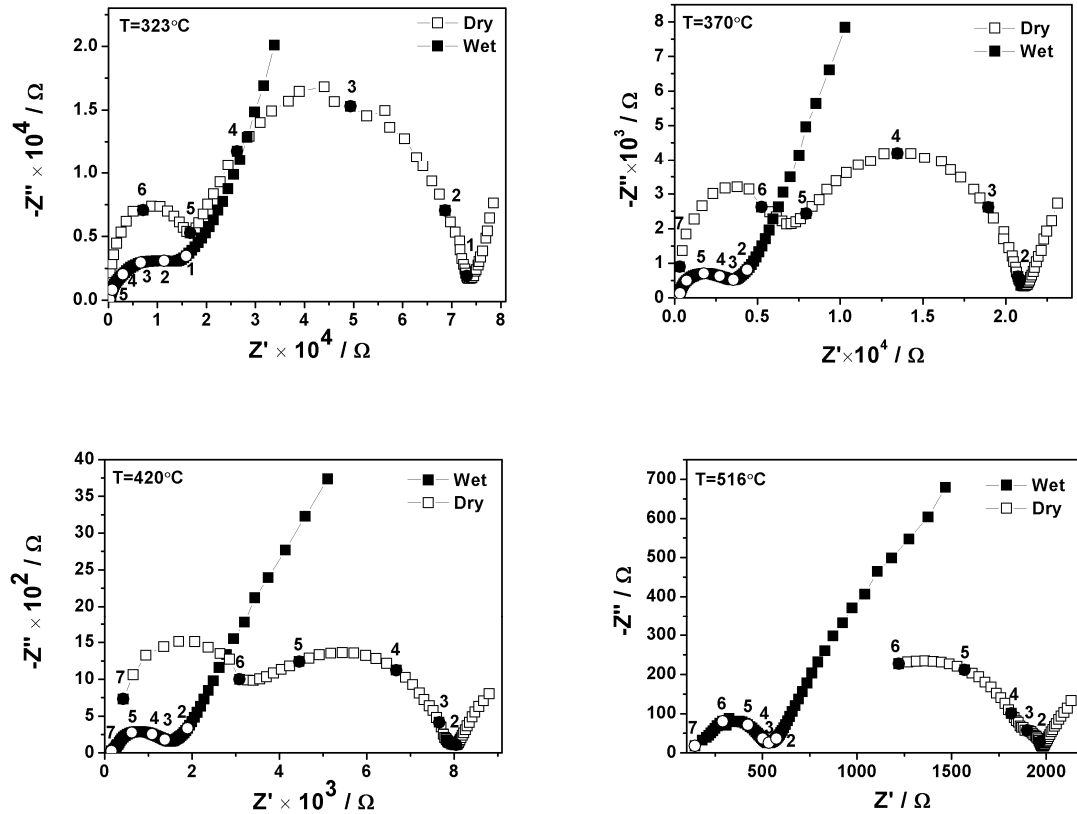
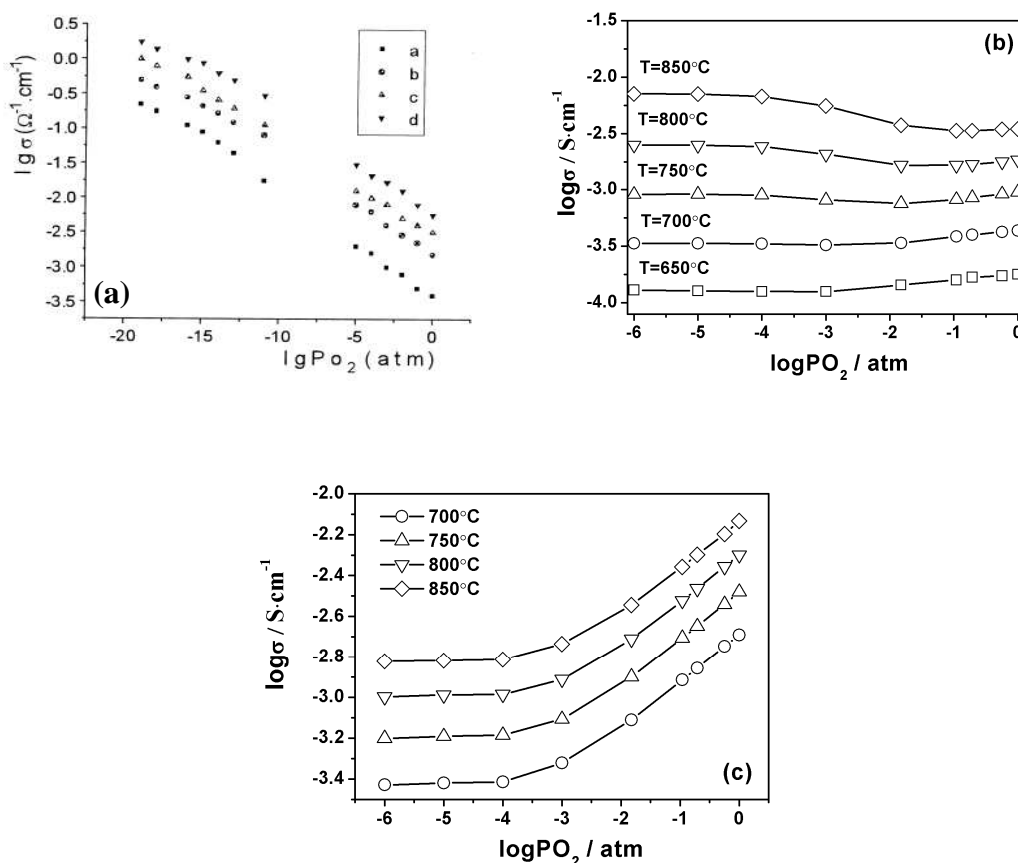


Figure 4.8 Impedance Spectra of BSY125 in dry and humidified Ar at different temperatures.

#### 4.4.2 Transport properties as a function of P(O<sub>2</sub>)

Conductivity measurements have been measured for all samples as a function of oxygen partial pressure between  $10^{-5}$  and 1 atm. During these measurements, the stabilisation time was around 1-2 h and adjusted depending on the evolution of the impedance spectrum. The results were very similar for all compounds excepted for pure BaSnO<sub>3</sub> for which a complex behaviour is observed. Pure BaSnO<sub>3</sub> is known to present a n-type behaviour [8]. **Figure 4.9 (a)** shows that the conductivity of BaSnO<sub>3</sub> continuously decreases with the increase of oxygen partial pressure [9]. However, the behaviour observed in this study is very different and shows a transition between a n-type behaviour at low oxygen partial pressure and high temperature to a p-type behaviour at high oxygen partial pressure and low temperature. Besides, one surprising point is the high value of conductivity obtained in spite of the absence of voluntarily introduced defects. The

understanding of non doped BaSnO<sub>3</sub> is out of the scope of the present study. Nevertheless, a fine study of BaSnO<sub>3</sub> properties at high temperature would be probably necessary and would suppose to study a range of compositions with varying Ba over Sn contents. Indeed, the presence of Ba vacancies cannot be discarded in the actual compound.



**Figure 4.9** The total conductivity of (a) Electrical conductivity of BaSnO<sub>3</sub> [9] (a: 1116 K, b: 1173 K, c: 1216 K, d: 1273 K.), (b) BaSnO<sub>3</sub>, (c) BSY125 as a function of oxygen partial pressure.

Let us thus come back to doped compounds, the measurements versus oxygen partial pressure are presented in **Figure 4.9 (c)** for the  $x = 0.125$  compound. This figure evidences an evolution of conductivity with  $P(\text{O}_2)$  very similar to that of other proton conductors such as barium zirconates or cerates. Indeed, the material changes from pure anion conducting compound with no evolution of conductivity with  $P(\text{O}_2)$  to a p-type conducting behaviour with an evolution of conductivity  $P(\text{O}_2)$  following a  $1/4$  power law.

This behaviour corresponds to the situation where anion vacancies are still the major defect in terms of concentrations but due to the higher mobility of holes, their conductivity overpasses anion conductivity at high oxygen partial pressure. Conductivity can then be fitted by the following law [10]:

$$\sigma_{\text{total}}(T) = \sigma_{\text{anion}}(T) + \sigma_{\text{holes}}(T) P(\text{O}_2)^{1/4} \quad (4-2)$$

From which some fundamental characteristics of anion or holes transport can be extracted. The numerical results of such fitting are given in **Table 4.3**. We see that the anion migration energy decreases with Y<sub>2</sub>O<sub>3</sub> content from 1.32 eV for BSY5 to 0.96 eV for BSY375. This value is close to the ones observed for other compounds, *e.g.* 0.77 eV for SrCe<sub>0.95</sub>Yb<sub>0.05</sub>O<sub>3</sub> [10] and 1.06 eV for Ba<sub>2</sub>SnYO<sub>5.5</sub> [1]. The fitting procedure gives also an activation energy for the hole conduction process. Nevertheless, since this activation energy reflects both hole formation energy and their migration energy, it does not allow separating concentration and mobility contributions to the conductivity. Concerning hole conductivity activation energy, we observe that it is correlated to oxygen migration activation energy. Such an effect was previously observed by Tuller *et al.* [10], and was assigned to the fact that the transport of holes consisting of O<sup>-</sup> species and better described by a polaron behaviour is probably linked to oxygen vibrations, that also influences oxygen transport.

Compounds	Oxygen vacancy activation energy (eV) <sup>(1)</sup>	Hole conductivity activation energy (eV) <sup>(1)</sup>
BSY5	1.32	1.03
BSY125	1.17	0.909
BSY25	1.04	0.801
BSY375	0.96	0.829

<sup>(1)</sup> Measured from fitting of conductivity versus  $P(\text{O}_2)$  in the 650-850 °C temperature range.

**Table 4.3** Activation energies of anion and hole from total conductivity in BSY compounds.

#### 4.4.3 Conductivities as a function of temperature in different atmospheres

The conductivities of BaSn<sub>1-x</sub>Y<sub>x</sub>O<sub>3-δ</sub> were investigated under different atmospheres since protons, oxygen vacancies, electrons and holes all coexist, with their concentration dependent on dopant concentration, temperature, oxygen partial pressure and water partial pressure. All the measurements were carried out upon cooling from 850°C, and the cooling rate was 200 °C/h for dry atmosphere, 50 °C/h for wet atmosphere.

#### 4.4.3.1 Reproducibility of measurements

In order to verify the stability of samples and the reproducibility of measurements in different atmospheres, the conductivities under dry Ar were measured several times during the measurements. The order of measurements was: **Dry Ar (1<sup>st</sup>) → Wet Ar → Wet 5H<sub>2</sub>/Ar → Dry Ar (2<sup>nd</sup>) → Dry air → Wet air → Dry Ar (3<sup>rd</sup>)**. The Arrhenius plots of total conductivities of BaSn<sub>1-x</sub>Y<sub>x</sub>O<sub>3-δ</sub> in dry Ar are presented in **Figure 4.10** for all samples.

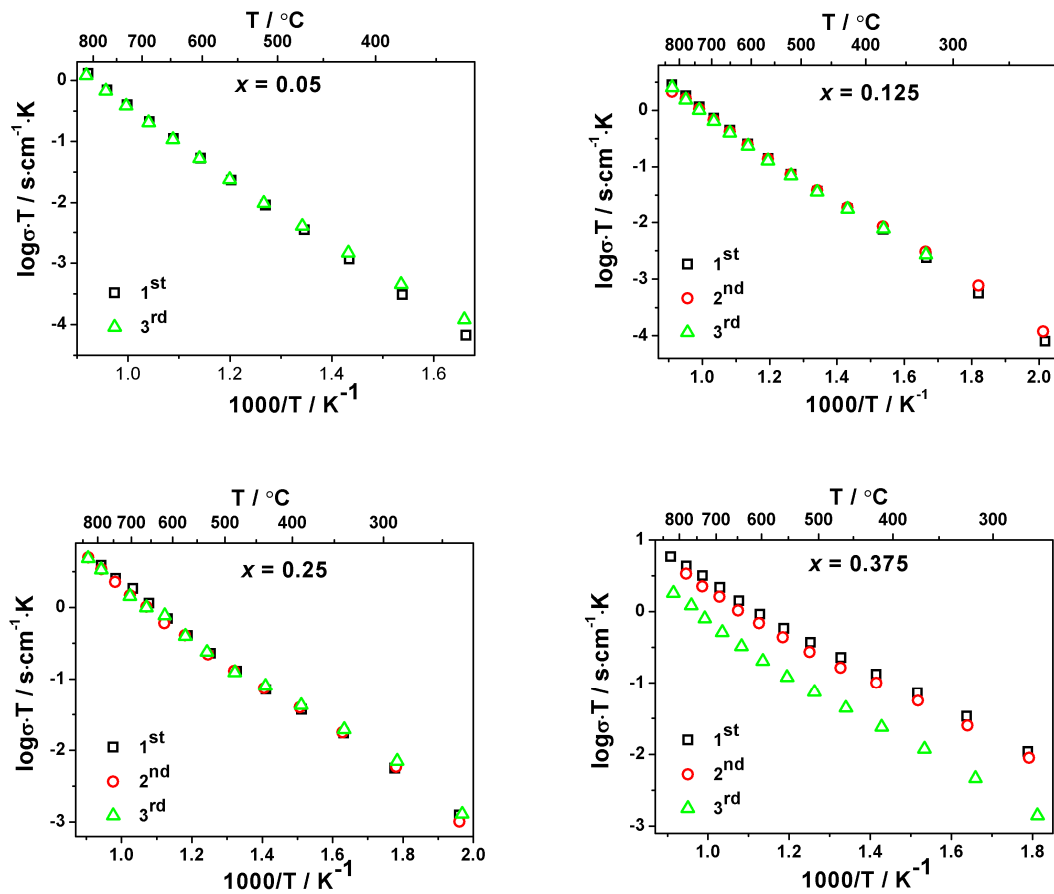


**Figure 4.10** Arrhenius plots of total conductivities of BaSn<sub>1-x</sub>Y<sub>x</sub>O<sub>3-δ</sub> in dry Ar with different times.

For BSY5, BSY125 and BSY25, **Figure 4.10** shows that the conductivities in dry Ar have almost kept the same values during all measurements. It is even surprising that the conductivities increase slightly compared with the 1<sup>st</sup> measurement at low temperature. This is probably due to the proton “freezing” in the structure after measuring under wet atmosphere. However, for BSY375, the conductivity has degraded slightly in the 2<sup>nd</sup> measurement, and decreased sharply in the 3<sup>rd</sup> time measurement. After measurements, we observed that the sample was broken, which in great part justifies to the sharp decrease of the 3<sup>rd</sup> conductivity measurement. The instability of structure may be induced by hydration due to the high concentration of oxygen ion vacancies. The same behaviour was also reported in the Ba<sub>2</sub>SnYO<sub>5.5</sub> by Murugaraj *et al.* [1]. With these results, we want to put emphasis on the fact that interpretation for the  $x = 0.375$  composition should be considered with care due to the obvious instable state of this sample.

#### 4.4.3.2 Influence of P(O<sub>2</sub>) and P(H<sub>2</sub>O) on conductivity

In this part, we want to comment what the conductivity look like in dry and wet Ar, dry and wet air, and wet Ar/H<sub>2</sub>. The objective is to make as clear as possible the main differences between oxidative neutral and reducing atmospheres, and between dry and wet atmospheres.

**Figure 4.11** shows the total, bulk and grain conductivities of 5 mol % Y-doped BaSnO<sub>3</sub> as a function of temperature in different atmospheres. Here this composition is detailed to illustrate the general behavior. The differences observed for other compositions will be commented in the following.

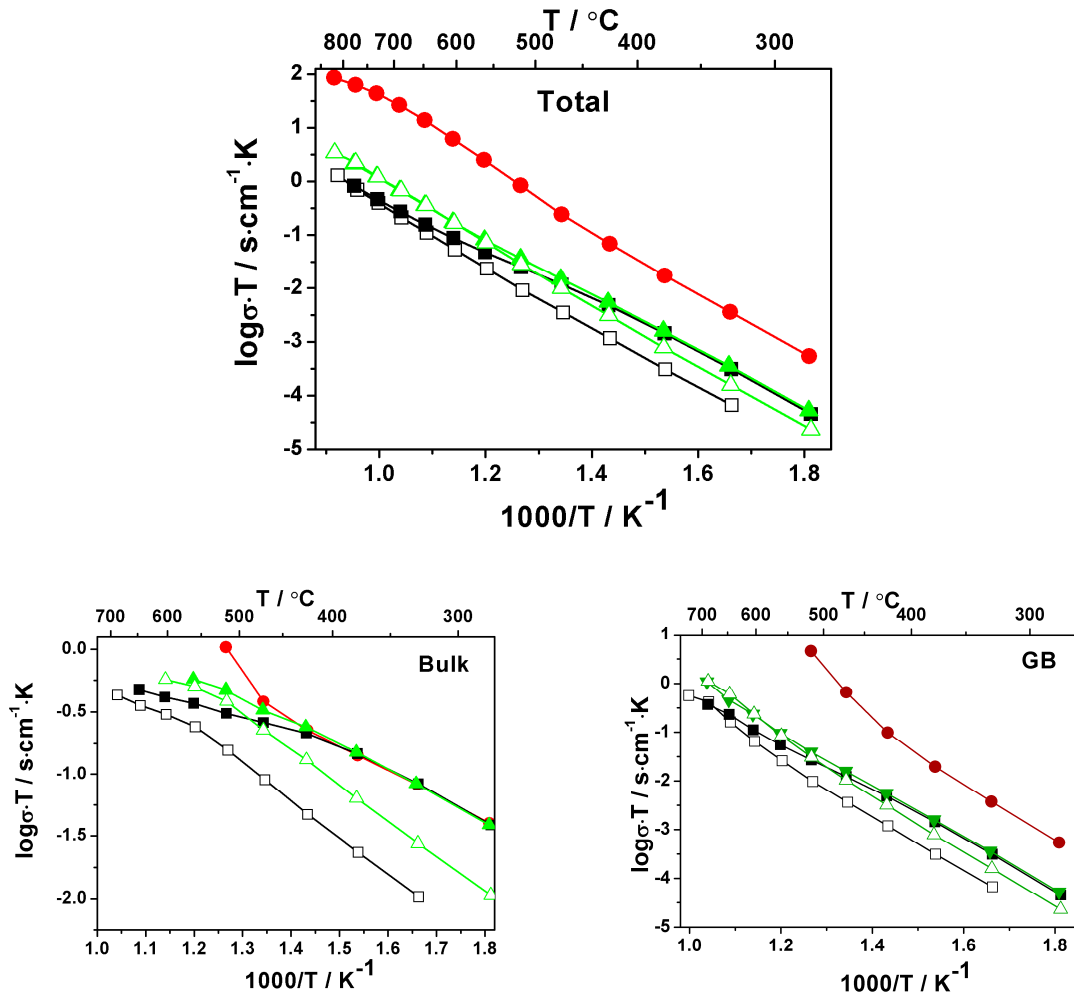


**Figure 4.11** Arrhenius plots of total and bulk conductivities of 5 mol % Y-doped BaSnO<sub>3</sub> at different atmosphere under different atmospheres.

(□ - Dry Ar, ■ - Wet Ar, △ - Dry air, ▲ - Wet air, ● - Wet 5H<sub>2</sub>/Ar)

The conductivity measured under wet atmosphere shows a high conductivity compared with the measurement under dry atmosphere at low temperature, while the difference is not so obvious at high temperature. The effect of humidity is especially visible for bulk conductivity. This is typical for proton conducting materials due to the absorption of steam resulting in enhanced proton conduction [11-13]. For Grain boundaries, the difference between dry and wet atmosphere is much smaller. From this, it is already anticipated that only materials with important grain sizes will present significant proton conduction.

The total conductivity under wet 5H<sub>2</sub>/Ar is significantly higher (one order of magnitude) than in wet air or Ar. The bulk conduction is independent of PO<sub>2</sub> at low temperature (below 500 °C), which has also been reported in Ba<sub>3</sub>Ca<sub>1.18</sub>Nb<sub>1.82</sub>O<sub>9-δ</sub> [14] and 5 mol % Ca doped BaCeO<sub>3</sub> [15]. Thus, the increased total conductivity at low temperature comes clearly from the contribution of grain boundary conductivity. The grain boundary conductivities of Ba<sub>0.97</sub>Zr<sub>0.77</sub>Y<sub>0.19</sub>Zn<sub>0.04</sub>O<sub>3-δ</sub> and BaZr<sub>0.8</sub>Y<sub>0.2</sub>O<sub>3-δ</sub> compounds were reported to be higher in wet 5H<sub>2</sub>/Ar than in wet air at low temperature. However, the author did not explain this point [16]. Flint *et al.* [15] reported that the grain boundary resistance in oxygen is higher than in nitrogen or hydrogen due to reaction of oxygen with oxide-ion vacancies, and leading to a decrease in oxide ion vacancies available for reaction with water. In this study, we suppose that the GB might be reduced more easily than bulk. In this case, the oxygen released might be compensated by electrons, according to the following equations as:



This would lead to enhanced conduction properties of grain boundary.

Concerning the behaviour at high temperature, we already showed that Y-doped BaSnO<sub>3</sub> present a p-type behaviour at high PO<sub>2</sub>. Then, it is logical that the total conductivities in dry air (**Figure 4.13**) is higher than in dry Ar due to hole conduction. From **Figure 4.12**, it seems that this behaviour is maintained till very low temperature in dry atmosphere. In humid atmosphere the situation is totally different, since the total conductivity is now independent of P(O<sub>2</sub>), confirming that conductivity is dominated by proton charge carriers.

In the following graph, we present the same graph as obtained for BSY5, for the composition  $x = 0.125$  and  $x = 0.25$ . Except for the behaviour in hydrogen, the general conclusions are the same *i.e.* (1) no protons contributions at high temperature but significant hole behaviour in oxidative atmosphere and (2) dominating protonic conductivity at low temperature whatever the humid atmosphere.

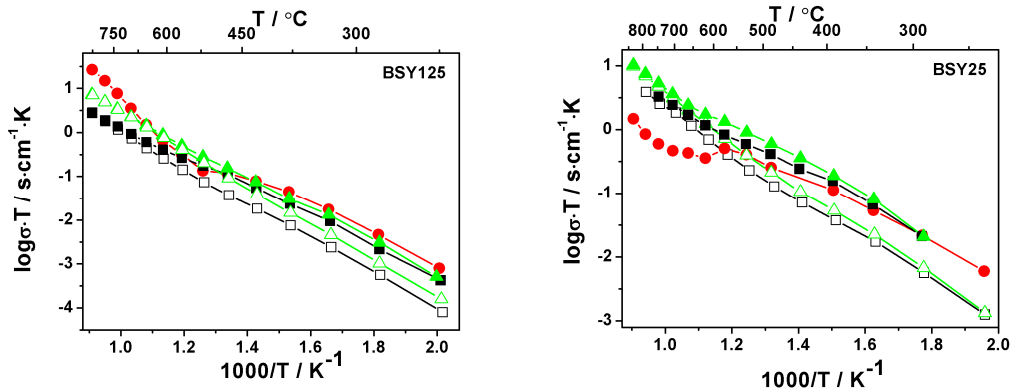


**Figure 4.13** Arrhenius plots of total conductivity of BaSn<sub>1-x</sub>Y<sub>x</sub>O<sub>3-δ</sub> ( $x = 0.125$  and  $0.25$ ) under different atmospheres ( $\square$  - Dry Ar,  $\blacksquare$  - Wet Ar,  $\Delta$  - Dry air,  $\blacktriangle$  - Wet air,  $\bullet$  - Wet 5H<sub>2</sub>/Ar).

#### 4.4.4 Influence of Y<sup>3+</sup> content on conductivity

##### 4.4.4.1 Conductivity in wet and dry Ar atmosphere

The total conductivity, bulk conductivity and grain boundary conductivity of substituted BaSn<sub>1-x</sub>Y<sub>x</sub>O<sub>3-δ</sub> ( $0.05 \leq x \leq 0.375$ ) materials, measured under both dry and wet argon atmospheres, are plotted in **Figure 4.14**. Let us first comment the general trend of these curves as mentioned above. Dry and wet conductivities are the same at high temperature. The total conductivity increases with the Y<sup>3+</sup> content as expected from the increased number of oxygen vacancies with the substitution level. Nevertheless, at high temperature, the total conductivity tends to saturate. Then only slight differences between BSY25 and BSY375 samples are observed. This behaviour is classical in ion conducting compounds for which the conductivity as a function of acceptor doping passes through a maximum value. Another reason might be the slight degradation of BSY375 under wet atmosphere.

In **Table 4.3** are gathered the activation energy in the dry Ar as obtained from the measurements between 600°C and 800°C. These values are smaller than the ones extracted from the fitting presented above for different P(O<sub>2</sub>). This can be explained in part by the fact that the contribution of holes (with smaller activation energy) to the conduction is not negligible in the Ar atmosphere used here. Another explanation is the presence of residual water in the “dry” atmosphere which leads to a non negligible proton contribution. Such

assumption is supported by the fact that conductivity in dry atmosphere also shows a change of slope with decreasing temperature while an Arrhenius like behaviour could be expected. Then, one can hardly associate the activation energy values to a single charge carrier (oxygen vacancies as would be expected) and thus no information can really be extracted from the behaviour in dry atmosphere at low temperature.

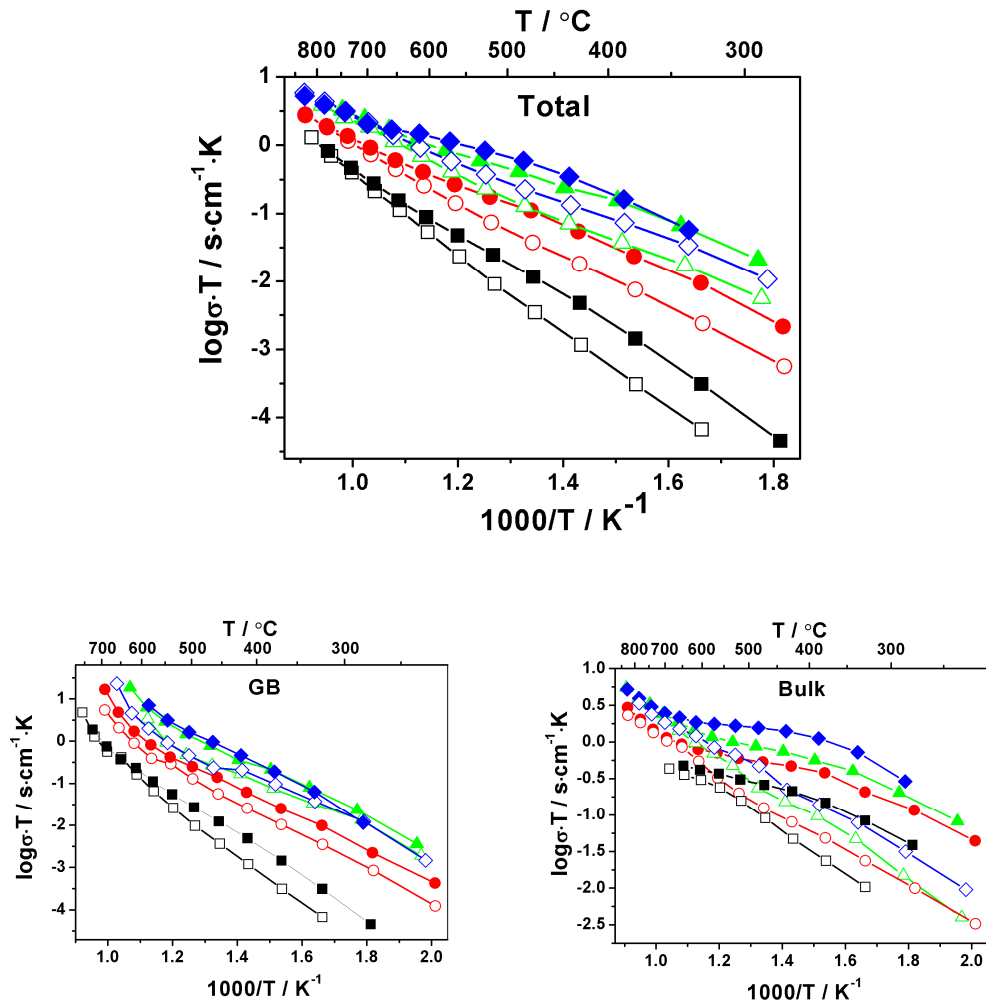


**Figure 4.14** Arrhenius plots of total conductivities of BaSn<sub>1-x</sub>Y<sub>x</sub>O<sub>3-δ</sub> samples under dry (open symbols) and wet (solid symbols) Ar: (a) Total conductivities, (b) Bulk conductivities, (c) Grain boundary conductivities. BSY5 (black squares: □ ■), BSY125 (red circles: ○ ●), BSY25 (up green triangles: ▲ △), BSY375 (blue rhombic: ◆ ◇).

More interesting is the behaviour in wet atmosphere at low temperature. From this low temperature behaviour, one may get quantitative information about proton transport.

The linear behaviour of the logarithm of conductivity versus  $1/T$  is only observed below 400 °C from which the activation energy of the total, bulk and grain boundary proton conductivity can be extracted. These values are reported in **Table 4.4**. The values of activation energy for bulk transport in wet atmosphere at low temperature are around 0.4 eV. These values are smaller than those obtained for Ba<sub>2</sub>SnYO<sub>5.5</sub> (0.51 eV) [1] and Ba<sub>2</sub>SnInO<sub>5.5</sub> (0.56 eV) [17]. According to literature, the activation energy for yttrium-substituted BaZrO<sub>3</sub> was about 0.42 eV - 0.31 eV in the 5 mol % to 15 mol% of Y<sup>3+</sup> on Zr site [18]. Kreuer reported that the activation energy was about 0.44 eV in the Y<sup>3+</sup> concentration range of 2 mol % to 10 mol % and 0.48 eV for BZY20 [5]. These last results for zirconates compounds suggest that the proton transport activation energy is constant at low substituant concentration, and might increase for higher Y<sup>3+</sup> concentration. In this study, we find that the proton activation energy within bulk is constant whatever the yttrium content. Besides the obtained value is in very good agreement with the value (0.36 eV for BaSnHO<sub>3</sub><sup>+</sup>) determined from ab initio calculations [19].

The grain boundary conductivity increases with Y content in the **Figure 4.14**, which has to be related to the grain size of the samples, which was shown also to increase with Y content (shown in **Figure 4.2**). The results for all compositions show that the conductivity is dominated by grain boundary conductivity and that the effect is more evident under wet atmosphere since grain boundary conductivity evolves only slightly with humidity. A similar behaviour exists in most of proton conductors, in particular barium zirconate compounds [4, 20, 21].

Compound	Total Dry (eV)	Bulk Dry (eV)	GB Dry (eV)	Total Wet (eV)	Bulk Wet (eV)	GB Wet (eV)
BSY5	1.21	0.59	1.16	0.98	0.40	1.02
BSY125	0.87	0.48	0.79	0.72	0.38	0.74
BSY25	0.75	0.50	-	0.58	0.35	0.72
BSY375	0.70	0.47	-	0.59	0.36	0.71

Note: the activation energy was attained by fitting Arrhenius plots with the temperature between 600 °C and 800 °C under dry atmosphere. Activation energy of total conductivity was attained between 500 °C and 250 °C, for bulk between 400 °C and 250 °C under wet atmosphere.

**Table 4.4** Activation energy for conduction properties of BSY compounds under Ar atmosphere

#### 4.4.4.2 Conductivity in wet hydrogen atmosphere

The total conductivity under wet 5H<sub>2</sub>/Ar evolves strongly with Y content as synthesised in the Figure 4.15. At high temperature (above 550 °C), for low Y content, the conductivity is almost linear with temperature, while for high Y content, it exhibits weak temperature dependence. For BSY5 sample, the behaviour is monotonic and has been attributed to electron contribution due to an easier reduction of grain boundaries that will control overall conductivity. For the other samples, a transition is evident at an intermediate temperature that corresponds to the temperature at which differences between dry and wet atmospheres are observed. We can thus consider that the conductivity at low temperature in Ar/H<sub>2</sub> humidified atmosphere is essentially protonic in nature. Then, the plateau of conductivities versus temperature for high yttrium content in wet 5H<sub>2</sub>/Ar above 500 °C may be a consequence of an increase in the protonic charge mobility with temperature and a simultaneous decrease in proton concentration due to loss of water [22]. Similar behaviour has also been observed for Ba<sub>3</sub>Ca<sub>1.18</sub>Nb<sub>1.82</sub>O<sub>9-δ</sub> [14] and Ba<sub>0.97</sub>Zr<sub>0.77</sub>Y<sub>0.19</sub>Zn<sub>0.04</sub>O<sub>3-δ</sub> and BaZr<sub>0.8</sub>Y<sub>0.2</sub>O<sub>3-δ</sub> compounds [16]. At high temperature, when samples are no longer hydrated, the main charge carriers are either oxygen vacancies or electrons. The high conductivity observed in BSY5 and BSY125 reflects probably electron contribution to conductivity, while the other compounds are still ion conducting under these conditions. This explanation is coherent with the fact that grain boundaries are

found to be more easily reduced (and higher electron conducting than bulk) and that grain boundaries are more present in compounds with low Y content due to small grain size.

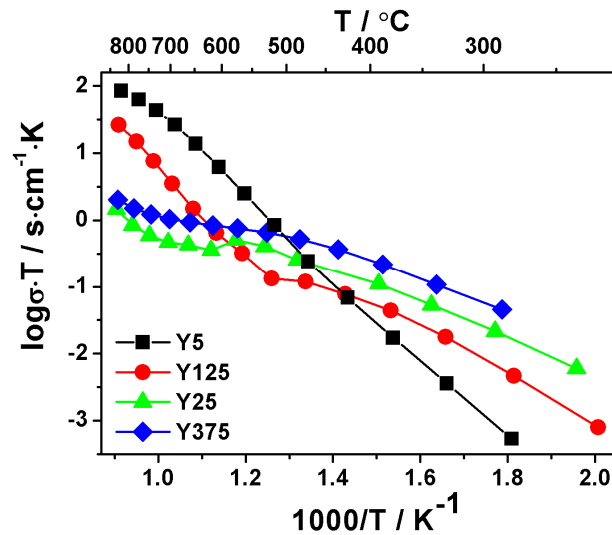


**Figure 4.15** Arrhenius plots of total conductivities of BaSn<sub>1-x</sub>Y<sub>x</sub>O<sub>3-δ</sub> samples in wet 5H<sub>2</sub>/Ar.

#### 4.4.5 Isotope effect

The isotope effect was investigated by comparing a 12.5 mol % Y-doped BaSnO<sub>3</sub> sample under Ar bubbling in H<sub>2</sub>O and D<sub>2</sub>O, see **Figure 4.16**. The slopes of Arrhenius plots at higher temperatures are different from those at low temperatures under Ar with H<sub>2</sub>O and D<sub>2</sub>O. The values of conductivities are found to be the same at high temperatures whatever the atmosphere while the conductivities measured at low temperature in D<sub>2</sub>O-humidified Ar are lower in H<sub>2</sub>O-humidified Ar.

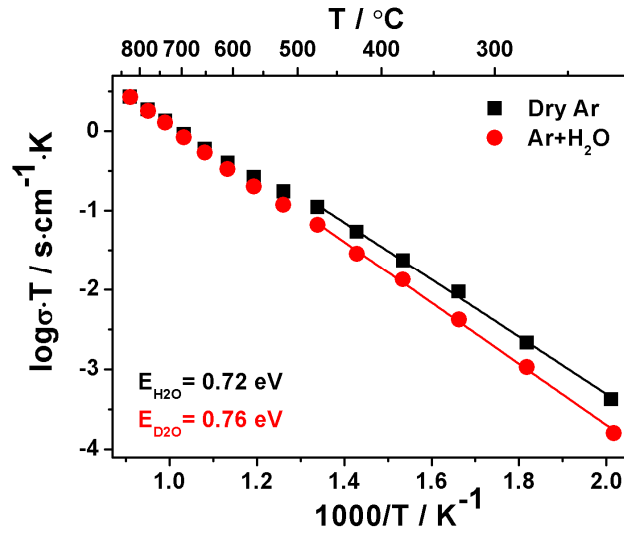


**Figure 4.16** Arrhenius plots of total conductivity plots of 12.5 mol % Y-doped BaSnO<sub>3</sub> under Ar bubbling in H<sub>2</sub>O and D<sub>2</sub>O.

It is well known that the proton does not occupy a true interstitial site but attaches to an oxide ion because of its small size. In a classical approach of particle diffusion, the proton hopping rate is expected to be proportional to  $\sqrt{1/m}$ , which means that the ratio of protonic conductivity to deuteronic conductivity should be  $\sigma_H / \sigma_D = \sqrt{2}$ . However, it shows different results for the ratio of protonic to deuteronic conductivities. For instance, Scherban [23] reported that  $\sigma_H / \sigma_D$  is close to 2.5 in 5 mol % Yb-doped SrCeO<sub>3</sub> compound at room temperature, and concluded that protonic hopping follows a non-classical behavior. However, Huang [24] reported a contrasting result in 6 % Y-doped SrZrO<sub>3</sub>, into which  $\sigma_H / \sigma_D$  is close to  $\sqrt{2}$ , and concluded that protons migrate by hopping in the crystal. In our experiment, **Figure 4.17** shows that the ratio of protonic to deuteronic conductivities increases with decreasing temperature  $\sigma_H / \sigma_D$  is close to  $\sqrt{2}$  at temperature between 600°C and 450°C, and about 2.0 between 450°C and 300°C. In general, the conductivities are determined by the ionic concentration and mobility in crystal. However, we know that some ions may “freeze” in the structure at low temperature, which would lead to different concentrations of protons and deuterons. In this case, the ratio of protonic to deuteronic conductivities will change with temperature.

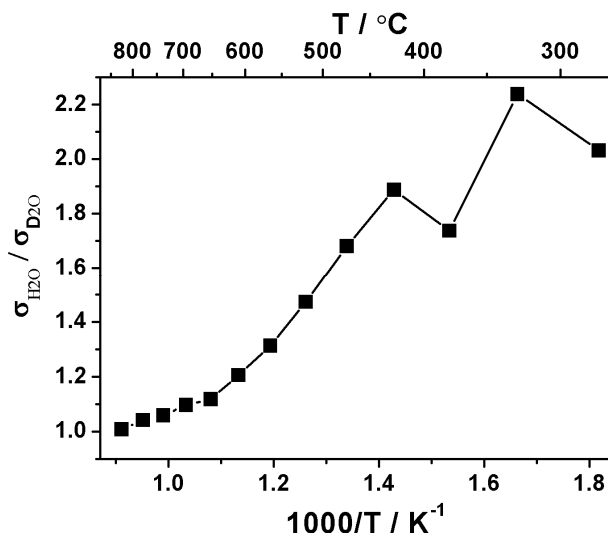


**Figure 4.17** The ratio of conductivity as a function of temperature in Ar bubbling in H<sub>2</sub>O and D<sub>2</sub>O.

The activation energy of sample under D<sub>2</sub>O is 0.04 eV higher than that under H<sub>2</sub>O. The same results have been reported in 5 mol % Yb-doped SrCeO<sub>3</sub> [23] and 6 mol % Y-doped SrZrO<sub>3</sub> [24]. The existence of an isotope effect provides convincing evidence that the conduction mechanism in Y-doped BaSnO<sub>3</sub> is primarily protonic. The conductivity decrease and the activation energy increase when protons are replaced by deuterons.

#### 4.5 Chemical stability

The degradation of conductivity and structural instability of 37.5 mol % Y-doped BaSnO<sub>3</sub> were put into evidence after several measurements under wet atmosphere. A similar behaviour was reported for Ba<sub>2</sub>SnYO<sub>5.5</sub> compounds with the collapse of the structure and the formation of a brownmillerite phase upon reduction, and the macrocracking induced by hydration [1]. In our study, we also observed that Ba<sub>2</sub>SnYO<sub>5.5</sub> compound is not stable. The pellet sintered at 1600°C for 12 h (relative density is > 90 %) was broken when it was in the laboratory atmosphere after some days, and it will be crashed during treated thermally in the air. However, the sample sintered at 1400°C (relative density below 85 %), is stable, even in wet atmosphere, suggesting that porosity helps reducing the effect of the lattice strain resulting from hydration [1]. In order to study the yttrium content dependence on chemical stability in different conditions, we

studied the stability of samples with different yttrium content under different atmospheres, including wet Ar, 5H<sub>2</sub>/Ar and CO<sub>2</sub>, and also in boiling water.

#### 4.5.1 Stability in wet atmospheres/conditions

**Figure 4.18** shows that Y-doped BaSnO<sub>3</sub> powders except 5 mol % Y-doped BaSnO<sub>3</sub> are decomposed completely in boiling water for 3 h, and transformed into BaSn(OH)<sub>6</sub>, Ba(OH)<sub>2</sub>·8H<sub>2</sub>O and Y(OH)<sub>3</sub>. For the same treatment applied to pellets, no other phase is observed. Nevertheless the peaks are wide which indicate a significant effect of hydration on the crystalline structure. For 25 mol % Y-doped BaSnO<sub>3</sub> pellet, **Figure 4.19** shows that no parasitic phase is observed from x-ray diffraction pattern, even after a boiling water treatment of 15 h. However, there is a visible white loose phase on the surface of sample. A SEM observation of a fracture shows clearly this phase till a depth of 10 μm inside the sample (**Figure 4.20**).

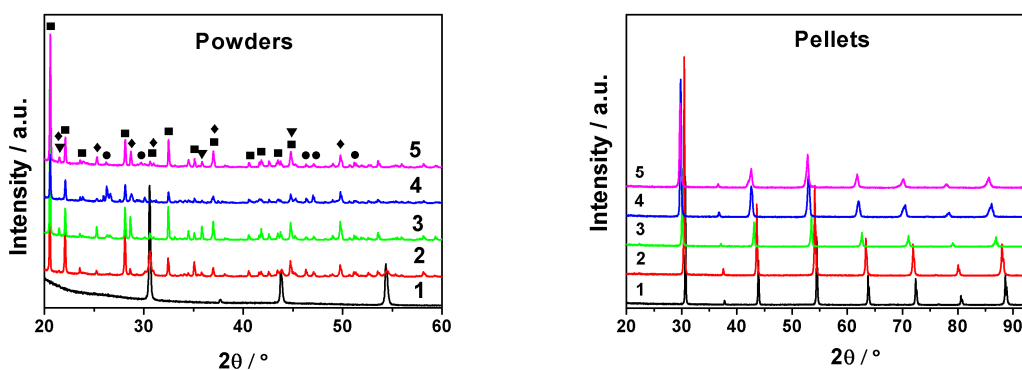


**Figure 4.18** X-ray diffraction of Y-doped BaSnO<sub>3</sub> in boiling water for 3 h: 1 - BSY5, 2 - BSY125, 3 - BSY25, 4 - BSY375, 5 - BSY50.  
(■ - BaSn(OH)<sub>6</sub>, ▼ - Ba(OH)<sub>2</sub>·8H<sub>2</sub>O, ● - Y(OH)<sub>3</sub>, ◆ - BaSnO(OH)<sub>4</sub>)

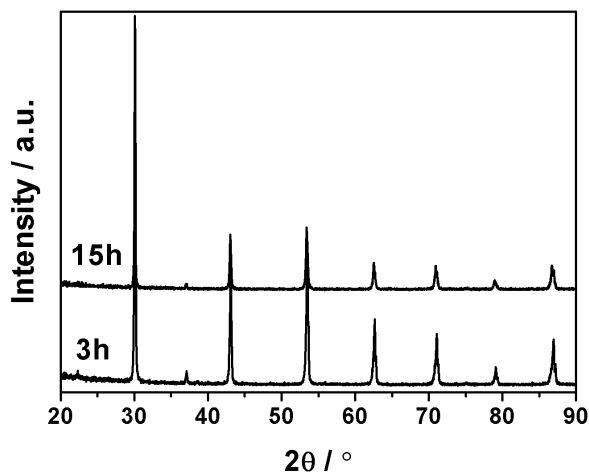


**Figure 4.19** X-ray diffraction of BSY25 pellets in boiling water for different time.

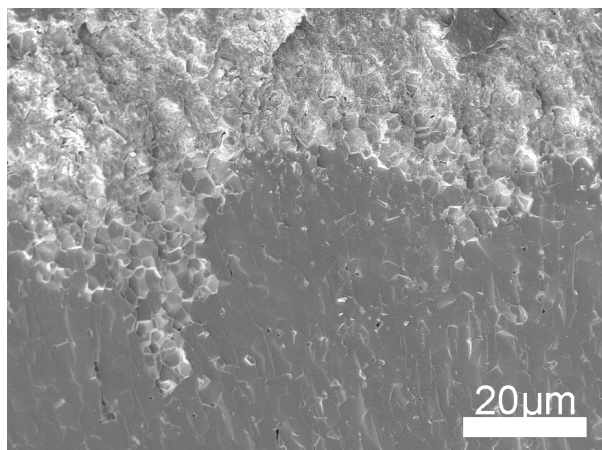


**Figure 4.20** SEM picture of BSY25 pellets in the boiling water for 15 h.

A less aggressive treatment was nevertheless performed consisting in keeping the powder samples at 350 °C for 100 h under wet Ar. **Figure 4.21** shows there is no parasitic phase observed whatever the composition. However, **Figure 4.22** shows that Ba(OH)<sub>2</sub> was formed on the surface of 50 mol % Y doped BaSnO<sub>3</sub> during TG measurement from 1000 °C to room temperature at 0.021 atm. water pressure. For 37.5 mol % Y-doped BaSnO<sub>3</sub>, X-ray diffraction pattern shows small peaks corresponding to pure BaSnO<sub>3</sub>, suggesting the segregation of Y. However, the parasitic phases are only observed on the surface of sample, not observed inside of samples (fracture of sample, and polished) in the **Figure 4.22**.

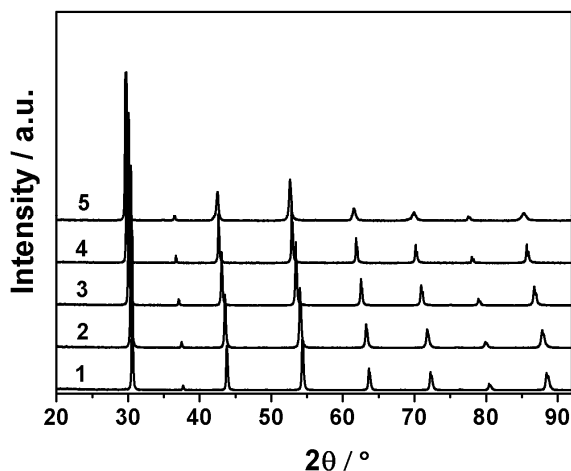


**Figure 4.21** X-ray diffraction patterns of Y-doped BaSnO<sub>3</sub> powders heat-treated in wet Ar at 350°C for 100 h: 1 - BSY5, 2 - BSY125, 3 - BSY25, 4 - BSY375, 5 - BSY50.

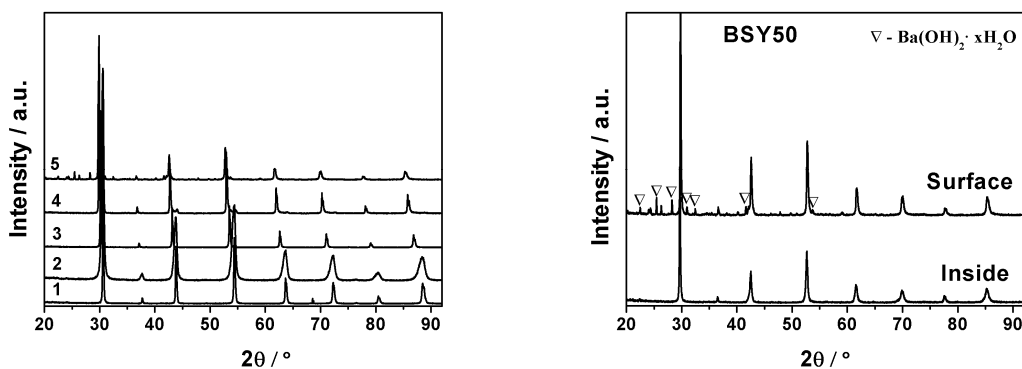
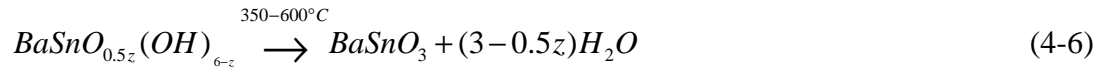


**Figure 4.22** X-ray diffraction patterns of Y-doped BaSnO<sub>3</sub> powders after TG measurement: 1 – BSY5, 2 – BSY125, 3 – BSY25, 4 – BSY375, 5 – BSY50.

The above results show that the stabilities differ significantly between liquid water and water vapour. A similar behaviour has been reported in doped BaCeO<sub>3</sub> by Bhide *et al.* [25]. For barium cerate, the author supposed that water attacks the surface of BaCeO<sub>3</sub> particles and forms barium hydroxide. Barium hydroxide is soluble in water and the remaining insoluble CeO<sub>2</sub> forms a porous layer on the surface of the remaining BaCeO<sub>3</sub>. Water can readily penetrate through the porous CeO<sub>2</sub> interface, and continue the material decomposition. In this study, X-ray diffraction patterns in **Figure 4.18** show peaks correspond with barium hydroxide and barium tin hydroxide respectively. The barium tin

hydroxide will formed barium tin oxide at higher 350°C [26].



In the presence of water vapour, the situation is expected to be different. For proton conductors, oxygen vacancies can be filled by water molecules according to **Eq. (1-2)**. Based on this reaction, it consists of the following steps [27]: 1) chemical absorption of H<sub>2</sub>O on Y-doped BaSnO<sub>3</sub> surface, 2) reaction of H<sub>2</sub>O with O<sup>2-</sup> on the Y-doped BaSnO<sub>3</sub> surface to form hydroxyl ions OH<sup>-</sup>, 3) penetration of OH<sup>-</sup> into the inner part by grain boundary diffusion, 4) filling of oxygen vacancies by OH<sup>-</sup> ions, and therefore the formation of proton defects. In the proton conductors, the oxygen-ion diffusion is much lower than the protonic diffusion. Thus, the oxygen-ion diffusion coefficient would determine the rate of dissolution of water into the perovskite lattice and subsequent kinetics of decomposition. Therefore, the transport of water (liquid) and dissolved Ba(OH)<sub>2</sub> through the porous layer when boiled in water is expected to be much faster than the transport of oxygen ions and proton defect through the lattice. Hence, the kinetics of decomposition in liquid water is then expected to be much faster than in water vapour, which is consistent with the experimental results [25].

One may argue that the treatment of boiling water does not correspond to any of the conditions a material encounters inside a working fuel cell. Nevertheless, this treatment is a very fast and valuable to test the stability of materials in humid atmosphere. Indeed, we tested the same treatment on 10 mol % Y doped barium zirconates and barium cerates. The results show the total degradation of barium cerates powders and pellets, while zirconates pellets are absolutely not degraded and powders only shows small peaks corresponding to Y<sub>2</sub>O<sub>3</sub>. We thus consider this test to give relevant information on the stability of material for the foreseen fuel cells application.

The stability of the perovskite structure has often been rationalized in terms of the radii of ions comprising the unit cell using a parameter known as the Goldschmidt tolerance factor, *t*, which is defined [28]:

$$t = \frac{r_A + r_o}{\sqrt{2}(r_B + r_o)} \quad (4-7)$$

Where,  $r_A$ ,  $r_B$  and  $r_o$  are the ionic radii of A, B, and O ions, respectively. Kreuer [29] have reported that the perovskite oxide with big B ion exhibits low tolerance factor and low thermodynamics stabilisation with respect to the binary oxides, and the closer the  $t$  is to unity, the greater is the expected stability of the perovskite structure [28]. Bhide *et al.* [28] reported that the Madelung energy (a negative energy quantity) is inversely proportional to the lattice parameter for the  $A^{2+}B^{4+}O_3$  perovskite. From this argument, the stability of perovskite oxide decreases thus with the increase of cell parameters. Then, the tolerance factors is anticipated to decrease with yttrium content, and the Madelung energy is anticipated to have smaller absolute values with yttrium content due to both the diminishing of formal charge and to the increase of cell parameters. This qualitative argument helps thus understanding why the instability of Y-doped compounds diminishes with yttrium content. Another possibility is that the greater content of oxygen vacancies with yttrium makes the strain induced by humidification much more important for higher yttrium contents.

#### 4.5.2 Stability in wet 5H<sub>2</sub>/Ar and CO<sub>2</sub>

BSY25 and BSY50 powders (calcined at 1400°C for 10 h) and pellets (sintered at 1500 °C for 12 h) were treated thermally at 600 °C for 50 h under wet 5H<sub>2</sub>/Ar and 650 °C for 50 h under wet CO<sub>2</sub>. The X-ray diffraction patterns are shown in **Figure 4.23** and **Figure 4.24**, respectively. There is no impurity observed for the samples treated under wet H<sub>2</sub> and CO<sub>2</sub>. Y-doped BaSnO<sub>3</sub> seem stable under CO<sub>2</sub> atmosphere in accordance with the result previously published on Ba<sub>2</sub>SnYO<sub>5.5</sub> [1]. However, it was reported Ba<sub>2</sub>SnYO<sub>5.5</sub> formed the brownmillerite phase upon reduction atmosphere. In our study, we have not observed this phase from samples treated in wet 5H<sub>2</sub>/Ar.

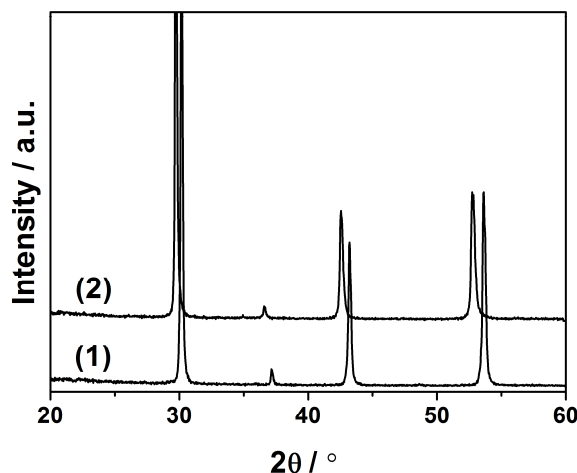


**Figure 4.23** X-ray diffractions of (1) BSY25 and (2) BSY50 pellets sintered at 1500°C for 12 h in wet 5H<sub>2</sub>/Ar at 600°C for 50 h.

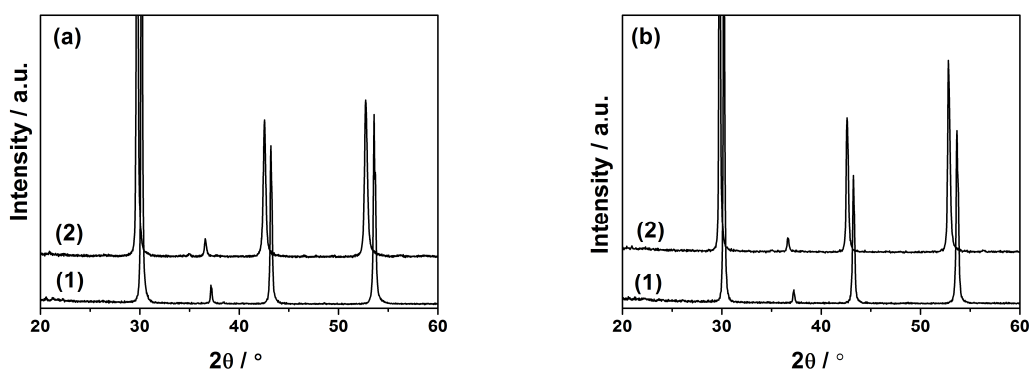


**Figure 4.24** X-ray diffractions of (1) BSY25 and (2) BSY50 in wet CO<sub>2</sub> at 650°C for 50 h.  
(a) Powders and (b) Pellets

## 4.6 Conclusion

We have succeeded in synthesising BaSn<sub>1-x</sub>Y<sub>x</sub>O<sub>3-d</sub> dense compounds with a polymerisation route followed by a classical sintering. All materials present a cubic perovskite structure with cell parameters following the evolution of mean radius on B-site. All compounds uptake water at low temperature and thermogravimetric measurements indicate a decrease in hydration enthalpy as yttrium content increases. All doped compounds are oxygen ion conducting at high temperature and present a mixed anion-hole behaviour in the range 10<sup>-5</sup>-1 atm of oxygen partial pressure. Activation energies have

been determined for both charge carriers and are shown to diminish with yttrium content. The best anion conduction properties are observed for higher yttrium contents showing that mobility does not evolve as much as oxygen vacancy concentration with yttrium doping. At low temperature, proton conduction is observed in humid atmosphere for all compounds. The level of proton conduction follows that of oxygen conduction i.e. the higher the doping level the higher the proton conductivity. From the analysis of bulk and GB conductivity, we determined that this evolution is in great part due to difference of microstructures between the samples. Indeed, the bulk conduction increases strongly in humid atmosphere while it increases only slightly for GBs. Smaller grain size samples will thus present poor proton conduction. Activation energies for bulk proton conduction changes slightly with Y content between 0.35 eV - 0.40 eV, a value close to that observed for barium zirconates.

The stability of Y-doped BaSnO<sub>3</sub> was investigated under different atmospheres and conditions. Under CO<sub>2</sub>, the Y-doped compounds are stable, and there is no imperious phase observed by XRD. However, the conductivity of 37.5 mol % Y-doped barium stannate degraded after several measurements, which resulted in the collapse of the structure. For low yttrium content, we have not observed the degradation of conductivities neither the appearance of parasitic phase in the sample treated in humidified and highly reducing atmosphere. This would mean that the instability of barium stannate compounds is not as important as expected, and is probably due essentially to hydration induced stress.

## References

- [1] P. Murugaraj, K. D. Kreuer, T. He, T. Schober, J. Maier, *Solid State Ionics* **1997**, 98, 1.
- [2] R. D. Shannon, *Acta Cryst.* **1976**, A32, 751.
- [3] J. Wu, L. P. Li, a. S. M. H. W. T. P. Espinosa, *J. Mat. Res.* **2004**, 2366.
- [4] K. D. Kreuer, *Ann. Rev. Mater. Res.* **2003**, 33, 333.
- [5] K. D. Kreuer, S. Adams, W. Munch, A. Fuchs, U. Klock, J. Maier, *Solid State Ionics* **2001**, 145, 295.
- [6] Y. Yamazaki, P. Babilo, S. M. Haile, *Chemistry of Materials* **2008**, 20, 6352.
- [7] K. D. Kreuer, *Solid State Ionics* **1999**, 125, 285.
- [8] B. Ostrick, M. Fleischer, H. Meixner, *Journal of the American Ceramic Society* **1997**, 80, 2153.
- [9] W. Lu, S. Jiang, D. Zhou, S. Gong, *Sensors and Actuators A: Physical* **2000**, 80, 35.
- [10] I. Kosacki, H. L. Tuller, *Solid State Ionics* **1995**, 80, 223.
- [11] I. Ahmed, S.-G. Eriksson, E. Ahlberg, C. S. Knee, *Solid State Ionics* **2008**, 179, 1155.
- [12] I. Ahmed, C. S. Knee, M. Karlsson, S. G. Eriksson, P. F. Henry, A. Matic, D. Engberg, L. Borjesson, *Journal of Alloys and Compounds* **2008**, 450, 103.
- [13] S. Valkenberg, H. G. Bohn, W. Schilling, *Solid State Ionics* **1997**, 97, 511.
- [14] H. G. Bohn, T. Schober, T. Mono, W. Schilling, *Solid State Ionics* **1999**, 117, 219.
- [15] S. D. Flint, R. C. T. Slade, *Solid State Ionics* **1997**, 97, 457.
- [16] S. Tao, J. T. S. Irvine, *Journal of Solid State Chemistry* **2007**, 180, 3493.
- [17] T. Schober, *Solid State Ionics* **1998**, 109, 1.
- [18] F. Iguchi, N. Sata, T. Tsurui, H. Yugami, *Solid State Ionics* **2007**, 178, 691.
- [19] E. Bevilion, PhD thesis, SPMS laboratory of Ecole Centrale Paris, **2009**.
- [20] F. Iguchi, T. Tsurui, N. Sata, Y. Nagao, H. Yugami, *Solid State Ionics* **2009**, 180, 563.
- [21] F. Iguchi, T. Yamada, N. Sata, T. Tsurui, H. Yugami, *Solid State Ionics* **2006**, 177, 2381.
- [22] N. Bonanos, *Solid State Ionics* **1992**, 53-56, 967.

- [23] T. Scherban, W. K. Lee, A. S. Nowick, *Solid State Ionics* **1988**, 28-30, 585.
- [24] H. H. Huang, M. Ishigame, S. Shin, *Solid State Ionics* **1991**, 47, 251.
- [25] S. V. Bhide, A. V. Virkar, *Journal of The Electrochemical Society* **1999**, 146, 2038.
- [26] H. S. Wensheng Lu, *J Sol-Gel Sci Techn* **2007**, 42.
- [27] X. Guo, *Chemistry of Materials* **2004**, 16, 3988.
- [28] S. V. Bhide, A. V. Virkar, *Journal of The Electrochemical Society* **1999**, 146, 4386.
- [29] K. D. Kreuer, *Solid State Ionics* **1997**, 97, 1.

# Chapter 5 Effect of ZnO Additive on Sintering and Electrical Properties of $\text{BaSn}_{0.75}\text{Y}_{0.25}\text{O}_{3-\delta}$

## 5.1 Introduction

$\text{BaSn}_{0.75}\text{Y}_{0.25}\text{O}_{3-\delta}$  compounds have shown high proton conductivity and rather good stability under wet atmospheres in chapter 4. However, they exhibit a strong aversion against densification. For instance, the relative density is only about 90 % for samples sintered at 1600°C for 12 h. Such a high temperature possibly results in barium evaporation and leads to the decrease of proton conductivity. A high temperature also makes difficult to fabricate an effective electrochemical device using this oxide. Indeed, it is difficult to find good electrode materials which can sustain a so high temperature without significant chemical reactions. It is also impossible to retain the porous microstructure of the electrode at such temperature.

Recently, both Haile's and Irvine's groups have reported that ZnO as an additive or a second dopant can favour a high densification at low sintering temperature (1300-1350°C), and can strengthen the chemical stability, even if this slightly decreases the total conductivity [1-5]. The results reported are nevertheless contradictory concerning zinc position in the materials. Babilo *et al.* [2] reported that Zn accumulates in the intergranular regions as observed by SEM and energy dispersive X-ray spectroscopy (EDS), while Tao *et al.* [4] reported that zinc enters the lattice structure from both EDS and XRD analyses after firing.

The aim of this chapter is to verify that the positive effect of ZnO addition on densification of barium stannates can also be applied for barium stannates. In order to investigate the effect of ZnO additive on the formation of single phase, densification and electrical properties, we have employed two methods for introducing ZnO into the

materials, and investigated the effect of ZnO on the aforementioned properties by a combined approach of XRD, SEM/EDS and AC impedance spectroscopy (IS).

This chapter consists of two parts. Part I: the effect of ZnO on the pure phase formation and densification of  $\text{BaSn}_{0.75}\text{Y}_{0.25}\text{O}_{3-\delta}$  compound. Part II: the effect of ZnO as a sintering aid and second dopant on the electrical properties of  $\text{BaSn}_{0.75}\text{Y}_{0.25}\text{O}_{3-\delta}$ .

## **5.2 Part I: ZnO effect on pure phase formation and densification of $\text{BaSn}_{0.75}\text{Y}_{0.25}\text{O}_{3-\delta}$**

### **5.2.1 Experimental**

Polycrystalline barium stannate based compounds were prepared by a solid state reaction method. Starting materials were high purity  $\text{BaCO}_3$  (Alfa Aesar, 99.9-101 %),  $\text{SnO}_2$  (Alfa, 99.9 %),  $\text{Y}_2\text{O}_3$  (Rhône-Poulenc, 99.999 %) and ZnO (Fluka Chemie, > 99 %). First,  $\text{BaCO}_3$  powders were dried at 120 °C in the oven, and  $\text{SnO}_2$ ,  $\text{Y}_2\text{O}_3$  and ZnO powders were calcined at 800 °C for 2 h before mixing together. Stoichiometric amounts of  $\text{BaCO}_3$ ,  $\text{SnO}_2$ ,  $\text{Y}_2\text{O}_3$  and ZnO were mixed initially in a mortar by hand. Acetone was added during the milling to ensure thorough mixing. Subsequently, the mixtures were milled in a  $\text{ZrO}_2$  container with  $\text{ZrO}_2$  balls (Retsch, PM100) at 450 rpm for 12 h.

For investigating the effect of ZnO as a sintering aid on the densification of  $\text{BaSn}_{0.75}\text{Y}_{0.25}\text{O}_{3-\delta}$  compound, the milled mixture of stoichiometric amounts of  $\text{BaCO}_3$ ,  $\text{SnO}_2$  and  $\text{Y}_2\text{O}_3$ , was calcined 1400°C for 10 h to obtain pure  $\text{BaSn}_{0.75}\text{Y}_{0.25}\text{O}_{3-\delta}$  powder. The calcined powders were mixed with given quantities of ZnO, and pressed into 10mm pellets by uniaxial pre-pressing in a steel die under 4 t pressure for 1 min, and then isostatically pressed at 750 MPa during 10 min (green densities ~ 60-70%). Thereafter, the as-pressed pellets were sintered at 1300°C, 1400°C and 1500°C for 12 h. The heating rate was 300 °C/h, and cooling rate 400 °C/h.

The relative densities of sintered pellets were determined by measuring the dimensions and weight of each sample. Total linear shrinkage  $(L-L_0)/L_0$  was used to

characterise the effect of the content of ZnO additive on the sinterability of the BSY25, where  $L_0$  is the initial diameter and  $L$  is the final diameter.

## 5.2.2 Results and discussions

### 5.2.2.1 Single-phase formation with ZnO

Many methods have been developed to prepared barium stannate based materials, including conventional solid state reaction [6] and wet chemical methods [7-10]. However, doped  $\text{BaSnO}_3$  compounds are mostly prepared by solid state reaction [11-14] due to its features of simplicity. It is known that this method supposes high temperature for attaining single phase. The single-phase formation of doped  $\text{BaSnO}_3$  compound supposes a calcination temperature above  $1300^\circ\text{C}$ , and generally needs intermediate grinding.

In order to investigate the effect ZnO on the formation of pure phase  $\text{BaSn}_{0.75}\text{Y}_{0.25}\text{O}_{3-\delta}$  compound, we added 4 mol % ZnO into the stoichiometric mixtures of oxide/carbonate measured for the  $\text{BaSn}_{0.75}\text{Y}_{0.25}\text{O}_{3-\delta}$  target compound. The mixtures were calcined between  $950^\circ\text{C}$  and  $1400^\circ\text{C}$ . The value of 4 mol % ZnO was the one used previously by Babilo *et al.* [2] for  $\text{BaZrO}_3$  compound. We will see in the next paragraph that this value also corresponds to the optimised value for  $\text{BaSn}_{0.75}\text{Y}_{0.25}\text{O}_{3-\delta}$  densification.

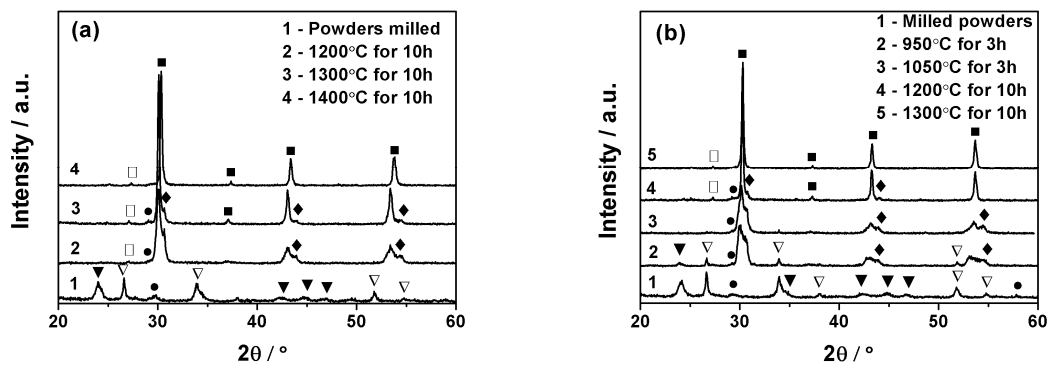


**Figure 5.1** X-ray diffraction patterns of powders calcined at different temperature: (a)  $\text{BaSn}_{0.75}\text{Y}_{0.25}\text{O}_{3-\delta}$ , (b)  $\text{BaSn}_{0.75}\text{Y}_{0.25}\text{O}_{3-\delta}$  with 4 mol % ZnO additive.  
 (● -  $\text{Y}_2\text{O}_3$ , ◆ -  $\text{BaSnO}_3$ , ■ -  $\text{BaSn}_{0.75}\text{Y}_{0.25}\text{O}_{3-\delta}$ , ▼ -  $\text{BaCO}_3$ , ▽ -  $\text{SnO}_2$ , □ -  $\text{K}_\beta$ ).

X-ray diffraction patterns are presented in **Figure 5.1**. After ball milling, there is no new phase formed in the raw powders, however the peaks become wide. This indicates that the grain size of powders becomes smaller after milling, and this might be favourable to sintering and reaction. **Figure 5.1 (a)** shows that pure  $\text{BaSn}_{0.75}\text{Y}_{0.25}\text{O}_{3-\delta}$  compound is obtained after heat-treatment at  $1400^\circ\text{C}$ . The possible phases are identified using program Eva, and they are  $\text{Y}_2\text{O}_3$ ,  $\text{BaSnO}_3$ ,  $\text{BaSn}_{0.75}\text{Y}_{0.25}\text{O}_{3-\delta}$  and  $\text{K}_\beta$  below  $1400^\circ\text{C}$ . With ZnO additive, **Figure 5.2 (b)**, the single phase of  $\text{BaSn}_{0.75}\text{Y}_{0.25}\text{O}_{3-\delta}$  compound is obtained at  $1300^\circ\text{C}$ , which is about  $100^\circ\text{C}$  lower than  $\text{BaSn}_{0.75}\text{Y}_{0.25}\text{O}_{3-\delta}$  without ZnO. A similar behaviour was shown in the compound  $\text{BaZr}_{0.8}\text{Y}_{0.2}\text{O}_{3-\delta}$ , for which the single phase preparation temperature with ZnO is roughly  $350^\circ\text{C}$  lower than that required for pure  $\text{BaZr}_{0.8}\text{Y}_{0.2}\text{O}_{3-\delta}$  [4].

#### 5.2.2.2 Densification with ZnO

To investigate the effect of ZnO content on the densification behaviour of  $\text{BaSn}_{0.75}\text{Y}_{0.25}\text{O}_{3-\delta}$  compound, we first prepared single-phase  $\text{BaSn}_{0.75}\text{Y}_{0.25}\text{O}_{3-\delta}$  at  $1400^\circ\text{C}$ , which was identified by X-ray diffraction (**Figure 5.1**). The linear shrinkage of  $\text{BaSn}_{0.75}\text{Y}_{0.25}\text{O}_{3-\delta}$  compound with different ZnO (0-10 mol %) content is presented in **Figure 5.2**. We use the linear shrinkage for comparing the densification of different additions of ZnO since the theoretical density of samples will change with ZnO content.

**Figure 5.2** shows that the linear shrinkage, increases in the range from 0-4 mol % ZnO, and then almost remains constant value for higher ZnO contents. This behaviour is similar to the case of ZnO as an additive in  $\text{BaZr}_{0.8}\text{Y}_{0.2}\text{O}_{3-\delta}$ , and it was reported that a maximum density as a function of sintering temperature exists at  $1300^\circ\text{C}$  [2]. In this study, we find that the densification at  $1400^\circ\text{C}$  is slightly higher than at  $1300^\circ\text{C}$  and  $1500^\circ\text{C}$ .

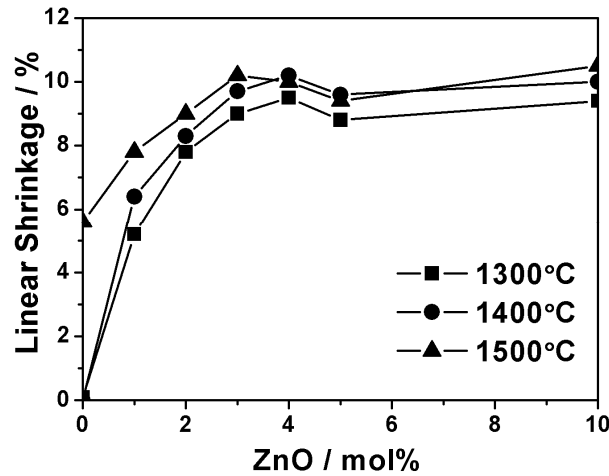


**Figure 5.2** The linear shrinkage of  $\text{BaSn}_{0.75}\text{Y}_{0.25}\text{O}_{3-\delta}$  with different ZnO contents as a sintering aid sintered at different temperatures.

### 5.2.3 Conclusion

With the use of 4 mol % ZnO as a sintering aid, we can increase significantly the density of  $\text{BaSn}_{0.75}\text{Y}_{0.25}\text{O}_{3-\delta}$  at low temperature, and decrease the temperature of the formation of single phase  $\text{BaSn}_{0.75}\text{Y}_{0.25}\text{O}_{3-\delta}$  prepared by solid state reaction.

The question now remains about the role played by ZnO and its influence on transport properties. This will be studied in the next part, during which we will examine ZnO both as a sintering aid and a second dopant.

## 5.3 Part II: ZnO as a sintering aid and second dopant effects on microstructural and electrical properties of $\text{BaSn}_{0.75}\text{Y}_{0.25}\text{O}_{3-\delta}$ compound

### 5.3.1 Experimental

For ZnO as a second dopant, we studied the composition of  $\text{BaSn}_{0.71}\text{Y}_{0.25}\text{Zn}_{0.04}\text{O}_{3-\delta}$  (denoted BSY25Zn4). The mixtures of  $\text{BaCO}_3$ ,  $\text{SnO}_2$ ,  $\text{Y}_2\text{O}_3$  and ZnO in stoichiometric ratio were milled in a  $\text{ZrO}_2$  container with  $\text{ZrO}_2$  balls (Retsch, PM100) at 450 rpm for 12 h. For ZnO as a sintering aid (denoted BSY25-4ZnO), we used pure  $\text{BaSn}_{0.75}\text{Y}_{0.25}\text{O}_{3-\delta}$  powders initially prepared at  $1400^\circ\text{C}$  for 10 h, and mixed with 4 mol % ZnO and

performed a ball milling at 400 rpm for 2 h. After shaping the sintering process consisted of a thermal treatment at 1300-1400°C during 12 h.

## 5.3.2 Results and discussions

### 5.3.2.1 Structural and microstructural properties

The diffraction patterns of sintered pellets obtained are presented in **Figure 5.3**. In all cases, a single phase cubic structure is observed (space group:  $Pm\bar{3}m$ ). The lattice parameters were refined using the Topas and cellref programs, and the relative density was calculated by dimensions and weight (see in **Table 5.1**). ZnO both as a sintering aid and second dopant can increase significantly the density of samples at 1300 °C. Babilo *et al.* [2] reported that the enhanced densification is assumed to be a result of the high Zn concentration in the grain-boundary regions, and suggested that Zn entering the bulk crystalline structure would induce a decrease of densification. In contrast, Tao *et al.* [4] suggested that ZnO reacts with barium oxides to form intermediate barium zinc oxides with relative lower melting point decreasing the sintering temperature. Another possibility is that zinc enters the perovskite lattice and the Zn-containing perovskite exhibits a lower melting point, which further leads to denser samples. In this study, the comparison of the two methods, suggests that both mechanism may exist for enhanced densification with zinc oxide. Both Zn in the grain boundary and in the bulk will enhance the densification.

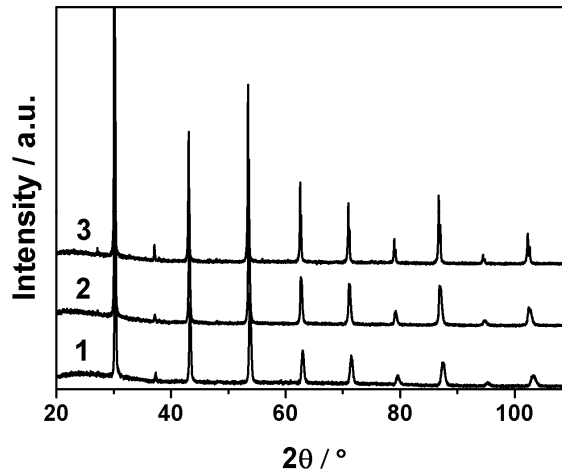


**Figure 5.3** X-Ray diffraction patterns of sintered pellets: 1 - BSY25 sintered at 1600°C, 2 - BSY25-4ZnO sintered at 1300°C, 3 - BSY25Zn4 at 1300°C for 12 h.

Compounds	Sintering condition (°C)	Lattice Parameter $a(\text{Å})$	Relative density (%)
BSY25 powder	1400	4.1963(3)	-
BSY25 pellet	1600	4.1680(7)	94-97
BSY25-4ZnO	1300	4.1892(8)	96-98
BSY25Zn4	1300	4.197(8)	97-99

*Note: The theoretical theory density value used was calculated by using the lattice parameter of BSY25 powders calcined at 1400°C for 10 h.*

**Table 5.1** the lattice parameters and relative densification of compounds

From **Table 5.1**, the cell parameters for the four samples can be classified according to:  $a$  (BSY25Zn4) >  $a$  (BSY25 powder) >  $a$  (BSY25-4ZnO) >  $a$  (BSY25 pellet). The interpretation for such result is not obvious though some explanations can be found from the composition of compounds and from the thermal treatment they were submitted to. First of all, the ionic radius of  $Zn^{2+}$  in 6-fold coordination (0.72Å) is slightly higher than that of  $Sn^{4+}$  (0.69Å, six-coordination [15]). A slight increase of cell parameter might thus be expected if Zn substitutes for Sn. More drastic, will be the evolution due to barium evaporation during thermal treatment. In this case, an important decrease of cell parameter

is expected if significant amount of barium is lost during high temperature sintering [16]. These two points allow explaining the evolution in the series:  $a$  (BSY25Zn4) >  $a$  (BSY25 powder) >  $a$  (BSY25 pellet).

For BSY25-4ZnO, nevertheless, some zinc entering inside the structure can not be discarded. In this case, the real formula of the compound should probably be written:  $Ba_{1-x}(Sn_{0.75}Y_{0.25})_{1-x}Zn_xO_{3-d}$  with  $x$  not exceeding 4 mol % corresponding to the case of a total incorporation of zinc addition inside the perovskite structure. In this case, more than the influence of zinc on the mean radius of B-site, the consequence of this incorporation is an induced sub-stoichiometry on A-site leading to a smaller cell parameter as observed when barium evaporation is considered. Indeed, if zinc goes to the B-sites on firing, which could be expected to increase the vacancy concentrations on both the Ba and oxygen sites according to [2]:



The increase in barium vacancy concentration is also responsible for the decrease in lattice parameters of BSY25-4ZnO comparing with pure BSY25. It was also reported to be responsible for the increase of grain-boundary mobility, grain growth and densification[2].

The microstructure of sintered pellets is shown in **Figure 5.4-5.6**. **Figure 5.4** illustrates the microstructure of samples with ZnO as a second dopant as a function of sintering temperature. The grain size grows obviously with increasing the temperature, from 1-2  $\mu m$  at 1300°C to 3-4  $\mu m$  at 1350°C, and the grain shows a rough surface at 1400°C, which may be due to the evaporation of Zn. A similar behaviour has been reported in the  $BaZr_{0.85}Y_{0.15}O_{3-\delta}$  with 4 mol % ZnO as additive [2]. The SEM pictures of BSY25-4ZnO (*i.e.* ZnO as a sintering aid) are presented in **Figure 5.6**, with EDS analyses. EDS patterns show that the small grain (point 1) exhibits stronger peaks corresponding to Zn element, while the big grain (point 2) exhibits very small peaks for Zn element, and the other small grains in grain boundary also contains Zn element. This result is in agreement

with the chemical analysis of Y-doped  $BaZrO_3$  with 4 mol % ZnO additive [2]. The average grain size of unmodified BSY25 sintered at  $1600^\circ\text{C}$  (Figure 5.5) is about 1-2  $\mu\text{m}$ , which is close to that of BSY25Zn4 compound sintered at  $1300^\circ\text{C}$ . Caballero *et al.* [17] observed that introduction of very small concentrations of ZnO to  $BaTiO_3$  dramatically inhibited grain growth. In contrast, it was reported that the grain size of Y-doped  $BaZrO_3$  with 4 mol % ZnO is higher than that of simple Y-doped  $BaZrO_3$  for samples sintered at  $1300^\circ\text{C}$  [2]. Hence, considering the great difference of temperature between the two treatments, we can consider that ZnO favours grain growth.

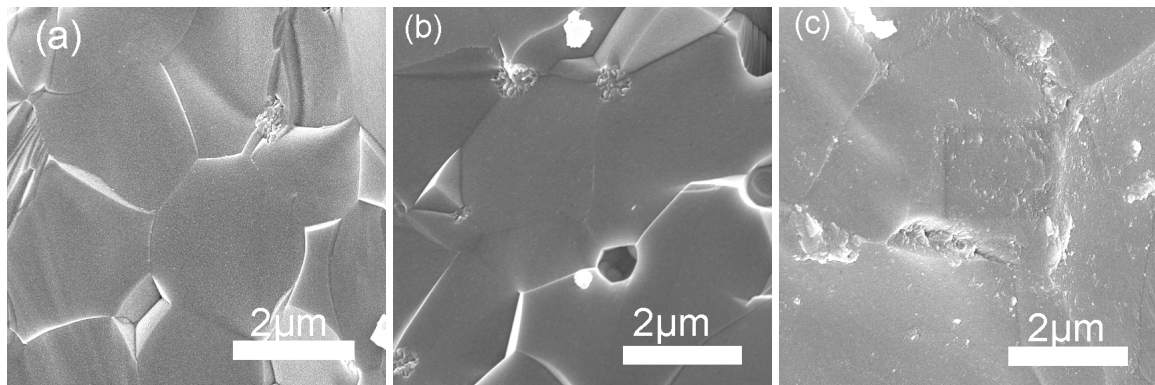


**Figure 5.4** SEM picture of BSY25Zn4 sintered at different temperature: (a)  $1300^\circ\text{C}$  for 12 h, (b)  $1350^\circ\text{C}$  for 12 h, (c)  $1400^\circ\text{C}$  for 12 h.

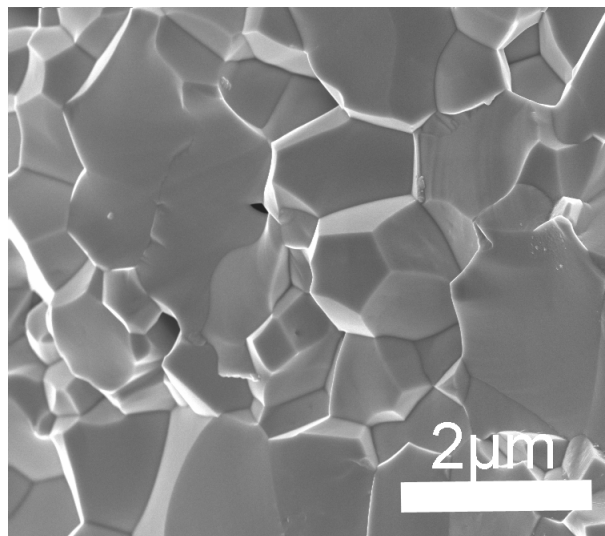


**Figure 5.5** SEM of BSY25 sintered at  $1600^\circ\text{C}$  for 12 h

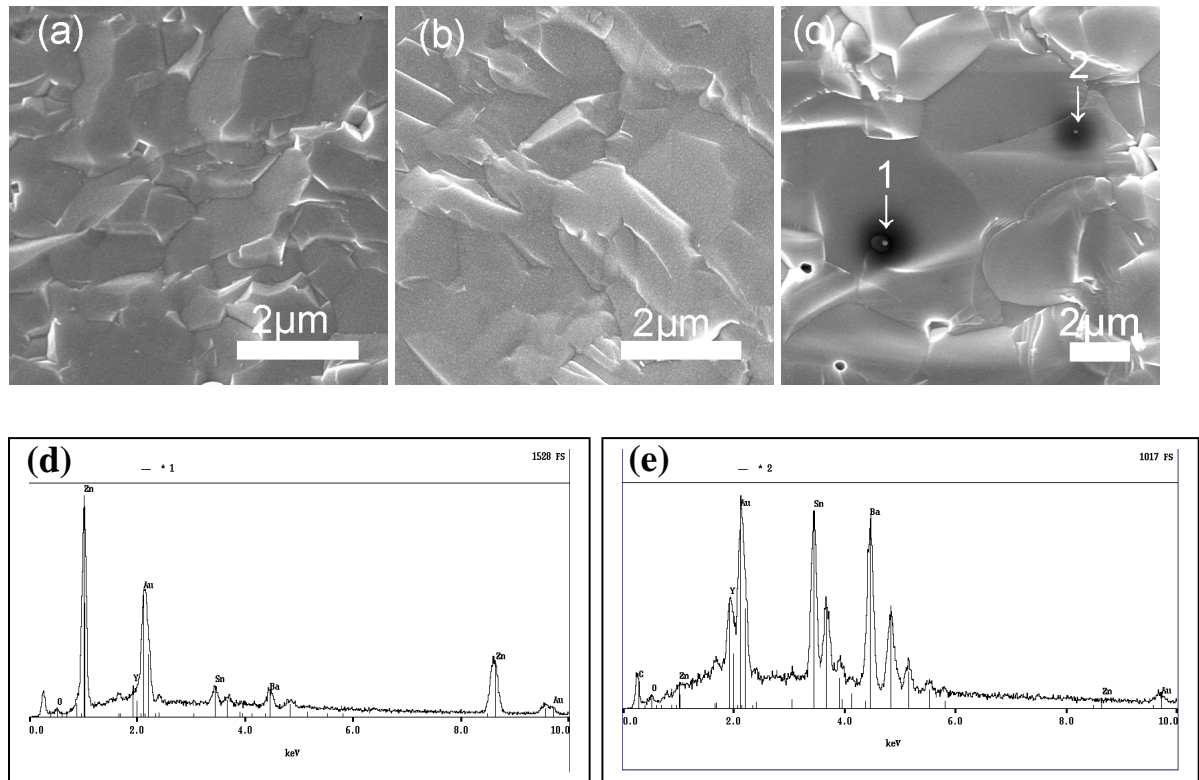


**Figure 5.6** SEM of BSY25-4ZnO compounds: (a) 1300°C, (b) 1350°C, (c) 1400°C for 12 h; EDS: (d) point 1, (e) point 2 in SEM of (c).

### 5.3.2.2 Transport properties

The evolution of the Nyquist plots of BSY25-4ZnO obtained at low temperature under dry and wet air atmospheres is shown in **Figure 5.7**. The other compounds have similar impedance spectra. Therefore we only present the impedance spectra of BSY25-4ZnO. At low temperature, the impedance spectra showed the impedance of sample in wet air diminished dramatically comparing with in dry air due to proton conduction. Below 300°C, the impedance spectra consisted of three full semicircles. The higher frequency arc is attributed to bulk response, low frequency arc is attributed to electrode response (see below), and the semicircle between the bulk and electrode arcs is attributed to grain boundary response. With increasing temperature, the arcs shift to high frequencies and for  $T > 300^\circ\text{C}$ , the impedance spectra consist of the grain boundary arc, electrode arc and Warburg diffusion. The frequency arc corresponding to bulk reaches a value higher than the maximum measurement frequency of the impedance meter and thus the bulk arc is no

longer visible in this case. ( $> 380^\circ\text{C}$ ). In order to indentify the semi-circle in the frequency between  $10^4$  Hz and 1Hz, we measured a full impedance spectrum with the bias of 0.2 V. **Figure 5.7** shows that this semi-circle changes with bias, suggesting that it can be associated to electrode contribution not to our material.

In order to separate the bulk and grain boundary resistance, impedance spectra were modeled using an equivalent electrical circuit formed with three  $R_iC_i$  circuits in series at low temperature ( $< 300^\circ\text{C}$ ), and the series association of a resistance and two  $R_iC_i$  at high temperature.

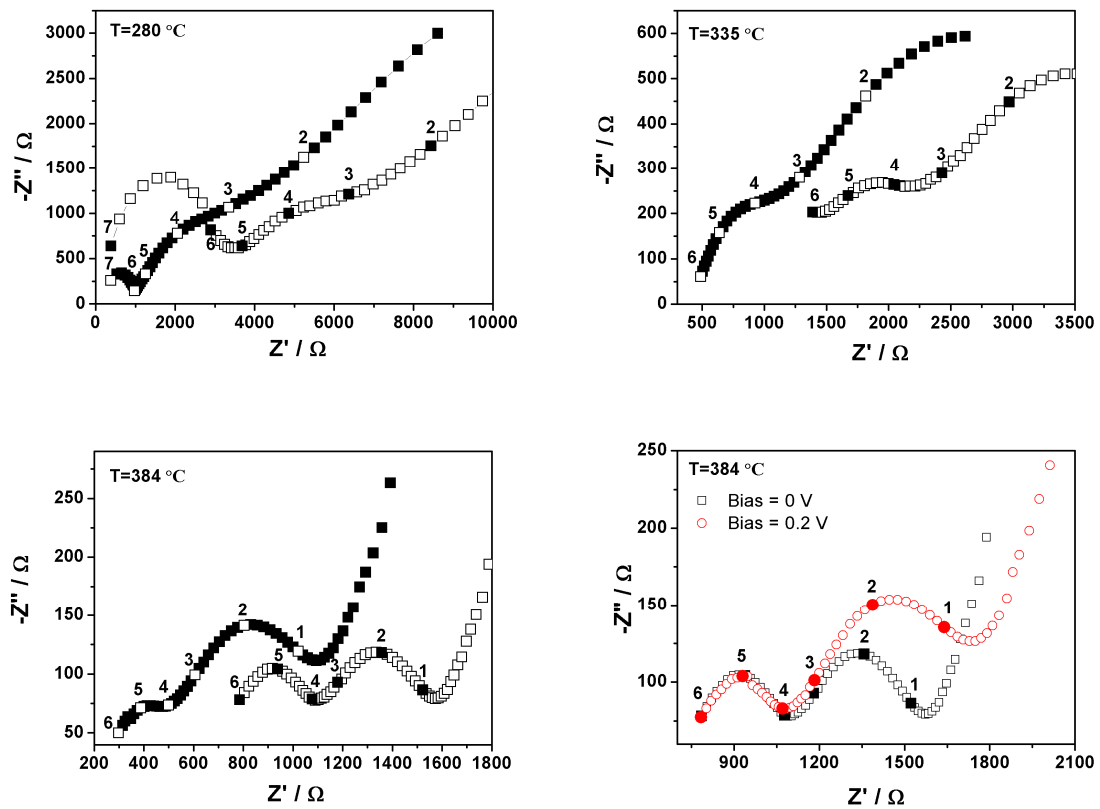


**Figure 5.7** The impedance Spectroscopy of BSY25-4ZnO in the dry and wet air at different temperature (solid symbol - wet air, open symbol - dry air).

The Arrhenius plots of the total, bulk and grain boundary conductivity are shown in **Figure 5.8**, and the activation energies are listed in **Table 5.2**. The total conductivities do not show significant differences, but the total conductivity of BSY25-4ZnO is slightly

higher than that of the other compounds. **Figure 5.8** also shows that the bulk conductivities are unaffected by the ZnO as a sintering aid. However, the bulk conductivity of BSY25Zn4 (*i.e.* Zn as a second dopant) is much lower than that of unmodified BSY25 and BSY25-4ZnO. Also, the activation energy of bulk conduction for BSY25Zn4 (0.53 eV) is higher than that of BSY25 (0.41 eV) and BSY25-4ZnO (0.39 eV) compounds. For ZnO as a sintering aid, Babilo *et al.* [2] reported that the bulk conductivity of 4 mol % ZnO modified  $BaZr_{0.85}Y_{0.15}O_{3-\delta}$  is lower than that of unmodified. However, in this study, we observed that ZnO as a sintering aid did not affect the bulk conductivity. It may be due to the different experimental methods. In Babilo's study, the wet chemical method was used to prepare Y-doped  $BaZrO_3$  with ZnO additive, and ZnO was introduced prior to pure phase Y-doped  $BaZrO_3$ . However, in our study, ZnO was introduced into pure phase BSY25 compounds. The amount of Zn entering inside the structure may be very small comparing with Babilo's study.

For the grain-boundary conductivity, **Figure 5.8 (c)** shows that the grain boundary conductivities of BSY25Zn4 and BSY25-4ZnO are slightly higher than that of BSY25. **Figures 5.4-6** reveal that the grain sizes of the compounds are similar (between 1-2  $\mu\text{m}$ ). The increase of grain boundary conductivity of modified BSY25 with ZnO may be due to the low sintering temperature leading to no impurities accumulated in the grain boundary. The total and bulk conductivities increased in wet air at low temperature due to proton conduction, the activation energies of total conductivity in wet air were  $\sim 0.62$  eV, similar to  $BaZr_{0.25}In_{0.75}O_{3-\delta}$  (0.63 eV) [18]. The activation energies of bulk conductivities were between 0.39 eV and 0.53 eV, which is typical for proton conductors (0.4 - 0.5 eV) [19-20].

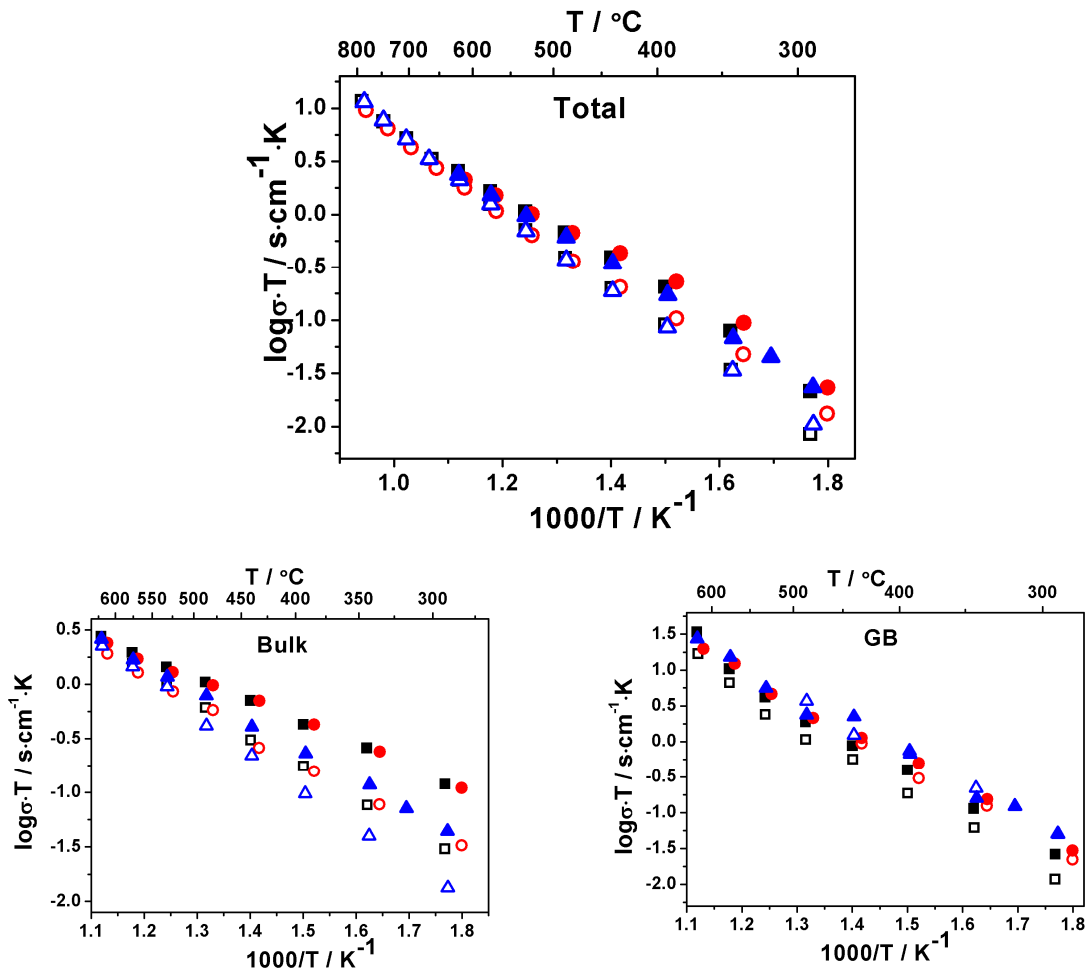


**Figure 5.8** The conductivity of pellets measured in dry and wet air. ■- BSY25 in wet air, □- BSY25 in dry air, ○- BSY25-4ZnO in dry air, ●- BSY25-4ZnO in wet air, ▲ - BSY25Zn4 under wet air, △- BSY25Zn4 in dry air.

Compounds	Total_Dry	Bulk_Dry	GB_Dry	Total_Wet	Bulk_Wet	GB_Wet
BSY25	0.74	0.58	0.93	0.62	0.41	0.90
BSY25-4ZnO	0.65	0.53	0.83	0.61	0.39	0.82
BSY25Zn4	0.72	0.69	0.79	0.62	0.53	0.81

Note: the activation energy under dry air was fitted from 800-500 °C, under wet air from 400 °C to 250 °C.

**Table 5.2** the activation energy of BSY25, BSY25-4ZnO and BSY25Zn4

## 5.4 Conclusion

Single-phase and dense BSY25 compound has been successfully prepared at 1300°C by adding 4 mol % ZnO as a sintering aid and dopant. This temperature is significantly lower than the one required to obtain single-phase (1400°C) and much lower than the one to obtain dense dense ceramics (1600°C) without ZnO. From analysis of XRD and SEM, all compounds are single phase with cubic perovskite structure. Zinc oxide as a sintering aid does not affect the bulk conductivity, and slightly increases the total conductivity. However, Zn as a second dopant decreases significantly the bulk conductivity. The activation energies of bulk conductivities are between 0.39 eV and 0.53 eV in wet air, which suggests that the charge carriers are protons at low temperature. The total conductivity of BSY25-4ZnO reaches  $2.4 \times 10^{-3} \text{ S} \cdot \text{cm}^{-1}$  at 621°C in the humidified air.

## References

- [1] C. Savaniu, J. T. S. Irvine, *Solid State Ionics* **2003**, 162-163, 105.
- [2] P. Babilo, S. M. Haile, *Journal of the American Ceramic Society* **2005**, 88, 2362.
- [3] J. T. S. I. S. W. Tao, *Advanced Materials* **2006**, 18, 1581.
- [4] S. Tao, J. T. S. Irvine, *Journal of Solid State Chemistry* **2007**, 180, 3493.
- [5] A. K. Azad, J. T. S. Irvine, *Solid State Ionics* **2008**, 179, 678.
- [6] A.M. Azad, N. C. Hon, *Journal of Alloys and Compounds* **1998**, 270, 95.
- [7] W. Lu, H. Schmid, *J Sol-Gel Sci Techn* **2007**, 42.
- [8] M. Licheron, G. Jouan, E. Husson, *Journal of the European Ceramic Society* **1997**, 17, 1453.
- [9] J. James, O. B. S. Kumar, S. Senthil Kumar, *et al.*, *Materials Letters* **2003**, 57, 3641.
- [10] C. P. Udawatte, M. Kakihana, M. Yoshimura, *Solid State Ionics* **1998**, 108, 23.
- [11] A. Rolle, H. Seymour, P. Roussel, A. Rubbens, R.N. Vannier, *Ionics* **2008**, 14, 477.
- [12] P. Singh, O. Parkash, D. Kumar, *Solid State Ionics* **2005**, 176, 2167.
- [13] T. Schober, *Solid State Ionics* **1998**, 109, 1.
- [14] P. Murugaraj, K. D. Kreuer, T. He, T. Schober, J. Maier, *Solid State Ionics* **1997**, 98, 1.
- [15] R. D. Shannon, *Acta Cryst.* **1976**, A32, 751.
- [16] A. Magrez, T. Schober, *Solid State Ionics* **2004**, 175, 585.
- [17] A. C. Caballero, J. F. Fernandez, C. Moure, P. Duran, Y. M. Chiang, *Journal of the American Ceramic Society* **1998**, 81, 939.
- [18] I. Ahmed, S. G. Eriksson, E. Ahlberg, *et al.*, *Solid State Ionics* **2006**, 177, 1395.
- [19] K. D. Kreuer, *Solid State Ionics* **1999**, 125, 285.
- [20] K. D. Kreuer, *Ann. Rev. Mater. Res.* **2003**, 33, 333.

# Chapter 6 Atomistic Simulation of Pure and Doped BaSnO<sub>3</sub>

## 6.1 Introduction

In the previous chapters, the defect chemistry, microstructure and transport properties of acceptor-doped BaSnO<sub>3</sub> have been investigated by XRD, SEM, TGA and IS. In order to understand well the influence of the dopant nature and content on the defect chemistry of pure and doped BaSnO<sub>3</sub>, in particular, dopant site occupancy and dopant association energy, atomistic simulations are of prime importance. In our group, we have carried out calculations based on DFT and semi-empirical simulations. A DFT's study from our group has shown that the dopant-oxygen vacancy and dopant-proton interaction depends strongly on the dopant nature and the mobile atom stable position is rarely close to the dopant [1]. This would allow explaining that high dopant concentrations are not necessarily to ensure significant ion conduction. Another study of stannate compounds using semi-empirical potentials also gave some first results on the surface energies and redox reactions [2].

Atomistic simulations based on semi-empirical interatomic potentials have been applied successfully for the study of the defect properties of a range of perovskite-type proton and oxide-ion conductors. In particular, this helped to predict defect energies and to propose ionic transport model at the atomic level [3-11], having a predictive role in the design and improvement of materials.

In this chapter, we have explored the properties of pure and trivalent ions (Fe, Sc, In, Y, Gd, Sm, Nd and La) doped BaSnO<sub>3</sub> by atomistic simulations. These atomistic simulations were essentially based on semi-empirical potentials but DFT calculations were also used to give complementary information on electronic properties (the calculations were done by *Emile Bévilion* and *Grégory Geneste*). We will show that these calculations help not only to give local information on the defects

energetics but also on their macroscopic counterpart such as the evolution of cell parameters with doping. This study is voluntarily limited to dry samples *i.e.* we do not study here the incorporation of protons inside the structure.

## 6.2 Methods

### 6.2.1 Atomistic simulation technique

Two kinds of approaches were used here, one based on semi-empirical potential the other one based on DFT calculations. The first one is less CPU-costing but hardly gives precise information on electronic state. The second one is in this sense more complete but limited to very small systems.

The basis of atomistic semi-empirical simulation is the specification of an interatomic potential model, which describes the potential energy of the system as a function of the atomic coordinates and allows the modeling of perfect and defective lattices. The lowest energy configuration of the crystal structure is determined by using energy minimization procedures. The Born model representation is commonly used for ternary oxides, with the energy partitioned into long-range Coulombic and short-range pair potentials of the Buckingham form:

$$V_{ij}(r_{ij}) = A \exp\left(-\frac{r}{\rho_{ij}}\right) - \frac{C}{r_{ij}^6} \quad (6-1)$$

Where A,  $\rho$  and C are adjustable parameters assigned to the cation-oxide anion interaction. In the present study, the values of these parameters were taken from Ref [12-14] (Table 6-1). Those corresponding to Ba and Sn were shown to reproduce well the perfect lattice properties of simple oxides and also of BaSnO<sub>3</sub>. These properties are gathered in Table 6-2.

<b>M<sup>···</sup>O</b>	<b>A</b> (eV)	<b>ρ</b> (Å)	<b>C</b> (eV, Å <sup>6</sup> )	<b>Y(e)</b>	<b>K</b> (eV Å <sup>-2</sup> )	<b>Ref</b>
<b>O<sup>2-</sup></b>	<b>9547.96</b>	<b>0.2192</b>	<b>32.00</b>	<b>-2.389</b>	<b>23.09</b>	[12]
<b>Ba<sup>2+</sup></b>	<b>873.829</b>	<b>0.3863</b>	<b>0.0</b>	<b>9.203</b>	<b>459.2</b>	[12]
<b>Sn<sup>4+</sup></b>	<b>1056.8</b>	<b>0.3683</b>	<b>0.0</b>	<b>1.58</b>	<b>2037.8</b>	[12]
<b>La<sup>3+</sup></b>	<b>2088.89</b>	<b>0.3460</b>	<b>23.25</b>	<b>3.0</b>		[13]
<b>Nd<sup>3+</sup></b>	<b>1995.20</b>	<b>0.3430</b>	<b>22.59</b>	<b>3.0</b>		[13]
<b>Sm<sup>3+</sup></b>	<b>1944.44</b>	<b>0.3414</b>	<b>21.49</b>	<b>3.0</b>		[13]
<b>Gd<sup>3+</sup></b>	<b>1885.75</b>	<b>0.3399</b>	<b>20.34</b>	<b>3.0</b>		[13]
<b>Y<sup>3+</sup></b>	<b>1766.40</b>	<b>0.33849</b>	<b>19.43</b>	<b>3.0</b>		[13]
<b>In<sup>3+</sup></b>	<b>1495.65</b>	<b>0.3327</b>	<b>4.33</b>	<b>3.0</b>		[14]
<b>Sc<sup>3+</sup></b>	<b>1575.85</b>	<b>0.3211</b>	<b>0.0</b>	<b>3.0</b>		[14]
<b>Fe<sup>3+</sup></b>	<b>1414.60</b>	<b>0.3128</b>	<b>0.0</b>	<b>3.0</b>		[14]

**Table 6.1** Buckingham Interatomic potential parameters

In addition to studying the perfect lattice, an important feature of this approach is to predict how the lattice ions accommodate various kinds of defects. To do this, the energy of a defect, such as a vacancy, an interstitial ion, or a substitutional ion is calculated via the Mott-Littleton approach [15]. This method consists in partitioning the crystal lattice into two regions so that the ions in a spherical inner region surrounding the defect are relaxed explicitly, see **Figure 6.1**. In contrast, the remainder of the crystal, where the defect forces are relatively weak, is treated by more approximate quasi-continuum methods. In this way, local relaxation is effectively modeled and crystal is not considered simply as a rigid lattice. In the present calculations, the radii of regions I and IIa were 12 Å and 24 Å, respectively. Region sizes were chosen to be large enough to ensure that no appreciable change in defect formation energy occurred if the region sizes were increased further.

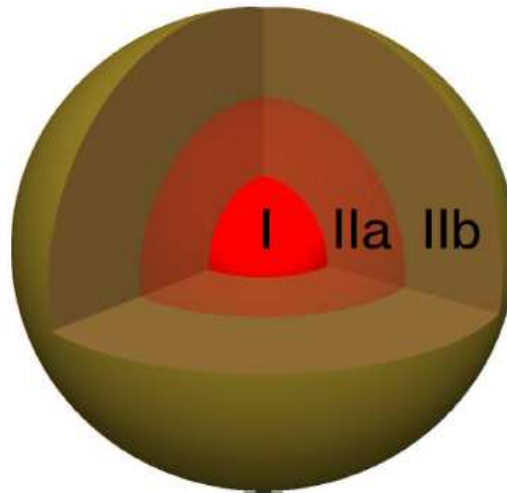


**Figure 6.1** Representation of the two region approach for defect energy calculations. The inner region, I, surrounds the defect and ion displacements are calculated explicitly. In the outer region, IIb, displacements are calculated using the Mott-littleton approximation. Region IIa acts as a transition between Region I and IIb [16].

In all calculations, the electronic polarizability of  $O^{2-}$ ,  $Ba^{2+}$  and  $Sn^{4+}$  ions are accounted for by the so-called shell model, see **Figure 6.2**. This model consists of a massless shell with charge  $Y|e|$  that is allowed to move with respect to a massive core of charge  $X|e|$ . The core and shell charges are connected by an isotropic harmonic spring force constant  $k$ . Displacement of the shell relative to the core gives a good description of electronic polarization and allows in particular the computation of the optical dielectric constant, not possible within a rigid-ion model. In all cases, calculations have been conducted using the Gulp code that include all the features detailed above [17].

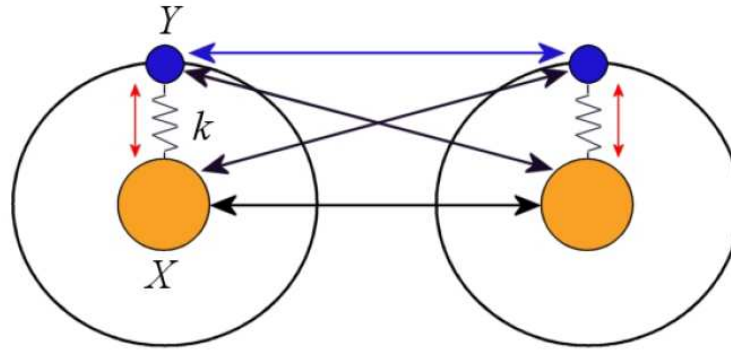


**Figure 6.2** The shell model. The orange atom is the core and the blue atom represents the charge of the massless shell. The red arrows represent polarization, black arrows represent Coulombic interactions and blue arrow represents short range interaction [18].

In order to give complementary information to semi-empirical simulations, we also performed a number of density-functional calculations with the SIESTA code [19, 20]. We used the GGA-PBE [21] functional to describe the exchange-correlation energy. In this case, the core electrons are treated through Troullier-Martins pseudopotentials [22], that include as valence electrons the 5s, 5p and 6s for Ba, the 4d, 5s and 5p for Sn and the 2s and 2p for O. This numerical scheme provides for cubic BaSnO<sub>3</sub> an equilibrium lattice constant of 4.21 Å, with a typical overestimation of the GGA. The defects studied by this method (neutral oxygen vacancy, neutral oxygen interstitial) are included in a 2×2×2 supercell (40 atoms if no defect). The configurations are optimized until all the components of the Hellman-Feynman forces are below 0.02 eV/angstrom.

### 6.2.2 Defective unit cell volumes

The Mott-Littleton defect calculations have been also used to predict lattice volumes, using an approximation of non interacting defects. More concretely, the defect relaxation volume,  $v$ , can be calculated from [14, 23, 24]:

$$v = -k_T V_C \left( \frac{\partial f_v}{\partial v} \right)_T \quad (6-2)$$

Where,  $k_T$  is the isothermal compressibility and  $v$  the unit cell volume.  $(\partial f_v / \partial v)_T$  is the change at constant temperature, in the Helmholtz defect formation energy as a function of the change in the unit cell volume. Given the defect relaxation volume, the unit cell volume can then be determined from the following equation:

$$V_{cell} = \sum V_{defect} \times c_{defect} + V_{perfect} \quad (6-3)$$

Where,

$$\sum V_{defect} = V_{M_{Sn}} + \frac{1}{2} V_{V_O}, \quad c_{defect} = \frac{[M]}{[M] + [Sn]}, \quad V_{perfect} = (4.1236)^3 = 70.118 \text{ \AA}^3$$

This approach will be used not only to determine the influence of dopant size on cell parameters but also the influence of dopant content on the same evolution. Surprisingly, we will see that this approach works very well even if the approximation of non-interacting defects is obviously not correct in particular for high doping level.

## 6.3 Results and discussions

### 6.3.1 Basic properties of BaSnO<sub>3</sub>

Before studying defects, it is necessary to simulate the properties of pure BaSnO<sub>3</sub>. **Table 6.2** shows the simulated properties values including lattice parameter, lattice energy, mechanical properties and dielectric properties. The calculated  $a$  lattice parameter of the  $Pm\bar{3}m$  perovskite structure is found to be in very good agreement with the experimental value. Indeed, the lattice parameter of BaSnO<sub>3</sub> is reproduced to within 0.17 % of the experimental value. The calculated mechanical and dielectrics properties are also consistent with the experimental values [25] and with those obtained by means of first-principles density functional calculations [26].

To evaluate thermal expansion coefficients, the ZSISA method (Zero Static Internal Stress Approximation) was used in this work to evaluate the cell parameters at different temperature. In the ZSISA method, only the strain derivatives with respect to the free energy are used while the internal derivatives neglect the free energy

contribution [27]. This approach has been found to be more stable at higher temperatures than total free energy minimization. **Figure 6.3** shows that the temperature evolution of the lattice parameter is linear and the thermal expansion coefficient calculated is  $1.06 \times 10^{-5} \text{ K}^{-1}$  (300-800 K), close to the experimental data  $9.6 \times 10^{-6} \text{ K}^{-1}$  [25, 26] for the same range of temperature.

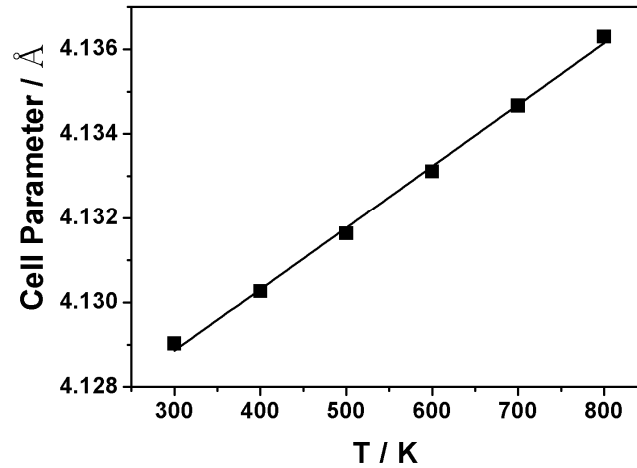


**Figure 6.3** Cell parameter as a function of temperature of pure BaSnO<sub>3</sub>.

Properties	This study	DFT [28]	Experiment [25]
Lattice parameter (Å)	4.1236	4.156	4.116
Lattice energy(eV)	-144.32	-	-
Static dielectric constant	23.63	22.3	-
High frequency dielectric constant	4.24	4.89	-
Elastic constant (GPa/m <sup>2</sup> )	$\epsilon_{11}=280.36$ $\epsilon_{66}=137.64$	-	-
Young modulus(GPa)	189.72	207	244
Poisson coefficient	0.329	0.233	-
Shear modulus(GPa)	100.4	84	99.9
Compressibility(GPa <sup>-1</sup> )	$5.4 \times 10^{-3}$	-	$6.86 \times 10^{-3}$

**Table 6.2** Calculated and Experimental Properties of BaSnO<sub>3</sub>

Therefore, the potentials used allow reproducing reasonably well the structural,

elastic and dielectric properties of pure BaSnO<sub>3</sub> and are thus validated for the following calculations.

### 6.3.2 Intrinsic atomic defects

We first calculated the major point defects formation energy. Solutions energies were then evaluated from solution equations on the basis of isolated *i.e.* non interacting point defects (vacancies and interstitials). To calculate the energy of a vacancy, an ion was removed from its lattice site and placed at an infinite distance. An interstitial was modelled in the same way by taking an ion from infinity and placing it at an interstitial site. The calculated energies are reported in **Table 6.3**, with the exception of cation interstitial and Frenkel energies, since they led to calculations instabilities. Anyway they are undoubtedly higher in energy and thus will not be considered further. The lattice energy used in the calculation of Schottky-type defects were obtained from atomistic simulation of BaSnO<sub>3</sub>, SnO<sub>2</sub> and BaO.

Examination of **Table 6.3** reveals that the creation of Frenkel and Schottky defects corresponds to substantial amounts of energy. The most favourable energy is found for the formation of Ba Schottky-type disorder which could result in loss of BaO at high temperature. This behaviour is very well known in Ba-containing oxides and a recent study on cation non-stoichiometry in BaCeO<sub>3</sub> confirms that barium loss does occur at high temperatures [29]. However, as a general rule, the magnitude of the calculated energies suggests that the concentration of intrinsic atomic defects is relatively small.

Parameter	Defect equilibrium	Formation energy (per defect /ev)
Ba <sup>2+</sup> vacancy		19.1
Sn <sup>4+</sup> vacancy		83.99
O <sup>2-</sup> vacancy		18.64
O <sup>2-</sup> interstitial		-9.05
Schottky	$Ba_{Ba}^{\times} + Sn_{Sn}^{\times} + 3O_o^{\times} = V_{Ba}'' + V_{Sn}'''' + 3V_o^{\cdot\cdot} + BaSnO_3$	4.938
O Frenkel	$O_o^{\times} = V_o^{\cdot\cdot} + O_i''$	4.795
Ba Schottky-type	$Ba_{Ba}^{\times} + O_o^{\times} = V_{Ba}'' + V_o^{\cdot\cdot} + BaO$	2.615
Sn Schottky-type	$Sn_{Sn}^{\times} + 2O_o^{\times} = V_{Sn}'''' + 2V_o^{\cdot\cdot} + SnO_2$	6.757

Table 6.3 Isolated point defects

### 6.3.3 Redox reactions

It is essential to understand the stability and behaviour of electronic defects with respect to the lattice defects since most applications *i.e.* fuel cells or gas sensors require the materials to be used from highly reducing to highly oxidising atmospheres. Allan *et al.*[2] investigated defect and surface structure of the ASnO<sub>3</sub> (Ca, Sr, Ba) stannates as oxidation catalysts by atomistic simulations. The formation energies of cations vacancies and interstitials were calculated to be very high compared to that of anions. Therefore, in the present study, we only considered the possibility of oxygen vacancy for reduction and oxygen interstitial or oxygen vacant site filling for oxidation. For the undoped system, the following reactions for oxidation and reduction were considered.

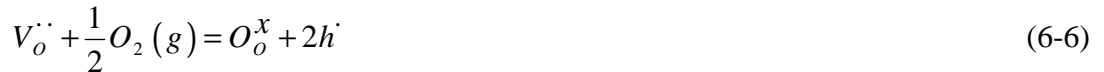
For reduction:



For oxidation:



Taking into account the fact that charge-compensating oxygen vacancies are created on acceptor-doping, we also considered the following equation for acceptor-doped samples:



These calculations were performed by means of DFT. For reduction, a neutral oxygen vacancy is placed in the supercell described above and the system is optimized. The question is whether the two electrons left by the missing oxygen atom occupy an extended state (like those of the conduction band in a semiconductor) or a spatially-localized state (polaron-like). After optimization, and although the oxygen vacancy would be a priori surrounded by two equivalent Sn atoms, we observed that only one Sn atom has a Mulliken charge that differs significantly from the others: 7 among the eight Sn atoms of the supercells have equal Mulliken charge within 0.03, while the 8<sup>th</sup> (one of the two surrounding the vacancy) has a Mulliken charge 0.18 lower than the seven others. The Ba atoms have all their charges equal within 0.01, while the O atoms also have charges equal within 0.04. This result clearly indicates that the charge left by the missing O is localized directly on one single Sn (small bound polaron) and does not occupy any extended state. It is noteworthy that the charge does not localize on the two Sn surrounding the vacancy but prefers to localize on one single Sn. This is compatible with the known oxidation degrees of Sn (+4 and +2). As a consequence, the distance from the reduced Sn to the neighbouring O is increased (between 2.16 and 2.20 Å) with respect to the Sn-O distance in pure barium stannate (2.105 Å in GGA).

This would justify the possible semi-empirical modelling (not considered here) of reduced barium stannate by the replacement of one Sn<sup>4+</sup> ion by one with lower charge. It is noteworthy that adding (resp. removing) an additional electron in the

supercell (without introducing any point defect) results in a uniform distribution of the additional (resp. missing) charge on the Sn atoms rather than the localization on a single Sn. It means that in this latter case, the additional (resp. missing) charge corresponds to the density of probability of an extended conduction band state (resp. valence band state). The reduction of Sn from +4 to +2 is thus probably intrinsically related to the existence of the point defect (O vacancy).

For oxidation reaction, we first examined pure BaSnO<sub>3</sub> in which one extra oxygen atom is inserted as interstitial in the 2×2×2 supercell. It is clear that neither Ba nor Sn can be more oxidized. In such systems, one usually observes the formation of suboxide species (peroxide O<sub>2</sub><sup>2-</sup> or superoxide ions O<sub>2</sub><sup>-</sup>). This is precisely what happens in this case: the extra O atom forms a bond with one oxygen of the structure (see **Figure 6.4**). The two atoms share the charge (equal Mulliken charges within 0.01, which are higher than the charges of all the other O atoms by approximately 0.21 per oxygen atom), and their bond is 1.49 Å, which is typically the bond length of peroxide ions O<sub>2</sub><sup>2-</sup>. The charges of the Ba and Sn are almost not affected.

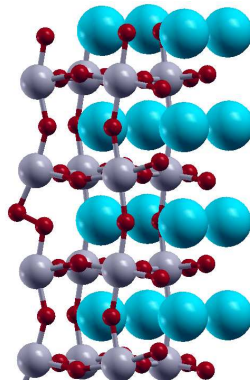


**Figure 6.4** Structure of peroxide ion as obtained from oxygen insertion into the BaSnO<sub>3</sub> cell.

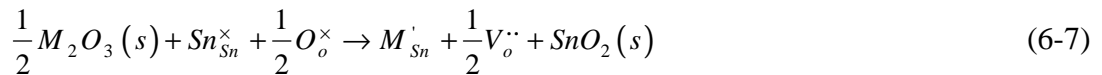
Let us precise that in acceptor-doped compounds, no oxygen interstitial is necessary since oxygen vacancies are already present. We have thus calculated the energy of a In-doped and Y-doped barium stannate (25 mol % doping rate) without oxygen vacancies, *i.e.* under strong oxidizing atmosphere. It is usually admitted that

the filling the oxygen vacancies leads to the appearance of holes in the electronic structure. Indeed, we find the two calculated systems to be metallic, with empty states close to the valence band top (holes). It is besides generally observed that holes in oxides systems behave like polarons. No evidence of polaronic like behaviour that would be reflected by a localisation of charges is put into evidence here but the small size of the system impedes such a description. Nevertheless, we should keep in mind that the actual measurements of BSY compounds as a function of atmosphere (see chapter 4) revealed the contribution of holes at high oxygen partial pressure. In this case, the electrical behaviour was found to be polaronic *i.e.* with like semi-conductor behaviour and activation energy is slightly smaller to that of oxygen atoms.

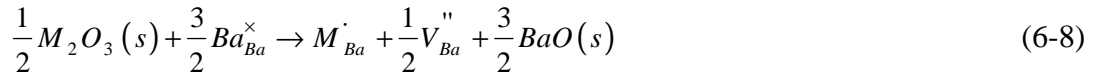
Concerning energies associated to these oxidation/reduction reactions, the **Eq. (6-4)** is associated to an enthalpy value of 4.0 eV. This value is high but significantly smaller than the one obtained for BaZrO<sub>3</sub> from similar DFT calculations [30]. This would signify that BaSnO<sub>3</sub> would reduce more easily than BaZrO<sub>3</sub> would do. Concerning oxidation reaction, the insertion of a neutral oxygen atom is associated with a very low positive enthalpy of 1.1 eV. This means that such reaction is not probable. Besides, this reaction becomes less and less favoured at high temperature due to the entropic contribution of gaseous oxygen to the reaction total free energy. The **Eq. (6-6)** is associated with negative enthalpies, respectively for In<sup>3+</sup> and Y<sup>3+</sup> dopants, in close agreement with the calculated value of -1.21 eV for BaZrO<sub>3</sub> by Sundell *et al.* [30]. Nevertheless, still here, the entropic contribution of gaseous oxygen is not taken into account neither the barrier to dissociate the O<sub>2</sub> molecule. The negative value of enthalpy would mean that the system naturally evolves toward the incorporation of oxygen and creation of holes in oxidative atmosphere, at least at low temperature, and that charged oxygen vacancies become stable when temperature increases. In reality, if an important incorporation of oxygen is not readily observed at low temperature, the p-type behaviour has been measured in air at temperatures between 600°C and 900°C.

### 6.3.4 Dopant-ion substitution

The substitution of a range of trivalent cations was investigated on both Ba and Sn sites for BaSnO<sub>3</sub> lattice in order to gain some insight into energy cost and subsequent preferential sites of dopants in host lattice. Substitution of the dopants on the Sn site was analyzed according to the standard “acceptor-doping” defect reaction, with the creation of oxygen vacancies as charge-compensating defects:



For substitution on the Ba site, dopant incorporation was described by:



The substitution on the Ba site, which contrarily to substitution on Sn site, does not produce oxygen vacancies but leads to BaO elimination. The energies associated to these reactions were evaluated by combining corresponding defect and lattice energy terms. Such an approach provides a useful systematic guide to the relative energies for the doping of different atoms at the same site. The resulting solution energies for substitution on the Ba and Sn sites as a function of ionic Shannon radius [31] are presented in **Figure 6.5**. 6-fold radius is used in both A and B-site substitution for reasons of simplicity.

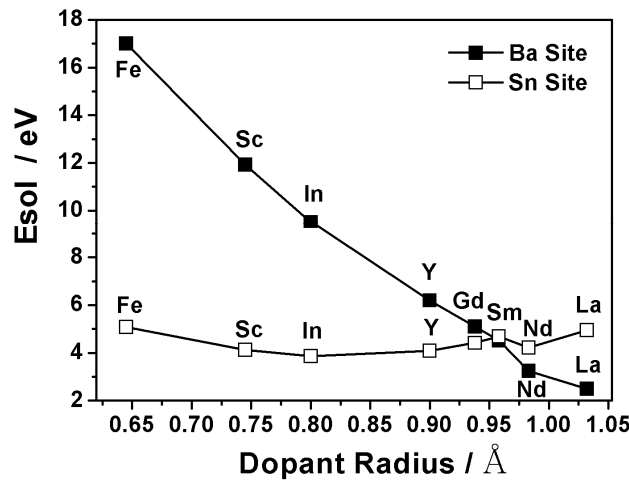


**Figure 6.5** calculated solution energy as a function of dopant radius.

Examination of the results reveals an important correlation between solution energy and ion size. This was already the case for other perovskite compounds [5, 6, 9, 32]. The majority of dopants ions (with exception of Sm, Nd and La) are predicted to substitute preferentially for Sn in BaSnO<sub>3</sub>. From the values of solution energy, we predict In<sup>3+</sup> and Y<sup>3+</sup> to be among the most favourable dopants for BaSnO<sub>3</sub>. This agrees with the experimental work of Schober [33, 34] where these cations were used as acceptor dopant for effective proton conduction. Nevertheless, the solution energy on B-site is almost the same for Sc<sup>3+</sup>, In<sup>3+</sup> and Y<sup>3+</sup> cations while their ionic radius differs by more than 0.15 Å. Besides, Y solution energy on B-site is one of the lowest in spite of the big radius difference between Y<sup>3+</sup> (0.9 Å [31]) and Sn<sup>4+</sup> (0.69 Å [31]). This situation is rather different from the one observed in fluorite compounds for which the lowest solution energy generally corresponds to a dopant atom with a radius very close to that of host atom [14, 24, 35]. Nevertheless, such behaviour has already been observed in perovskite compounds. Indeed, Islam *et al.* [9] showed that in barium zirconate compound the favourable substitution on B-site correspond to Y<sup>3+</sup> and Gd<sup>3+</sup> whose radii differ also by more than 0.148 Å with that of Zr<sup>4+</sup>. This can be interpreted by the fact that perovskite structure is known to accommodate much deviation from the ideal structure. Besides, in the case of BaSnO<sub>3</sub>, the tolerance factor is calculated to be 1.02 which means that the atom radius on B-site is small if compared to the available volume. This might then explain why bigger atoms might be incorporated in the structure without an important energy cost. It is interesting to note that Sm<sup>3+</sup> cation sits at the crossover points in Figure 3 which suggests possible substitution at either Ba or Sn sites. This also exists in other perovskite oxide, such as Nd in BaZrO<sub>3</sub> and Y in CaZrO<sub>3</sub> [9]. Our simulations suggest that similar effect might occur for larger dopants (eg. Nd and La) which have a lower calculated solution energy on Ba site. In fact, the real situation is somewhat different since cations are incorporated in stoichiometric proportion corresponding to substitution on either site. Nevertheless, this means that for larger dopant some partial substitution on A-site should not be discarded. A similar

phenomenon was reported in Barium cerate compounds [6]. Indeed, Haile *et al.* [36] showed that nominally B-site doped Ba<sub>x</sub>Ce<sub>0.85</sub>M<sub>0.15</sub>O<sub>3-d</sub> (x=0.85-1.20) can exhibit significant Nd dopant partitioning over both Ba and Ce sites.

### 6.3.5 Defect volume and cell parameter

In this section, the variation of lattice parameter with dopant radius and solute concentration was calculated. In this case, we only considered the substitution of atoms on B-site. We then compared these calculations to experimental data. Table 4 shows the volume associated to the punctual defect according to the method described above. We observe first that oxygen vacancy might have a negligible influence on cell volume evolution. Actually, from these results, 33 % of oxygen vacancies in BaSnO<sub>3</sub> would result in a less than 1 % contraction on the cell parameter. This was already shown by Mogensen *et al.* [37] who demonstrated that oxygen vacancy ( $r(v_o^-) = 1.3771 \text{ \AA} \sim 1.4045 \text{ \AA}$ ) has a volume similar to that of an oxygen ion. Then, we observe that only Fe<sup>3+</sup> substitution on B-site cation leads to a negative defect volume, which actually corresponds to the fact that this atom has a smaller radius than tin. However, as shown from the following table, the presence of barium vacancies or of dopant atom Gd<sup>3+</sup>, Sm<sup>3+</sup> and La<sup>3+</sup> on A-site also leads to a diminishing of a negative defect volume, and thus to a decrease of cell parameters. The presence of these two defects could thus explain the evolution of cell parameters confirming the model proposed in chapter 3.

Defect	Defect relaxation volume (Å <sup>3</sup> )/defect	Defect	Defect relaxation volume (Å <sup>3</sup> )/defect
$V_O^{\bullet\bullet}$	-1.35	$V_{Ba}^{\bullet\bullet}$	-1.86
$Fe_{Sn}^{\cdot}$	-3.22		
$Sc_{Sn}^{\cdot}$	3.54		
$In_{Sn}^{\cdot}$	7.34		
$Y_{Sn}^{\cdot}$	13.97		
$Gd_{Sn}^{\cdot}$	17.36		
$Sm_{Sn}^{\cdot}$	19.31	$Sm_{Ba}^{\cdot}$	-7.87
$Nd_{Sn}^{\cdot}$	21.19	$Nd_{Ba}^{\cdot}$	-7.00
$La_{Sn}^{\cdot}$	24.9	$La_{Ba}^{\cdot}$	-5.27

**Table 6.4** Defect relaxation volume

**Figure 6.6** shows the predicted lattice parameters as a function of dopant radius and concentration for BaSn<sub>0.75</sub>M<sub>0.25</sub>O<sub>3-δ</sub> (M = Fe, Sc, In, Y, Gd, Sm, Nd and La) and BaSn<sub>1-x</sub>Y<sub>x</sub>O<sub>3-δ</sub> (x = 0-0.375). The examinations of the results reveal that lattice parameters predictions reproduce well the experimental data for the BaSn<sub>1-x</sub>Y<sub>x</sub>O<sub>3-δ</sub> system, except for In<sup>3+</sup>, Sm<sup>3+</sup>, Nd<sup>3+</sup> and La<sup>3+</sup>. For In<sup>3+</sup> substitution, it is probable that the actual experimental composition is different from the nominal formula due to indium evaporation during thermal treatment. This would explain why the cell parameter of indium substituted compound is smaller than expected. For Sm<sup>3+</sup>, Nd<sup>3+</sup> and La<sup>3+</sup>, the lattice parameters predicted are higher than the experimental ones possibly due to partial substitution on A-site. This would confirm the tendency foreseen by solution energy calculations presented above. **Figure 6.6** also shows the evolution of cell parameter for Y doped compounds with doping level ranging from 0 to 37.5 mol %. In this case, the agreement is very good. This is all the most surprising since, for these calculations, defects are considered as non-interacting which is evidently far from the reality for such doping levels.

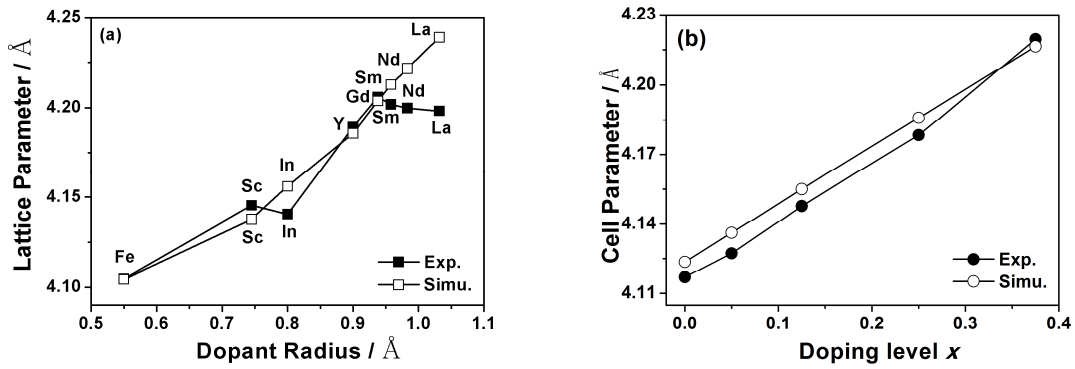


**Figure 6.6** Comparison of experimental and predicted lattice parameter: (a) Lattice parameter as a function of dopant radius in BaSn<sub>0.75</sub>M<sub>0.25</sub>O<sub>3- $\delta$</sub>  (M = Fe, Sc, In, Y, Gd, Sm, Nd and La), (b) Lattice parameter as a function of dopant concentration in BaSn<sub>1-x</sub>Y<sub>x</sub>O<sub>3- $\delta$</sub>  ( $x = 0, 0.05, 0.125, 0.25$  and  $0.375$ ).

### 6.3.6 Defect association

It is well known that the charge-compensating oxygen vacancies, which form upon acceptor doping, tend to interact attractively with dopant, leading to defect clustering. The formation of such cluster adds an additional binding (or association) term to the activation energy for oxide-ion conductivity. The magnitude of this interaction is related to the binding energy, defined as the difference between the formation enthalpy of the appropriate defect cluster and the sum of the formation enthalpies of the isolated point defects:

$$E_{bind} = E_{cluster} - \sum E_{isolated-defect} \quad (6-9)$$

We have considered the energies of simple defects configuration consisting of a pair cluster ( $M'_{Sn} : V''_o$ )<sup>\*</sup> at an adjacent (nearest neighbour, NN) site and second coordination shell (next-nearest neighbour, NNN) sites, see **Figure 6.7**. The cluster binding energies associated to these two configurations are reported in **Figure 6.8**.

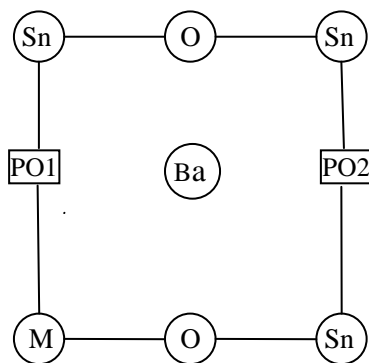


**Figure 6.7** Dopant-vacancy cluster configuration in BaSnO<sub>3</sub>, PO1: Nearest neighbour (NN), PO2: Next-nearest neighbour (NNN).

**Figure 6.8** reveals that the most stable configuration of the defect cluster depends on the size of the dopant cation. For dopant cations (such as Fe<sup>3+</sup>, Sc<sup>3+</sup> and In<sup>3+</sup>), smaller than Y<sup>3+</sup>, it is energetically more favourable for the vacancy to locate at an NN site, whereas larger dopant cations (such as Gd<sup>3+</sup>, Sm<sup>3+</sup>, Nd<sup>3+</sup> and La<sup>3+</sup>) favour the NNN site for the vacancy.

For Y<sup>3+</sup>, the difference of binding energy is small between NN and NNN configuration. Thus as the oxygen vacancy moves away from the Y<sup>3+</sup> ion, there is very little change in the binding energy.

Such inversion between NN and NNN site stability for the O vacancy has been reported at larger dopant concentration from ab initio calculations [38]. Although the larger concentration leads to larger binding energies, the largest dopants are also found in most cases by these authors to stabilize the O vacancy in the NNN site.

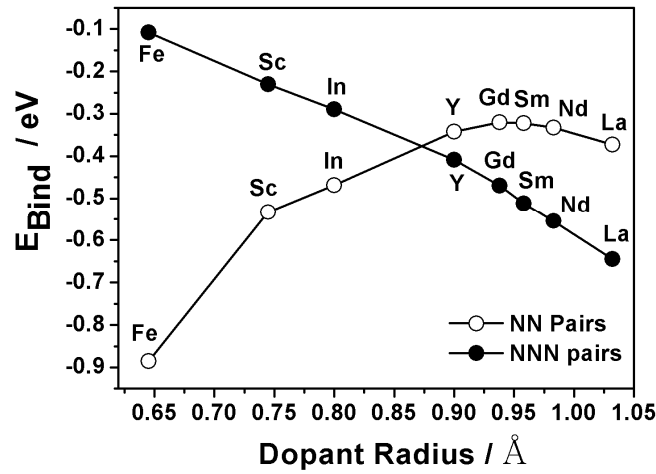


**Figure 6.8** Binding energies of dopant and oxygen vacancies as a function of dopants radius.

### 6.3.7 Oxygen ion migration

Finally, some information about oxygen migration we extracted these simulations. It is generally accepted that oxygen diffusion is based on rapid transport of oxygen vacancies which migrate by a conventional hopping mechanism [39]. Atomistic simulation have been successfully used to investigate oxygen vacancy migration of other compounds like AZrO<sub>3</sub> [5], ACeO<sub>3</sub> [6, 10] and LaBO<sub>3</sub> [11, 39]. In order to find the activation energy for oxygen ion migration, it is necessary to locate the lowest saddle point on the energy surface for the various possible pathways. The saddle point is the highest point along lowest energy pathway for an oxygen ion to move between two vacant oxygen sites. The activation energy for O<sup>2-</sup> migration due to the presence of vacancies is just the difference in the lattice energy when the moving O<sup>2-</sup> is positioned on the saddle point and either of the two octahedron corners.

In this study, the energy profile was mapped out by calculating the defect energy of oxygen ion migrating along the diffusion path between adjacent oxygen sites followed the method of Cherry *et al.* [39]. Each energy point was obtained after relaxation of the lattice at the fixed coordinates of the migrating ion. The contour plot of potential energy surface for oxygen vacancy migration is presented in **Figure 6.9**. It clearly shows that the migration “channel” follows a small deviation from the direct

path for vacancy migration. Migrating ion within the perovskite lattice is commonly assumed to take a direct linear path along the  $\langle 110 \rangle$  edge of the BO<sub>6</sub> octahedron into a neighbouring vacancy, for which the saddle point is located midway between the two anion sites [39]. However, **Figure 6.9** shows that oxygen follows a curved route with the saddle point bowed away from the adjacent Sn cation. This curved pathway had also been foreseen in other perovskite compounds like BaCeO<sub>3</sub> [6] and CaZrO<sub>3</sub> [4].

In the case of BaSnO<sub>3</sub>, the saddle point obtained is displaced at a distance of 0.12 Å from the linear path with migration energy of 0.65 eV. It has been reported that the migration path of BaCeO<sub>3</sub> with cubic structure is observed at a distance of 0.35-0.40 Å from the linear path with the migration energy 0.84 eV [6], undoped CaZrO<sub>3</sub> and SrZrO<sub>3</sub> are found at distances of 0.42 Å and 0.20 Å from the linear paths with calculated activation energies of 0.42 eV and 0.58 eV, respectively [5]. These results tend to show that the curvature is more pronounced for larger B-site atoms. The small value of such distance for BaSnO<sub>3</sub> is also coherent with the fact previously mentioned that tin is small on its site in this compound. According to experimental results, oxygen migration energies lies in the range 0.7 eV to 1.2 eV in acceptor-doped BaSnO<sub>3</sub> compounds. According to DFT calculations, the oxygen migration energy lies in the range of 0.65 eV-0.79 eV also in acceptor-doped compounds. Thus the value obtained here might reflect only part of the vacancy hopping mechanism. In particular, it is important to keep in mind that this calculated energy relate to intrinsic migration of oxygen vacancies and do not include possible association energies or dopant effects. These additional energy terms may account for the larger activation energies that are found experimentally.

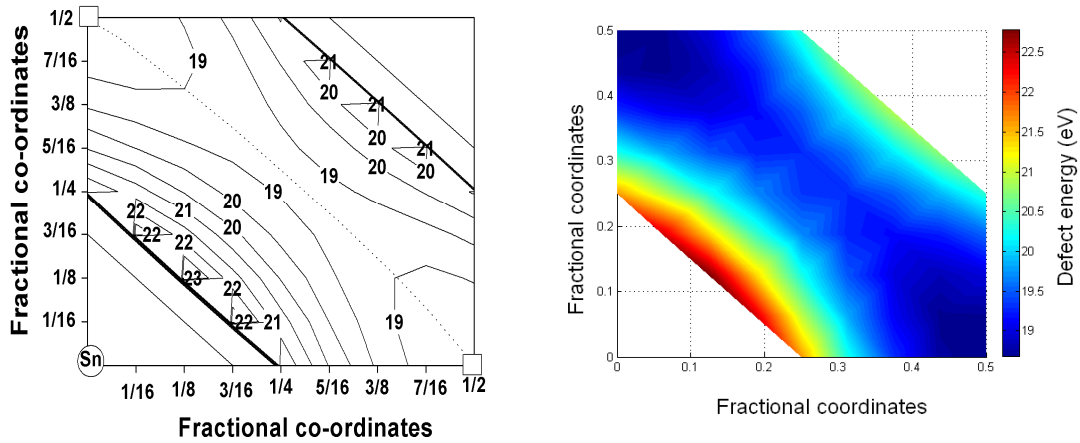


**Figure 6.9** Contour plot of potential energy surface for oxygen vacancy migration (showing the curved path or channel between adjacent anion sites)

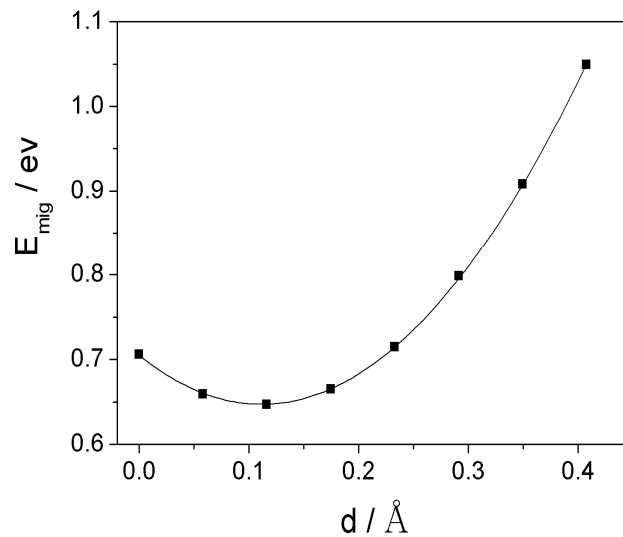


**Figure 6.10** Migration energy of an oxygen ion as a function of the distance,  $d$ , orthogonally from the linear path connecting nearest-neighbor oxygen sites.

**Figure 6.10 (b)** shows the evaluation of the activation energy of oxygen migration as we displace the oxygen ion in the saddle point away from the central Sn. The minimum energy is obtained at a distance of  $0.12 \text{ \AA}$  from the linear path with the migration energy,  $E_{\text{mig}} = 0.65 \text{ eV}$  by fitting the curve using polynomial. It has been reported that the migration energy of  $\text{BaCeO}_3$  with cubic structure is observed at a distance of  $0.35\text{-}0.40 \text{ \AA}$  from the linear path with the migration energy  $0.84 \text{ eV}$  [6], undoped  $\text{CaZrO}_3$  and  $\text{SrZrO}_3$  are found at distances of  $0.42 \text{ \AA}$  and  $0.2 \text{ \AA}$  from the linear paths with calculated activation

energies of 0.42 eV and 0.58 eV, respectively [5]. These results have shown that incorporation of a larger dopant on the B-site produce a greater path curvature, and increasing the oxygen migration energy. It is important to note that the calculated energies relate to intrinsic migration of oxygen vacancies and do not include energies of defect formation or association. These additional energy terms may account for the larger activation energies (1 eV) that are found for certain dopant levels.

## 6.4 Conclusion

Atomistic simulation techniques have been used to get further insight into the defect properties of pure and doped BaSnO<sub>3</sub>. The conclusions are drawn from our results as follows.

The potentials used reproduce well the observed properties of cubic BaSnO<sub>3</sub> and might be used for other stannate compounds. Actually, pyrochlore structures (not presented here) are also very well reproduced with the tin-oxygen potential used here.

Calculated energies for creating intrinsic defects are relatively high, with the most favourable energy for the formation of BaO vacancy pairs.

Oxidation and reduction behaviour is similar to that observed in other barium-based perovskite compounds though a higher reducibility might be observed if compared to barium zirconate.

The trivalent dopants, Sc<sup>3+</sup>, In<sup>3+</sup>, and Y<sup>3+</sup> have relatively favourable solution energies at the Sn site. For cations greater than Sm<sup>3+</sup>, some partial substitution on A-site cannot be discarded and even is partly proved by experimental values.

The predicted lattice parameters, deduced from defect volume calculations, as a function of dopant radius and concentration are in good agreement with experimental values.

The binding energy of  $(M'_{Sn} : V_o^{**})^{\bullet}$  association with dopant size shows that small size dopants prefer a cluster geometry in which the oxygen vacancy resides in a nearest neighbour site, while for the big size dopants, the oxygen vacancy is located in

a next nearest neighbour site. The yttrium dopant is the one that probably leads to less association effects.

The oxygen migration energy is calculated to be around 0.65 eV, in partial agreement with the experimental values. Oxygen ions were found to follow a slightly curved trajectory on hopping between adjacent vacancy sites.

## References

- [1] E. Bevilion, G. Gregory, *Phys. Rev. B* **2008**, 77, 184113.
- [2] R. I. Hines, N. L. Allan, W. R. Flavell, *J. Chem. Soc., Faraday Trans.* **1996**, 92.
- [3] C. A. J. Fisher, M. S. Islam, R. J. Brook, *Journal of Solid State Chemistry* **1997**, 128, 137.
- [4] M. S. Islam, *Journal of Materials Chemistry* **2000**, 10, 1027.
- [5] R. A. Davies, M. S. Islam, J. D. Gale, *Solid State Ionics* **1999**, 126, 323.
- [6] R. Glockner, M. S. Islam, T. Norby, *Solid State Ionics* **1999**, 122, 145.
- [7] M. S. Khan, M. S. Islam, D. R. Bates, *J. Phys. Chem. B* **1998**, 102, 3099.
- [8] M. Cherry, M. S. Islam, J. D. Gale, C. R. A. Catlow, *J. Phys. Chem.* **1995**, 99, 14614.
- [9] M. S. Islam, P. R. Slater, J. R. Tolchard, T. Dinges, *Dalton Transactions* **2004**, 3061.
- [10] G. C. Mather, M. S. Islam, *Chem. Mater.* **2005**, 17, 1736.
- [11] M. S. Islam, *Solid State Ionics* **2002**, 154, 75.
- [12] F. J. Berry, E. Moore, M. Mortimer, X. Ren, *et al.*, *Journal of Solid State Chemistry* **2008**, 181, 2185.
- [13] M. Pirzada, R. W. Grimes, L. Minervini, J. F. Maguire, K. E. Sickafus, *Solid State Ionics* **2001**, 140, 201.
- [14] L. Minervini, M. O. Zacate, R. W. Grimes, *Solid State Ionics* **1999**, 116, 339.
- [15] G. V. Lewis, C. R. A. Catlow, *Journal of Physics and Chemistry of Solids* **1986**, 47, 89.
- [16] K. J. W. Atkinson, PhD thesis, *Department of Materials*, Imperial College of Science, Technology and Medicine, **2002**.
- [17] J. D. Gale, *J. Chem. Soc., Faraday Trans* **1997**, 93, 629.
- [18] C. R. Stanek, PhD thesis, *Department of Materials*, Imperial College of Science, Technology and Medicine, **2003**.
- [19] P. Ordejon, E. Artacho, J. M. Soler, *Physical Review B* **1996**, 53, R10441.

- [20] J. M. Soler, E. Aetacho, J. D. Gale, *et al.*, *Journal of Physics: Condensed Matter* **2002**, *14*, 2745.
- [21] J. P. Perdew, K. Burke, M. Ernzerhof, *Physical Review Letters* **1996**, *77*, 3865.
- [22] N. Troullier, J. L. Martins, *Physical Review B* **1991**, *43*, 1993.
- [23] C. R. A. Catlow, J; Jacobs, P W M; A. B. Lidiard, *Journal of Physics C: Solid State Physics* **1981**, *14*, L121.
- [24] M. O. Zacate, L. Minervini, D. J. Bradfield, R. W. Grimes, K. E. Sickafus, *Solid State Ionics* **2000**, *128*, 243.
- [25] T. Maekawa, K. Kurosaki, S. Yamanaka, *Journal of Alloys and Compounds* **2006**, *416*, 214.
- [26] E. Bevillon, A. Chesnaud, Y. Wang, G. Dezanneau, G. Geneste, *J. Phys.: Condens. Matter* **2008**, 145217
- [27] N.L. Allan, T.H.K. Barron, J. A. O. Bruno, *J. Chem. Phys.* **1996**, *105*, 8300.
- [28] E. Bévillon, A. Chesnaud, Y.Z. Wang, G. Dezanneau, G. Geneste, *J. Phys.: Condens. Matter* **2008**, 145217
- [29] D. Shima, S. M. Haile, *Solid State Ionics* **1997**, *97*, 443.
- [30] P. G. Sundell, M. E. Bjorketun, G. Wahnstrom, *Physical Review B* **2006**, *73*, 104112
- [31] R. D. Shannon, *Acta Cryst.* **1976**, *A32*, 751.
- [32] J. Wu, R. A. Davies, M. S. Islam, S. M. Haile, *Chem. Mater.* **2005**, *17*, 846.
- [33] T. Schober, *Solid State Ionics* **1998**, *109*, 1.
- [34] P. Murugaraj, K. D. Kreuer, T. He, T. Schober, J. Maier, *Solid State Ionics* **1997**, *98*, 1.
- [35] M. S. Khan, M. S. Islam, D. R. Bates, *Journal of Materials Chemistry* **1998**, *8*, 2299.
- [36] J. Wu, L. P. Li, W. T. P. Espinosa, S. M. Haile, *J. Mat. Res.* **2004**, 2366.
- [37] M. Mogensen, D. Lybye, N. Bonanos, P.V. Hendriksen, F. W. Poulsen, *International conference on ionic and mixed conducting ceramics*, San Francisco, CA (US), 2002, **2001**.
- [38] E. Bevillon, G. Geneste, *Physical Review B* **2008**, *77*, 184113.
- [39] M. Cherry, M. S. Islam, J. D. Gale, C. R. A. Catlow, *Solid State Ionics* **1995**, *77*, 207.

# Chapter 7 Conclusion and Perspective

## 7.1 Conclusion

### 7.1.1 Resume of the main results

First, a gel polymerization method has been successfully developed to obtain pure (if we except residual  $\text{BaCO}_3$ ) and homogeneous  $\text{BaSn}_{1-x}\text{M}_x\text{O}_{3-\delta}$  ( $x = 0-0.5$ ,  $\text{M} = \text{Fe}, \text{Sc}, \text{In}, \text{Y}, \text{Gd}, \text{Sm}, \text{Nd}$  and  $\text{La}$ ) nanopowders after calcination at  $1200^\circ\text{C}$  for 4 h. In this case, the average particle size is typically 100-200 nm and compounds present a cubic perovskite structure (Space group:  $Pm\bar{3}m$ ). The sinterability of these nanopowders is dependent on the dopant nature but, in all cases, rather high if compared to most of previous studies. For In and Fe dopants, the relative densities reach up to 94-98 % at  $1500-1600^\circ\text{C}$  while the relative densities are about 90 % for other dopants, *i.e.* Sc, Y and Gd.

The defect chemistry of  $\text{BaSn}_{0.75}\text{M}_{0.25}\text{O}_{3-\delta}$  ( $\text{M} = \text{Fe}, \text{Sc}, \text{In}, \text{Y}, \text{Gd}, \text{Sm}, \text{Nd}$  and  $\text{La}$ ) compounds has been investigated taking into account structural considerations, atomistic simulations and transport measurements. The lattice parameters do not show the systemic trend with the radii of dopants, but an abnormal drop for Sm, Nd and La. The small cell parameters of the Sm-, Nd- and La- doped  $\text{BaSnO}_3$  can be explained by partial occupation of the Ba-site, which is supported by semi-empirical calculations. These simulations also show that the trivalent dopants, Sc, In, and Y have relatively favorable solution energies at the Sn site and the smaller association energy with oxygen vacancies.

When dealing now with the behavior of such compounds as proton conductors, we observed that all compounds present at low temperature a dominating proton conduction in wet atmosphere. Besides, the highest values of water uptake and proton conductivities are observed for Sc- and Y-doped  $\text{BaSnO}_3$ , respectively. This confirms that, if Y is favorable for the proton mobility, the high negative hydration enthalpy for Sc-doped  $\text{BaSnO}_3$  stabilizes the proton at higher temperature within the structure but impedes its movement. As a general rule, the best ion conduction properties, either for oxygen or

protons, are obtained for the highest doping levels, which indicate that for the range of composition studied the conductivity is driven by the number of charge carriers.

The stabilities of Y-doped BaSnO<sub>3</sub> were investigated under different atmospheres and conditions. In H<sub>2</sub>O, CO<sub>2</sub> and H<sub>2</sub>-containing atmospheres, the Y-doped compounds do not present impure phases by XRD. However, the conductivity of 37.5 mol % Y-doped barium stannate degrades after several measurements, which results in the collapse of the structure. For low yttrium content, we have not observed any degradation of conductivities neither the appearance of parasitic phase in the sample treated in humidified and highly reducing atmosphere.

Finally, we showed that the use of zinc oxide as a sintering aid for the 25 mol % Y-doped BaSnO<sub>3</sub> compound allows obtaining a relative density of 95 % after a sintering at 1300 °C. Zinc oxide as a sintering aid does not affect the bulk conductivity and even slightly increases the total conductivity.

### 7.1.2. Comparison of barium stannate with typical proton conductors

For typical proton conductors, it is well known that acceptor-doped BaCeO<sub>3</sub> shows the highest proton conductivity, but its long-term stability in CO<sub>2</sub> and water-containing atmosphere remains a concern. Y-doped BaZrO<sub>3</sub> combine high bulk proton conductivity and good chemical stability, and is considered to be a good candidate electrolyte material for intermediate-temperature fuel cells. In this study, we find that Y-doped BaSnO<sub>3</sub> compounds also exhibit high proton conductivity and good chemical stability in CO<sub>2</sub>-containing atmosphere, *i.e.* the bulk conductivity of 12.5 mol % Y doped BaSnO<sub>3</sub> in wet Ar is  $1.2 \times 10^{-3}$  S/cm at 600°C, is slightly lower than that of 10 mol % Y doped-BaZrO<sub>3</sub>,  $3 \times 10^{-3}$  S/cm at 600°C (Bohn *et al.* *J. Am. Ceram. Soc.*, 20000) in the wet air.

## 7.2 Perspective

First of all, it has been put into evidence that Sc<sup>3+</sup> dopant atoms favor a good hydration rate of samples at high temperature, while yttrium dopant lead to favorable energetic map for protons movement. Besides, Sc<sup>3+</sup> dopant as a smaller atom than Y<sup>3+</sup>

would probably enhance the stability of compounds. One may then think that a combination of both atoms could probably give an intermediate behavior and could then be used to improve the conduction and stability properties.

Then, a next step in atomistic simulations would concern the modeling of protons inside the doped  $\text{BaSnO}_3$  material. This would first give some indications on the localization of protons even if some previous results are already available for other perovskite compounds. More interesting would be to determine the possible dopant-proton interaction energies that would help determining the best dopant atoms. Since yttrium has already been identified as one of them, the simulations would allow understanding better the reasons for such good conduction properties.

Finally, another concern is the stability of barium stannate compounds. In this study, we have shown that this stability is probably intermediate between that of cerate and that of zirconate compounds but we only tested yttrium-doped compounds. It would be thus interesting to test whether other dopant atoms lead to similar conclusions. It is already anticipated that a smaller dopant would probably not give so poor stability for high doping levels. Besides, Barium Cerate which is one of the most promising proton conductors due to its high conduction suffers from strong problems of stability. The solid solution with a barium stannate compound could probably solve some of the problems encountered, even if a degradation of properties could be observed.

**Appendix A****Résumé en Français****Objectif:**

L'objectif de ce travail de thèse consistait à étudier de nouveaux matériaux pour applications aux piles à combustible de formule  $\text{BaSn}_{1-x}\text{M}_x\text{O}_{3-\delta}$  ( $x = 0-0.5$ ,  $M = \text{Fe, Sc, In, Y, Gd, Sm, Nd}$  and  $\text{La}$ ). Ces composés présentent sous atmosphère humide une conduction protonique non négligeable potentiellement intéressante au sein de piles à combustible basse température. La thèse se suivant les parties suivantes:

- Chapitre 1: Introduction
- Chapitre 2 : Méthodes
- Chapitre 3 : Elaboration et étude de composés  $\text{BaSn}_{1-x}\text{M}_x\text{O}_{3-\delta}$  ( $x = 0.125 / 0.25$ ,  $M=\text{Fe, Sc, In, Y, Gd, Sm, Nd}$  and  $\text{La}$ )
- Chapitre 4 : Elaboration et étude de composés  $\text{BaSn}_{1-x}\text{Y}_x\text{O}_{3-\delta}$  ( $x = 0 - 0.5$ )
- Chapitre 5 : Effets de l'ajout de ZnO comme agent de frittage
- Chapitre 6 : Modélisation
- Chapitre 7 : Conclusion

**Résumé de la thèse****Chapitre 1 : Introduction**

Au cours de l'introduction, nous décrivons le contexte général des piles à combustible et plus particulièrement des piles à combustible à oxyde solide. En soulignant que l'abaissement de la température de fonctionnement des piles permettrait de limiter des surcoûts importants et un vieillissement accéléré des composants, nous montrons qu'une voie pour parvenir à cet abaissement de température passe par l'emploi de matériaux de type conducteurs protoniques, plus performants que les conducteurs anioniques à basse température. Nous présentons plusieurs matériaux connus comme étant de bons

conducteurs protoniques tels que le cérate de baryum ou le zirconate de baryum. Ceci permet d'introduire directement les stannates de baryum de structure cristalline voisine pour lesquels des propriétés de conduction protonique ont également été observées. Nous insistons sur le fait que ces études sont extrêmement limitées et ne permettent donc pas de décider définitivement sur l'utilité ou non de ces composés. Ceci nous amène naturellement à notre étude systématique de ces composés avec l'objectif de démontrer leurs potentialités au sein des piles à combustible.

## **Chapitre 2: Techniques expérimentales**

Au cours de ce chapitre, nous présentons les méthodes que nous avons employées au cours de cette thèse. Nous insistons particulièrement sur la technique d'élaboration de poudres par polymérisation d'acide acrylique que nous avons développées afin d'obtenir des poudres aisément densifiables. Le résultat est convaincant puisque nous obtenons des céramiques après frittage de densité de l'ordre de 90%, là où des méthodes plus classiques ne permettaient pas de dépasser 80%.

## **Chapitre 3: Synthèse, structure et propriétés électriques de composés $\text{BaSn}_{1-x}\text{M}_x\text{O}_{3-\delta}$**

Ensuite, nous avons élaboré une série d'échantillons du type  $\text{BaSn}_{1-x}\text{M}_x\text{O}_{3-\delta}$  ( $x = 0.125 / 0.25$ ,  $\text{M} = \text{Fe}, \text{Sc}, \text{In}, \text{Y}, \text{Gd}, \text{Sm}, \text{Nd}$  and  $\text{La}$ ), pour lesquels nous avons à la fois étudié les propriétés structurales, microstructurales et les propriétés de transport. L'objectif avoué était d'identifier les dopants permettant d'obtenir les propriétés de transport les plus intéressantes. A l'aide à la fois de mesures de thermogravimétrie permettant de déterminer l'absorption d'eau et de mesures électriques, nous avons pu déterminer que les dopants  $\text{Sc}^{3+}$  et  $\text{Y}^{3+}$  étaient ceux permettant d'obtenir les meilleurs propriétés de conduction protonique. D'un autre côté, nous avons montré qu'une évolution non monotone des paramètres de maille en fonction du rayon du dopant pouvait s'expliquer par la présence du cation dopant sur le site A en supposant également une perte par évaporation du baryum.

#### **Chapitre 4: Propriétés structurales, incorporation protonique et conductivité de composés $\text{BaSn}_{1-x}\text{M}_x\text{O}_{3-\delta}$**

Faisant suite au chapitre 3 où nous avons montré que le dopant le plus intéressant du point de vue des propriétés électriques était l'yttrium, nous avons réalisé une étude étendue des composés dopés à l'yttrium. Au cours de ce chapitre, nous montrons que les propriétés de transport sont améliorées lors que le taux de dopant augmente, ce qui peut s'expliquer par l'augmentation du nombre de porteurs et l'augmentation de la taille de grains avec le taux d'yttrium. Cependant, nous montrons également que la stabilité du matériau pour ces forts taux de dopage est fortement réduite. En effet, les matériaux les plus fortement dopés se dégradent sous atmosphère humide. Nous avons également montré que les composés sont stables sous atmosphère hydrogénée même si les joints de grain semblent se réduire facilement pour donner une contribution électronique non négligeable à la conduction totale sous hydrogène.

#### **Chapitre 5: Effet de l'addition de ZnO sur le frittage et les propriétés électriques de $\text{BaSn}_{0.75}\text{Y}_{0.25}\text{O}_{3-d}$**

Les températures de frittage de 1500°C telles que utilisées lors des chapitre 3 et 4 sont extrêmement contraignantes du point de vue de l'application et une solution de mise en forme à basse température doit donc être trouvée. Au cours de ce chapitre, nous explorons donc une nouvelle méthode mise en forme des stannates de baryum où ZnO est utilisé comme additif afin de faciliter le frittage. Nous montrons qu'il est possible de par l'emploi de 4% (en poids) de ZnO comme additif de baisser de plusieurs centaines de degrés la température de frittage des matériaux sans pour autant affecter les propriétés de conduction. Il est même remarquable de constater que la conduction est même améliorée pour une céramique frittée avec ZnO à 1350°C, au lieu de 1500°C pour un frittage classique.

**Chapitre 6: Simulation à l'échelle atomique de BaSnO<sub>3</sub> pur et dopé**

Enfin, au cours d'un dernier chapitre qui vient en complément des chapitres 3 et 4, nous avons réalisé une étude par calculs semi-empiriques de l'effet du dopant au sien de BaSnO<sub>3</sub>. Cette étude permet d'une part de montrer que les dopants qui viennent s'insérer le plus facilement au sien du composé mère sont In<sup>3+</sup>, Sc<sup>3+</sup>, et Y<sup>3+</sup> correspondant aux cations ayant le rayon ionique le plus proche de Sn<sup>4+</sup>. Ces calculs permettent également de prévoir l'évolution des paramètres de maille en fonction d'un modèle de défaut et viennent donc en support aux hypothèses faites lors du chapitre 3 de substitution partielle sur le site A par les gros dopants. Ces calculs permettent également d'anticiper une faible interaction entre l'yttrium et la lacune d'oxygène qui permet d'expliquer en grande partie les bonnes propriétés de conduction de ces composés.

**Chapitre 7. Conclusion**

Enfin, en conclusion, nous essayons en résumant les propriétés observées de stannates de baryum dopées, de les resituer dans le contexte général de l'application visée. Nous montrons ainsi que les stannates de baryum peuvent être intéressantes pour l'application aux piles à combustible pour peu que le taux de dopant soit limité, que la taille de grain soit importante, que le procédé d'élaboration soit optimisé afin d'éviter les hautes températures de frittage. Nous montrons que, si le niveau de conduction est faible si comparé à celui des cérates, il est par contre tout-à-fait comparable à celui des zirconates. Une solution de compromis consisterait alors certainement à fabriquer des solutions solides entre BaCeO<sub>3</sub> et BaSnO<sub>3</sub> dopés, afin de combiner les propriétés intéressantes de conduction ou de stabilité des deux matériaux.